



Amorphization by mechanical deformation

B.Y. Li^a, A.C. Li^a, S. Zhao^{b,*}, M.A. Meyers^{a,*}

^a Materials Science and Engineering Program, University of California, San Diego, La Jolla, 92093, USA

^b School of Materials Science and Engineering, Beihang University, Beijing 100191, China

ARTICLE INFO

Keywords:

Amorphization
Mechanical deformation
Pressure
Shear
Molecular dynamics

ABSTRACT

Amorphization of crystalline structures is a ubiquitous phenomenon in metals, ceramics, and intermetallic compounds. Although the amorphous phase generally has a higher Gibbs free energy than its crystalline counterpart, there are many methods by which amorphization can be generated. The requirement to create an amorphous phase from a solid crystalline one is to increase its free energy above a critical level which enables this transition. In this review, our focus is on amorphization induced by mechanical deformation which can be imparted by a variety of means, prominent among which are tribological processes, severe plastic deformation, nanoindentation, shock compression, diamond anvil cell and ball milling/mechanical alloying. The deformation introduces defects into the structure, raising its free energy to the level that it exceeds the one of the amorphous phase, thus propitiating conditions for amorphization. Experimental observations of amorphization in metallic alloys, intermetallic compounds, ionically and covalently bonded materials are presented and discussed. There is also an observation of amorphization in a biological material: it is generated by impact deformation of hydroxyapatite in the mantis shrimp club. We also focus on the fundamental mechanisms of plastic deformation of amorphous materials; this is a closely linked process by which deformation continues, beyond amorphization, in the new phase. Observations and analyses of amorphization are complemented by computational simulations that predict the process of mechanically-induced amorphization and address the mechanisms of this transformation.

1. Introduction

There are four states of matter dictated by the fundamental state variables of pressure and temperature: solid, liquid, gas, and plasma. One phase can transform to another under certain conditions. Atoms in a solid have a restricted mobility. Every atom stays in the vicinity of one site in space, even though its position is not static; instead, it oscillates rapidly around this fixed site. Although the frequency of this oscillation is weakly related to temperature, the amplitude of this oscillation has a well-established correlation with temperature. The atomic-scale structure of the solid is composed of the spatial configuration of these fixed sites. On the contrary, a liquid does not possess an enduring configuration of atoms. In the liquid state, they are mobile and continuously moving throughout the material.

A classic example is silicon dioxide, also known as silica. It has at least three crystalline forms, commonly referred to as polymorphs (quartz, cristobalite, tridymite, and others); its amorphous form is known as glass. It is not easy for quartz to crystallize, but the slow

“geological” times are sufficiently long to obtain well-defined crystals. When molten silica is cooled, the very viscous melt, constituted of silicon and oxygen atoms, has difficulty reorganizing itself into a crystalline matrix, because of the strong covalent bonding; thus, this disordered structure of the molten state is retained in the solid state, leading to the formation of glass.

If one observes a glass blower at his trade, one can immediately see that glass has a unique property: it can be blown into a hollow sphere of an ever-increasing diameter at the end of the tube, whereas a metal would neck and fracture in tension. It can also be freely shaped if the temperature is sufficiently high. This property derives from the linear viscosity exhibited by glass, expressed as [1]:

$$\frac{\sigma}{\dot{\epsilon}} = \eta \quad (1)$$

where σ is stress, $\dot{\epsilon}$ is strain rate, and η is constant known as the Newtonian viscous coefficient. This viscosity changes with temperature as:

* Corresponding authors.

E-mail addresses: sdzst@gmail.com (S. Zhao), mameyers@eng.ucsd.edu (M.A. Meyers).

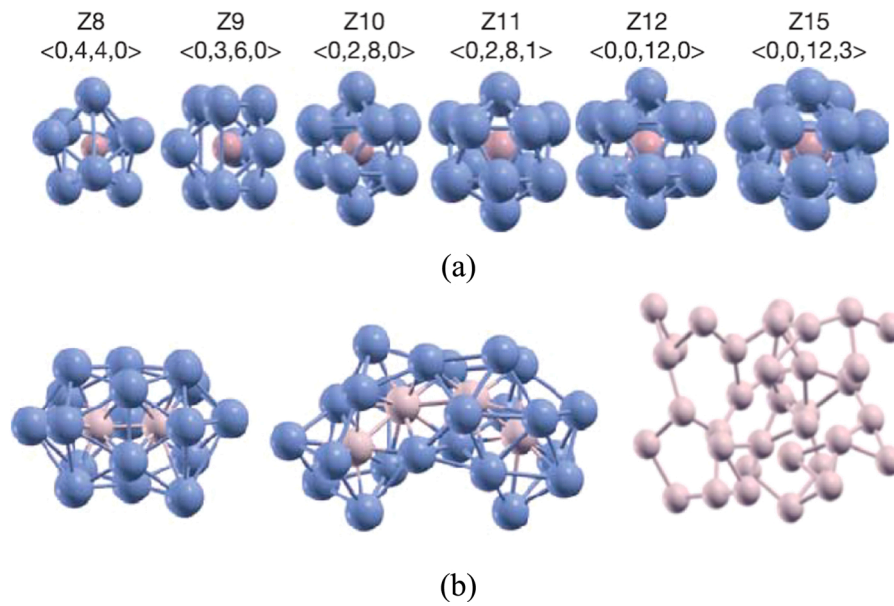


Fig. 1. Examples of short and medium range order found through ab initio molecular dynamics simulations in various metallic glasses. (a) Kasper polyhedra show the types of short-range order for different coordination numbers Z (=8, 9, 10, 11, 12, and 15). (b) Lone pair cluster in $Zr_{80}Pt_{20}$, extended string cluster in $Al_{74}Ni_{25}$, and a solute network in $Ni_{63}Nb_{37}$ (from left to right), exhibit types of medium range order [4].

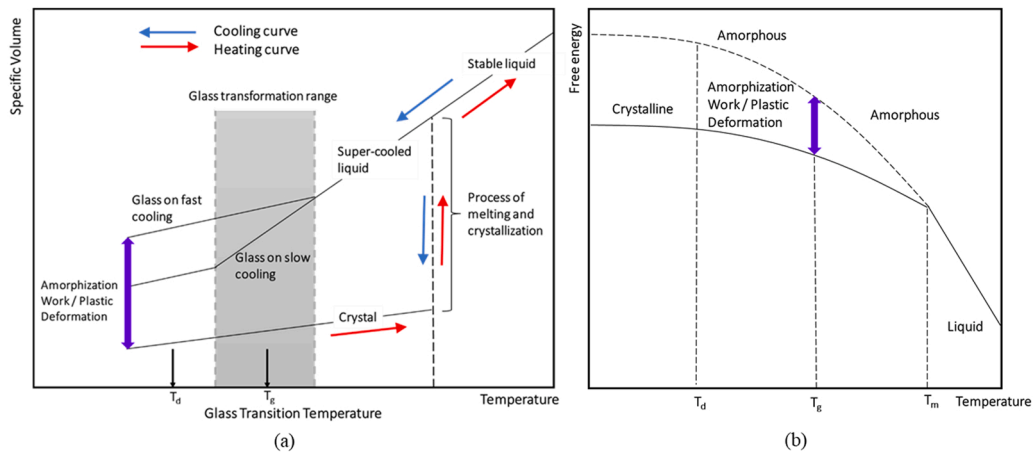


Fig. 2. (a) Generic specific volume vs. temperature showing crystallization and glass formation (on cooling) and difference in specific volume between crystalline and glassy phases. (b) Gibbs free energy vs. temperature showing crystalline and amorphous paths and difference in free energy between them.

$$\eta = \eta_0 \exp \frac{Q}{RT} \tag{2}$$

where Q is the activation energy for flow and T is the temperature in K. Crystalline metals and ceramics have a mechanical response that is quite different and is governed by defect generation and motion and crack nucleation and growth.

The common equation that expresses the strain-rate sensitivity of metals is:

$$\sigma = k \dot{\epsilon}^m \tag{3}$$

The value that differentiates glasses from metals and ceramics is the parameter m. For glasses, $m \sim 1$, giving it an extreme ability to undergo tensile extension. In metals and ceramics, on the other hand, this value is in the 0.01 range and instability sets in right away on tension. The absence of dislocations, twins and other defects in glasses, that are the agents of plastic deformation in crystals, is also responsible for another extraordinary property: glasses are often stronger than their equivalent crystalline counterparts.

The glassy form of silicates exists in nature, and obsidian is the prime example. It is produced when volcanic lava is rapidly cooled, thus bypassing crystallization. Its high hardness and sharp edges produced by a technique called ‘knapping’ have rendered it precious all the way from the Neolithic era. It has been used as arrow tips, knives, and surgical blades. The Maya used it as a weapon and in their ritual sacrifices which included the extraction of the heart from the live victim.

The synthetic counterpart of obsidian, glass, has its birth in Syria, Mesopotamia, or Egypt around 3500–2000 BCE. Although the technology of glass manufacturing reached a high level of development in the Twentieth Century, no metallic glass had been produced up to this point. In 1957, the fortuitous discovery by the brilliant Belgian scientist Duwez [2] opened the doors for research on metals that exhibit the properties of glasses and have an amorphous structure. This was accomplished by shooting a liquid pellet of a saturated solid solution into a flat target. The recovered splats showed an absence of diffraction spots upon being observed by X rays.

It is now recognized that amorphization exists in all kinds of materials and forms: metallic glasses, glassy minerals, stained glasses,

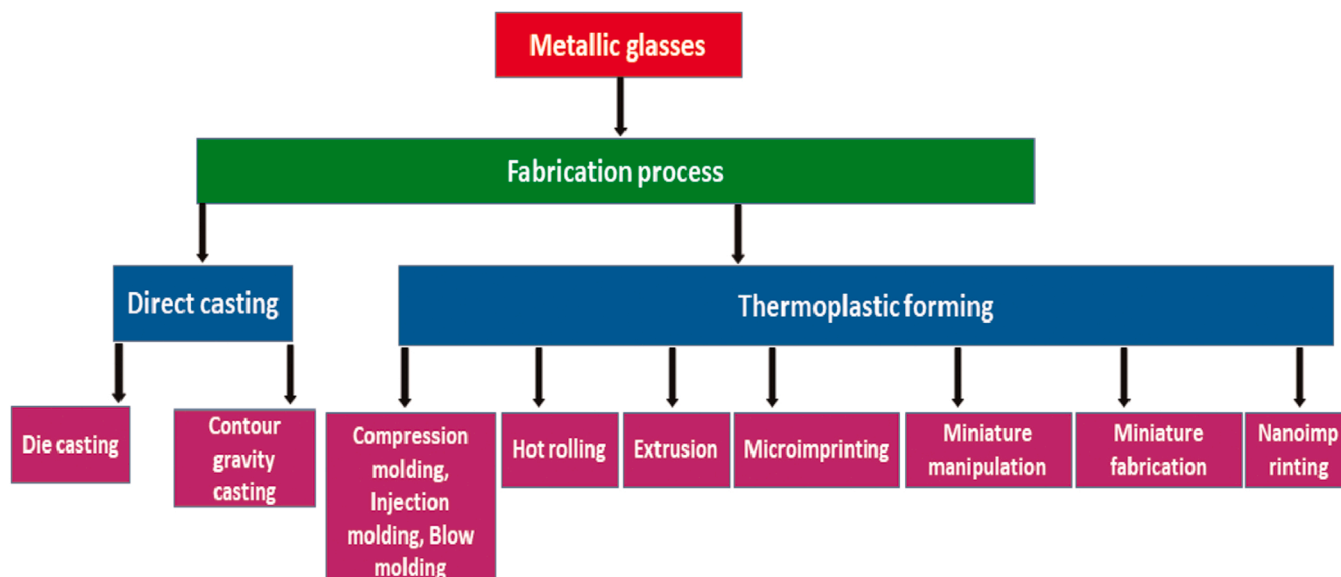


Fig. 3. Flow diagram of the fabrication of metallic glasses with two major paths: casting from melt and thermoplastic forming [9].

Table 1

Methods to generate amorphization.

Rapid cooling (quenching) of a melt, low-temperature annealing, melt spinning, melt quenching
Mechanical deformation: micropillar compression deformation, high pressure torsion, pressure-induced, static compression or decompression of crystals, tribological load, (prolonged) ball milling, mechanical alloying, Vickers indentation, tension, static high-pressure experiments, meteorite impact, deformation by tectonic processes, shock waves
Focused ion beam, ion implantation
Microwave irradiation, electron beam irradiation, neutron and charged-particle irradiation, pulsed laser irradiation, ion irradiation, femtosecond laser pulse irradiation
Vapor condensation techniques: variations of the method include using an electron beam to vaporize the source or using the plasma-induced decomposition of a molecular species, laser-assisted chemical vapor deposition, magnetron sputtering
Moderate heating
Solid state reactions
Hydrogen absorption
Numerous other methods: lyophilization, spray drying, freeze-drying, dehydration of crystalline hydrates above the crystallization temperature under an external magnetic field, followed by cooling accompanied with pulse current injection, impregnated in phosphoric acid

polymers, food, and even pharmaceuticals [3].

Amorphous (or glassy) metals are preferentially formed as a random mixture of metallic and metalloid atoms with only short-range order defined as the first- or second-nearest neighbors of an atom. There exists short-range-order (clusters) and medium-range order (extended clusters), which are distinct (Fig. 1) [4]. The cluster model is a short-range order model for amorphous materials. The solute atom is surrounded by solvent atoms. The atomic size ratio decides the coordination number of the solute atom. The extended cluster model is a medium-range-order model for amorphous materials. The solute atoms connect to form extended clusters or strings as the solute atom concentration increases. The coordination number is normally 3–7 [4].

There are three atomic scale models for amorphous solids. The first one is the continuous random-network model [5] for covalent glasses such as amorphous silicon and various oxide glasses. The second one is the random-coil model [6] for quantities of polymer-chain organic glasses like polystyrene. The third one is the random close-packing model [7] for metallic glasses, which resembles a number of marbles compacted in a paper bag. The well-defined short-range order determines that amorphous solids are not as random as a gas although they

all contain “random” in their name.

In glasses, each atom still has the nearest-neighbor atoms at the length of chemical bond, which is the same as in the corresponding crystalline material. However, the bond directions change as the distance goes farther away from an atom. Both crystalline and amorphous solids have short-range order at atomic scale as a result of chemical bonding, which holds the solid together.

It was previously believed that only a limited number of materials could be produced as glasses. These materials were known as glass-forming solids, including oxide glasses and organic polymers. It has now been realized that the amorphous solid state is generally universal in solid materials. Glass formation is a matter of bypassing crystallization (Fig. 2(a)). Nearly all materials can be produced with amorphous structure if cooled rapidly enough. Fig. 2(a) also shows how plastic deformation can increase the Gibbs free energy of the crystalline structure and lead to its transformation into the glassy one. This is indicated by the double-ended purple arrow in Fig. 2(a). This can also be expressed in terms of free energy vs. temperature (Fig. 2(b)). One can see that the amorphization is a second order transition because the slope does not have a discontinuity at the melting point. On the other hand, crystallization is a first-order transition. If deformation is imparted at a temperature T_d , the free energy is increased to the point where it reaches the one for the amorphous state and this can lead to the formation of the glassy form.

The melting and solidification between crystals and their corresponding liquids are first-order phase transitions, generating a sharp discontinuity in properties such as density. The glass transition, however, is a second-order transition, which does not have a discontinuous change in density nor does it have the latent heat of fusion. This is seen in both Fig. 2(a) and 2 (b). Nevertheless, heat capacity and thermal expansion of amorphous materials exhibit an abrupt change at glass transition temperature, making the accurate detection of crystalline to amorphous transition possible via differential scanning calorimetry [8].

In metals, the ordered crystal has higher packing efficiency, and so, the molar volume of the amorphous structure is larger than that of crystal. Therefore, the excess molar volume is a measure of disorder. This results in a positive Clapeyron slope for the boundary between solid and liquid phases in the T-P phase diagram. In contrast, many covalently bonded elements and compounds have open structures (e. g., Si, Ge, SiC, B₄C). For these solids, the densities of their amorphous phase are higher than their crystalline ones, resulting in a negative Clapeyron slope.

Metallic glasses are an important class of amorphous materials. Their

Table 2
Materials amorphized by mechanical deformation (in chronological order).

Metals and alloys			
Cu-Nb-(Si, Ge or Sn)	Mechanical alloying	Matsuki et al.[50]	1988
Nb ₃ Sn	Mechanical attrition	Cho et al.[51]	1991
Stainless steel	Hopkinson bar/shear band	Meyers et al.[52]	2003
Nanocrystalline nickel	Quasi-static compression	Han et al.[53]	2012
Graphite flakes in gray cast iron	Tribological loading (friction), Ball milling	Hinrichs et al.[54]	2018
Fe ₃ Cr ₂ Al ₂ CuNi ₄ Si ₅ HEA	Mechanical alloying and consolidation	Yang et al.[56]	2019
Cantor high-entropy alloy of CrMnFeCoNi	Hopkinson bar/shear band	Zhao et al.[57]	2021
Cantor high-entropy alloy of CrMnFeCoNi	In situ TEM tensile straining experiments	Wang et al.[125]	2021
Intermetallic compounds			
Ni-Zr	Mechanical alloying	Weeber and Bakker[62]	1988
Ni _x Zr _y	Ball milling	Chen et al.[63]	1993
Ni ₃ Al	Mechanical milling	Jang et al.[64]	1990
NiTi	Cold rolling	Koike et al.[65]	1990
Ti/Ni	Explosive welding	Nishida et al.[66]	1995
NiTi	High-pressure torsion	Huang et al.[67]	2004
NiTi shape memory alloy	Local canning compression	Jiang et al.[73]	2013
NiTi shape memory alloy	Ultrasonic Nano-crystal Surface Modification (UNSM)	Ye et al.[74]	2016
Nanocrystalline NiTi shape memory alloy micropillars	Uniaxial compression	Hua et al.[75]	2018
ZrCu and Zr ₅₀ Cu ₄₀ Al ₁₀	High pressure torsion	Tsuchiya et al.[76]	2011
SmCo ₅	Nanoindentation	Luo et al.[77]	2019
Covalently-bonded solids			
Olivine	Shock compression	Jeanloz et al.[78]	1977
Si	Mechanical scratching	Minowa et al.[79]	1992
α-quartz	Compression	Kingma et al.[80]	1993
Cristobalite	Gas gun	Gratz et al.[81]	1993
α - quartz and α -berlinite AlPO ₄	Diamond anvil cell	Cordier et al.[82]	1993
CaSiO ₃	Pressure	Serghiou et al.[83]	1993
Serpentine	Pressure and temperature	Irifune et al.[84]	1996
B ₄ C	Ballistic impact	Chen et al.[86]	2003
B ₄ C	Vickers indentation	Subhash et al.[87]	2013
B ₄ C	Indentation	Subhash et al.[88]	2016
B ₄ C	Nanoindentation	Reddy et al.[89]	2021
Boron suboxide	Nanoindentation	Reddy et al.[90]	2014
Diamond	High pressure plus laser heating	Zeng et al.[91]	2017
Diamond	High pressure and high temperature	Shang et al.[92]	2021
Diamond	High pressure and high temperature	Tang et al.[93]	2021
Si, Ge, SiC, B ₄ C	High energy laser shock compression	Zhao et al.[94]	2018
Forsterite	Static compression	Samae et al.[98]	2021
Ionic materials			
Ca(OH) ₂	Static compression	Meade and Jeanloz[99]	1990
Calcium phosphates	Pressure	Vaidya et al.[100]	1999
Biological materials			
Dactyl club samples of mantis shrimp	Quasi-static indentation and microimpact tests	Huang et al.[101]	2020

microstructure is different from crystalline metals. Metallic glass is an alloy instead of a pure metal under most conditions. It is composed of atoms with significantly different sizes, resulting in low free volume in the liquid state, and thus has orders of magnitude higher viscosity in its molten state, restraining the atoms' motion to form an ordered crystalline matrix. This structure also leads to lower volume shrinkage during cooling, which is resistant to plastic deformation. The amorphous phase does not have grain boundaries, a potential vulnerability of polycrystalline materials, contributing to better wear and corrosion resistance. Metallic glasses have properties that exceed those of other structural metals. They can survive elastic or larger reversible deformations than crystalline alloys. They do not have defects such as dislocations to undermine their strength.

Fig. 3 is a flow diagram of the fabrication of metallic glasses [9]. The fabrication processes are divided into direct casting and thermoplastic forming. Metallic glass can be formed into any shape like thermoplastic polymers upon heating.

Amorphization can be generated by a number of methods. The best known are rapid cooling (quenching), shock waves, mechanical deformation, focused ion beam, irradiation, vapor condensation techniques,

moderate heating, solid state reactions, mechanical alloying; several other methods are summarized in Table 1 [10–47].

Table 2 lists the principal materials that have been amorphized by mechanical deformation. They are grouped into metals and alloys, intermetallics, covalent, ionic, and biological materials and will be discussed in detail in Section 2 (metals and alloys), 3 (intermetallic compounds), 4 (covalently bonded solids), 5 (ionic materials), and 6 (biological materials). Mechanisms and kinetics of amorphization by mechanical deformation are given in Section 7. The fundamental deformation mechanisms in amorphous materials are presented in Section 8. Molecular dynamics has been extremely useful in studying the amorphization process by plastic deformation and in the simulation of the deformation mechanisms. This is presented in Section 9. The importance of amorphous materials can be gauged by the increasing number of publications, exemplified by the three-volume reference book edited by Taylor [48]. This compendium addresses three important components of amorphous materials: (i) chalcogenides, which have, in their glassy form, shown semiconducting properties; (ii) oxide glasses which consist of the major application of amorphous materials, and, although being known for thousands of years, present novel features;

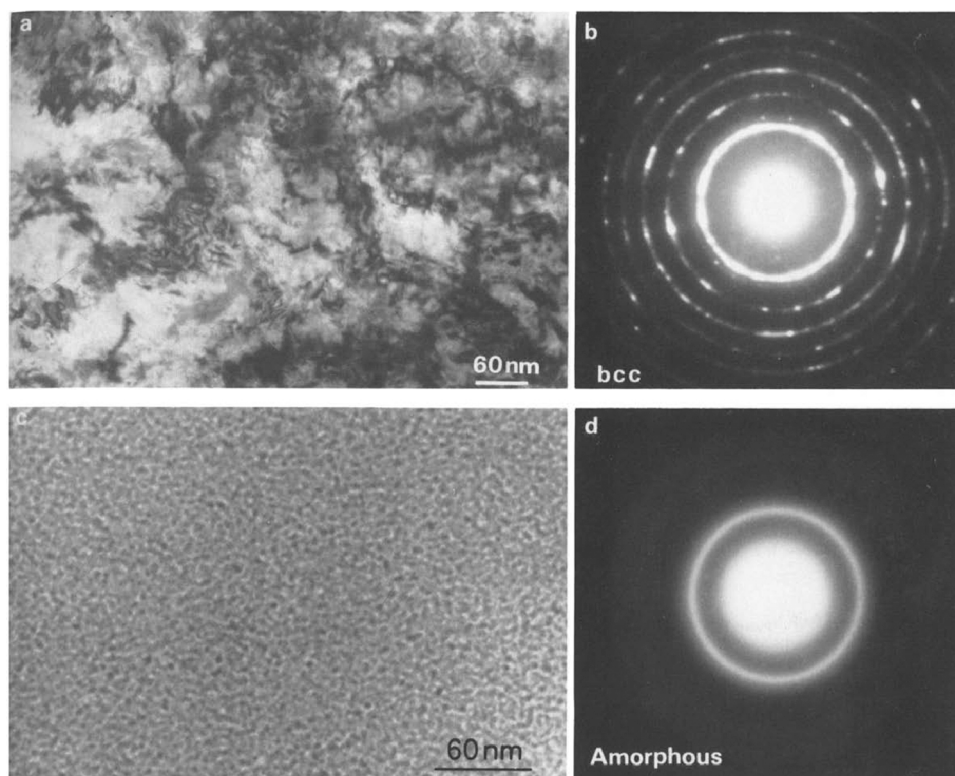


Fig. 4. Bright field electron micrographs and selected area electron diffraction patterns of $\text{Cu}_{44}\text{Nb}_{42}\text{Sn}_{14}$ powders produced by mechanical alloying after 4 h ((a) and (b)) and 24 h ((c) and (d)) [50].

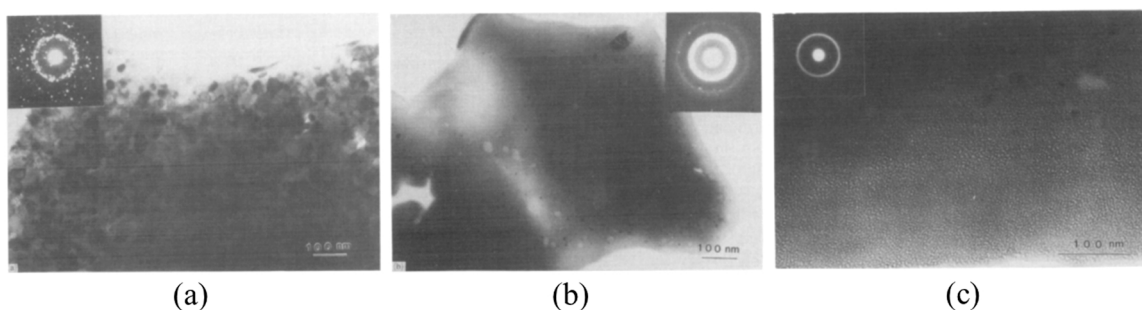


Fig. 5. (a), (b) TEM images of 5 h milled Nb_3Sn : (a) larger grain sizes of 20–50 nm; (b) nanocrystallites of 6 nm grain size in an amorphous matrix. (c) amorphous Nb_3Sn after 8 h milling [51].

and (iii) thin film amorphous semiconductors, which have applications in solar cells and IR imaging, among others.

2. Amorphization in metals and alloys

In this and subsequent sections, the observations of amorphization will be presented in a chronological order, following the sequence of Table 2. Amorphization in pure metals is very difficult to accomplish because of the extreme cooling rates required from the molten state. Similarly, it is very difficult to generate amorphization from mechanical deformation. However, different alloys including Cu-Nb-(Si, Ge or Sn) alloy systems, Nb_3Sn , stainless steel, graphite flakes in gray cast iron, Cantor and some other high-entropy alloys have been found to be amenable to amorphization by mechanical deformation.

Mechanical alloying (MA) is a solid-state powder processing method where a mixture of powders is subjected to high energy collision from milling balls in confined space; it involves repeated welding, fracturing and rewelding of powder mixtures to produce controlled, extremely

refined microstructures [49]. It is a widely used technique to prepare amorphous alloys. Amorphous alloys such as Ni-Nb, Ni-Zr, Cu-Zr, Co-Zr and Fe-Zr have been produced by MA [50]. Pure elemental powders of copper, niobium and silicon, germanium or tin were ball milled then hot pressed. Bright field electron images and corresponding selected area electron diffraction patterns are shown in Fig. 4 for $\text{Cu}_{44}\text{Nb}_{42}\text{Sn}_{14}$ powders made by MA after 4 h and 24 h milling. A high density of tangled dislocations is distributed all over the bright-field micrograph (Fig. 4(a)). The corresponding diffraction pattern (Fig. 4(b)) is comprised mainly of completely linked reflection rings of bcc structure with only a few weak reflection spots of fcc copper phase, which indicates that the bcc phase is severely deformed and with small grain size. In addition, the lack of contrast characteristic of a crystalline phase (Fig. 4(c)) and broad diffuse rings in the selected-area diffraction pattern (Fig. 4(d)) confirm the formation of an amorphous phase. The particle size of the amorphous powders after 24 h milling was reduced to about 200–500 nm from the initial size of below 34 μm . It is proposed in this study that amorphization requires three conditions: (i) fast diffusive

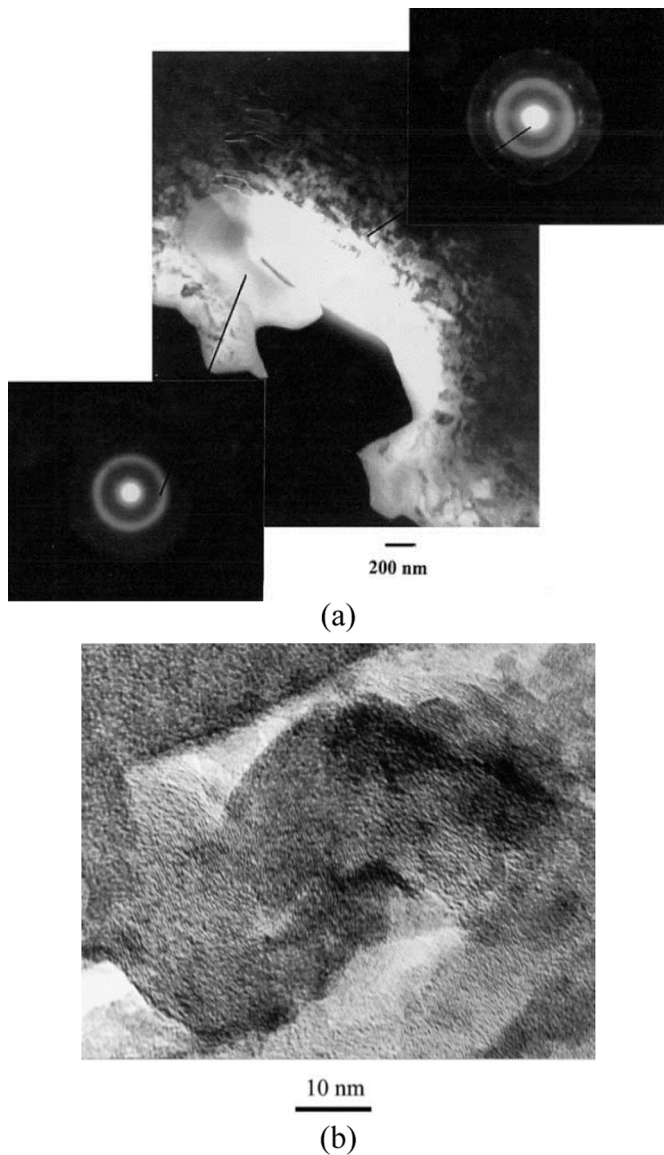


Fig. 6. (a) Nanocrystalline and amorphous regions within a shear band and the corresponding electron diffraction patterns generated by high strain and high strain rate deformation in a shear band in AISI 304 L stainless steel. (b) HRTEM images of amorphous region in the same specimen [52].

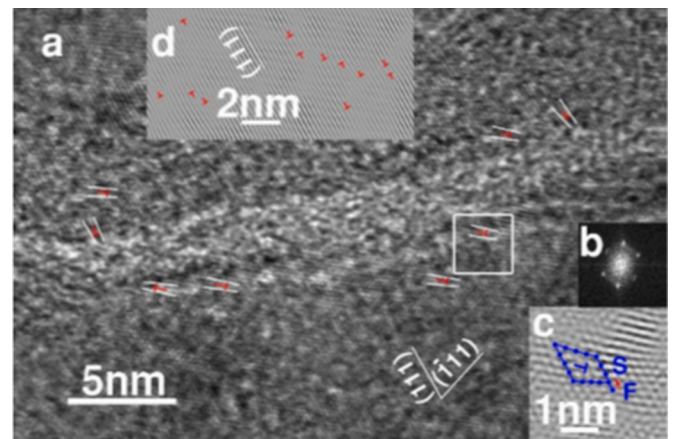


Fig. 8. TEM micrographs of dislocations around an amorphous band. (a) HRTEM image exhibits a high density of dislocations around an amorphous band. (b) the FFT pattern of the white-boxed area in (a), revealing a crystalline orientation approximately along a $\langle 110 \rangle$ zone axis. (c) Fourier-filtered image of the white-boxed area in (a), showing the details of a $a/2 \langle 110 \rangle$ full dislocation. (d) A one-dimensional Fourier-filtered image near the amorphous band. Extra (111) half-plane dislocations are marked with a red "T" [53].

solute atoms, (ii) a negative heat of mixing in the amorphous alloys which provides the chemical driving force for the amorphization reaction, and (iii) this reaction must occur at sufficiently low temperatures to restrain the nucleation of crystallization.

Amorphization by mechanical attrition was observed in the Nb_3Sn alloy when ball milling $\text{Nb} + \text{Sn}$, $\text{Nb} + \text{NbSn}_2$ or Nb_3Sn crystalline powder mixtures [51]. In starting powders of $\text{Nb} + \text{Sn}$ and $\text{Nb} + \text{NbSn}_2$, milling first formed the A15 crystalline structure Nb_3Sn phase which then transformed to the amorphous structure. The ordered A15 structure Nb_3Sn disordered completely after 1 h of milling, which was well before amorphization was first observed (5–6 h) (Fig. 5). Estimates of the free-energy and enthalpy differences between the crystalline and amorphous Nb_3Sn phases indicates that the driving force for the crystalline-to-amorphous transition derives from the total energy, consisting of the disordering energy (about 5 kJ/mol) and the energy of the defects induced by plastic deformation of the disordered crystalline Nb_3Sn (about 10 kJ/mol). The grain boundaries of the refined nanocrystallites are the possible source of the additional energy needed to initiate the amorphization transition process. The plastic deformation which occurs in the brittle A15 Nb_3Sn powder was confirmed by the work hardening and microstructures resulting from a considerable hydrostatic component of the stress state during ball milling.

Hat-shaped AISI 304 L stainless steel (Fe-18%Cr-8%Ni) specimens

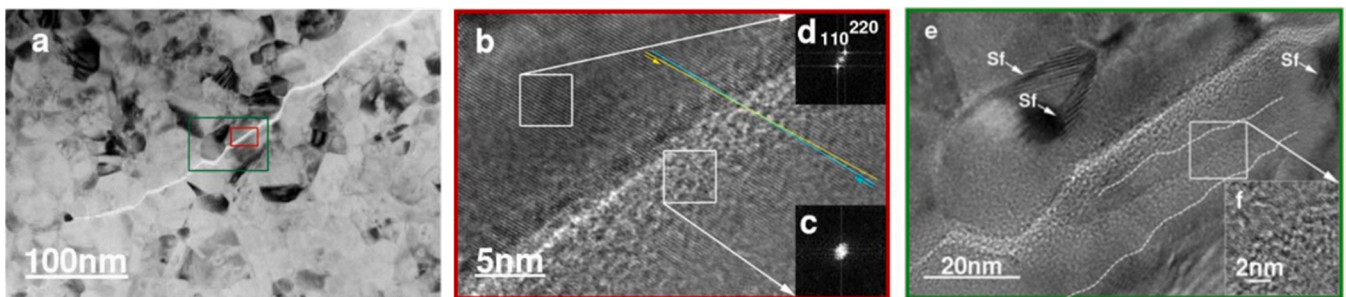


Fig. 7. TEM micrographs of post-compression nanocrystalline nickel. (a) Bright-field image of crack-like damage areas. (b) HRTEM image of the red-boxed area in (a) exhibits a 3–5 nm wide band and a misalignment of about 1° of the lattice on both sides of the band. (c) Fast Fourier transform pattern from inside the band is an amorphous halo and (d) FFT pattern of the nearby crystalline region. (e) HRTEM micrograph of the green-boxed area in (a). Stacking faults are indicated by Sf, the two white dashed lines highlight a heavily deformed band. (f) A Fourier-filtered image from the white boxed area in (e) shows the heavily deformed band is composed of amorphous phase intertwined with nanocrystals [53].

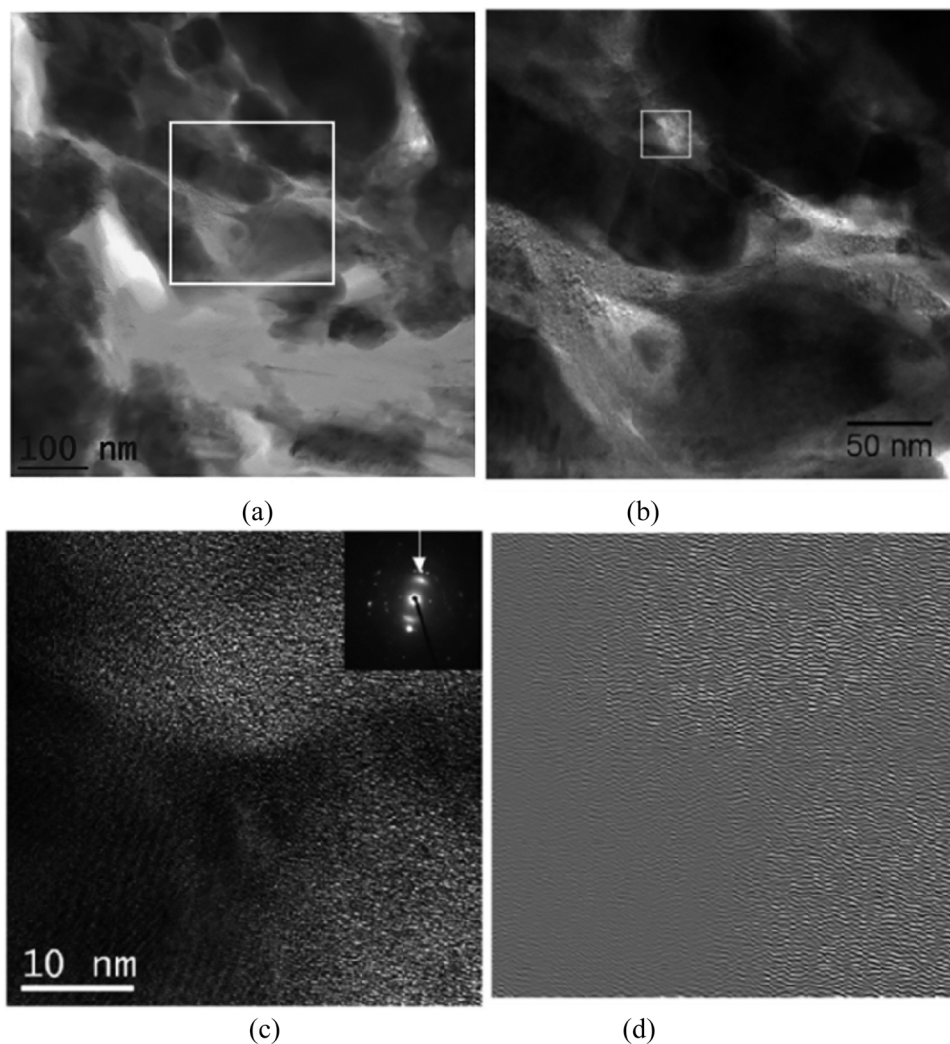


Fig. 9. Amorphization of graphite flakes in a gray cast iron disc after heavy duty automotive brake test. (a) Energy Filtered TEM images of the cross section of the disc. Light gray ribbons are graphite, dark gray grains are iron, and blotched gray grains are magnetite. (b) Higher magnification of the white-boxed area in (a). (c) Higher magnification of the white-boxed area in (b), with SAED pattern inset. (d) Inverse fast Fourier transform (IFFT) reconstructed image showing the graphite spots and that the planes are crumpled [54].

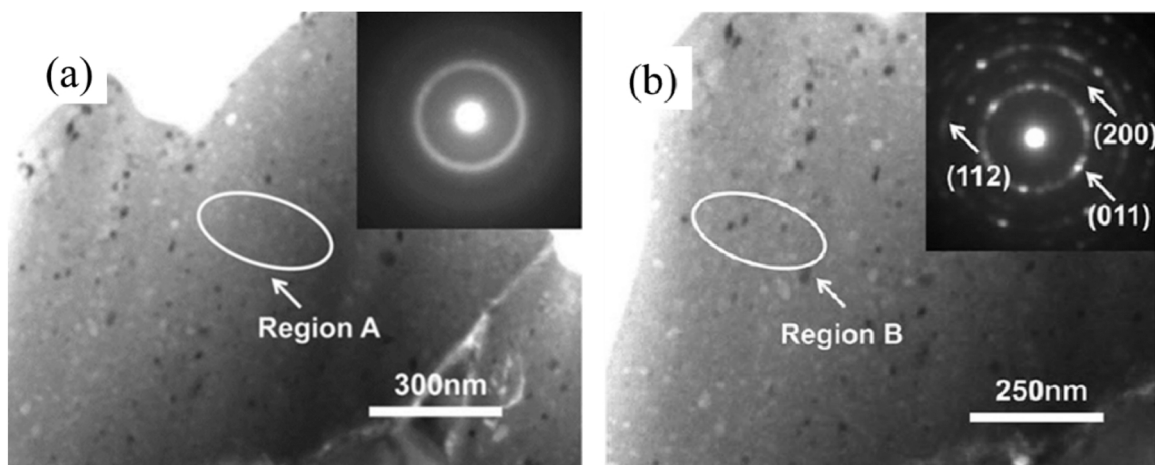


Fig. 10. TEM images of $\text{Fe}_3\text{Cr}_2\text{Al}_2\text{CuNi}_4\text{Si}_5$ HE-MG, a novel non-equiatomic alloy. (a) inset shows the diffraction pattern for the amorphous matrix, (b) inset shows the diffraction pattern for the nanoparticles [56].

were compressed in a split Kolsky-Hopkinson bar at strain rates of about 10^4 s^{-1} , generating shear strains between 1 and 100 in a narrow region [52]. Shear bands are formed as a result of the compressive deformation, and both nanocrystalline and amorphous regions within the shear bands were observed by TEM and the corresponding electron diffraction

patterns. The amorphization process was proposed to be achieved through a solid-state transformation. Outside the shear bands, stacking faults, twinning, and martensitic transformation were observed. Fig. 6 (a) shows the amorphous region in the center and the nanocrystalline region in the periphery in the TEM micrograph. The two regions are

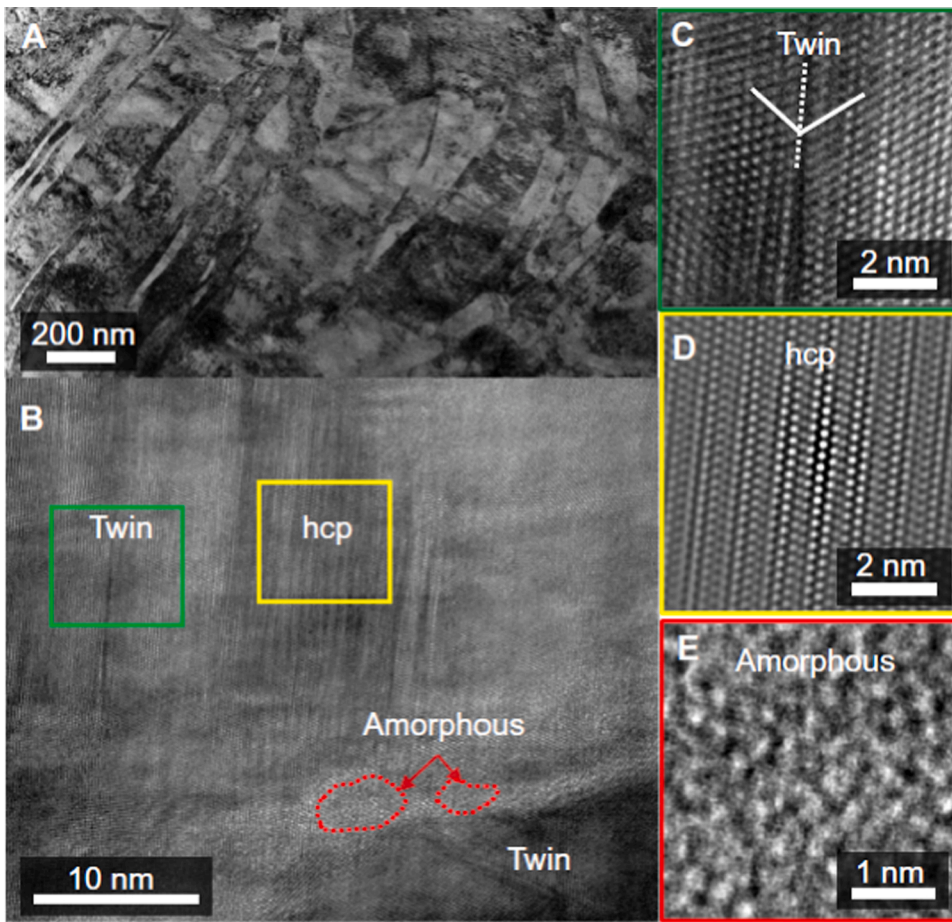


Fig. 11. Complex deformation microstructure of the swaged CrMnFeCoNi HEA after quasi-static compression at a strain rate of 10^{-3} s^{-1} . (a) TEM bright-field image shows high density planar defects. (b) HRTEM micrograph of the heavily deformed regions of twinning, hcp phase, and amorphous regions as marked. (c) Close up view of the twinned region (d) Close up view of the hcp region, with Fourier transformation-filtered to maximize phase contrast. (e) Close up view of the amorphous region, formed at the intersection of hcp and twinned region [57].

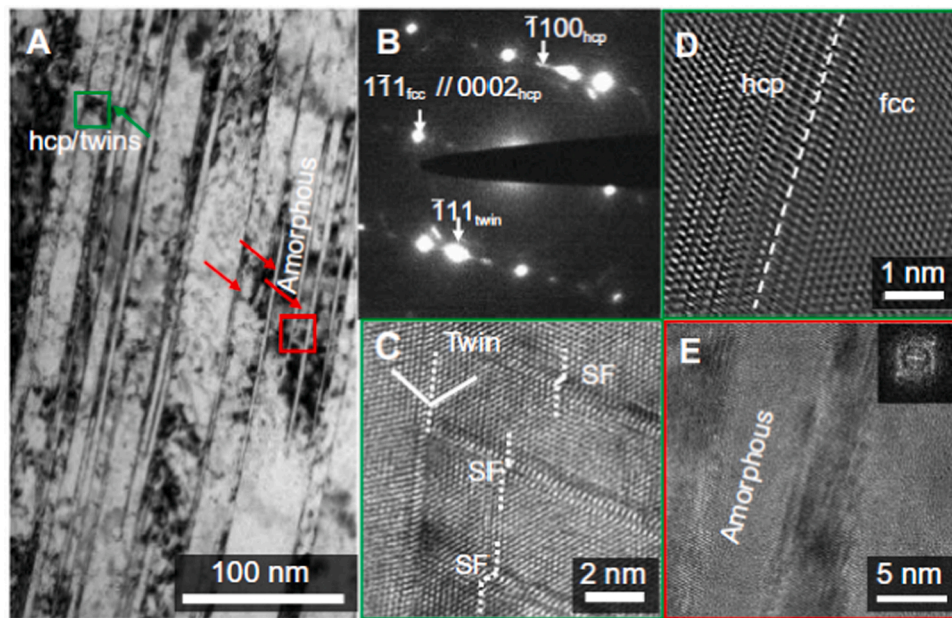


Fig. 12. Complex deformation microstructure of the CrMnFeCoNi HEA after dynamic compression/shear. (a) Bright-field TEM image of the shear band with twins, stacking faults, hcp phase, and amorphous bands. (b) SAED pattern shows the existence of the fcc matrix, twinning spot, and the hcp structures. (c) HRTEM image shows the coexistence of twins and stacking faults (SF). (d) Fourier-filtered lattice image of the interface between hcp and fcc phases. (e) HRTEM image of the amorphous bands (red-boxed area in (a)) and the corresponding fast Fourier-transformed diffractogram [57].

separated by an interface which shows both crystalline and amorphous characteristics; Fig. 6(b) confirms the amorphous nature of this area.

While amorphous structures have been observed in a variety of multi-component alloys, amorphization in pure metals has rarely been found. Localized solid-state amorphization in bulk nanocrystalline

nickel generated by quasi-static compression at a strain rate of 10^{-5} s^{-1} at room temperature was observed by high-resolution TEM [53]. Fig. 7 exhibits regions subjected to severe deformation along the crack paths or surrounding the nano-voids. These nano-scale amorphous structures were found near the highly deformed regions, indicating that

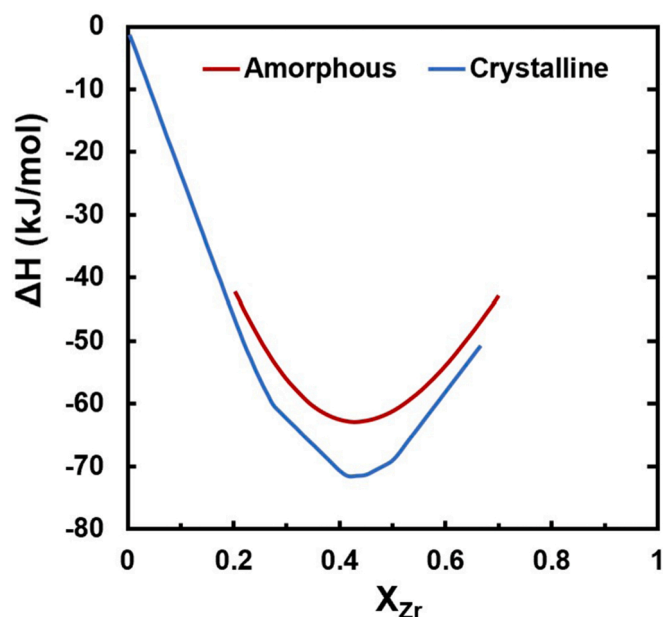


Fig. 13. Enthalpy curves of crystalline (lower, blue) and amorphous (upper, red) Ni-Zr alloys/compounds [62].

nanocrystalline structures can promote amorphization. This result may lead to new insights into the nature of the crystalline-to-amorphous transition and provide a possible method to produce elemental metallic glasses that have hardly been produced by rapid solidification so far. Fig. 8 shows the dislocations around an amorphous band.

The energy-filtered transmission electron microscopy (EFTEM) images of amorphized graphite flakes in gray cast iron under tribological loading can be seen in Fig. 9 [54]. The gray cast iron disc was subjected to a heavy-duty automotive brake test. Graphite layers were squeezed into the ferritic matrix, where oxygen could enter and subsequently form magnetite. The exfoliated few-layer graphene was heavily deformed. The Raman spectra revealed that the shear stresses on the brake surface induced disorder in a much more effective way than milling due to the additional compressive and impact forces exerted during the brake test. The high anisotropy of elastic moduli in the crystalline graphite

structure and the low attraction between the graphene layers results in the exfoliation of wrinkled few-layer graphene under shear loading, leading to more defect-related bands in Raman spectra than by mechanical stresses during high energy milling. The high elastic modulus of graphite along the basal planes results in few-layer graphite batches that penetrate the soft iron matrix, causing iron nanoparticles to peel off. This low attraction between graphene layers allows the layers to be further wedged apart by micron sized iron or magnetite particles. This mechanism explains the amorphization of graphite and formation of nano-scale magnetite in friction films during braking.

As mentioned earlier, metallic glasses (amorphous metals) are solid state materials which do not have a long-range atomic order. Most metals are crystalline and have a highly ordered atomic arrangement. Metallic glasses (MGs) present superior mechanical properties to crystalline alloys due to their glass-like microstructure. Most MGs are composed of two or more elements and the limited number of compatible principal elements restricts the development of MGs. HEAs have high configurational entropies which can significantly reduce the Gibbs free energy the alloy system and stabilize the interior structures. Some high entropy alloys (HEAs) have an amorphous phase, and have been called high entropy metallic glasses (HE-MGs) [55]. HE-MGs combine the properties of both HEAs and metallic glasses but not all HEAs can form amorphous structures. Usually, a single-phase solid solution or more complex compounds are formed instead. A high mixing entropy required for preparing HE-MGs can be achieved by using multicomponent alloys with equiatomic or near-equiatomic ratios. The $\text{Fe}_3\text{Cr}_2\text{Al}_2\text{CuNi}_4\text{Si}_5$ HE-MG was prepared by amorphous powder molding using mechanical alloying (MA) and ultrahigh pressure consolidation (UHPS), generating an amorphous matrix (Fig. 10 (a)), with uniformly distributed nanoparticles (Fig. 10 (b)) [56]. The UHPC is best performed at as low temperature as possible to retain the amorphous structure produced by MA. This technique can effectively suppress the crystallization process of the amorphous phase, thus providing a new way to prepare HE-MGs.

Figs. 11 and 12 [57] show the microstructures of a pre-deformed high entropy CrMnFeCoNi Cantor alloy that underwent quasi-static uniaxial and dynamic uniaxial compression, and was subsequently subjected to dynamic shear experiments at a shear strain rate of $6 \times 10^5 \text{ s}^{-1}$ in the same hat-shape geometry as mentioned in the earlier experiments on stainless steel [52]. A dense structure composed of stacking faults, twins, crystalline transformation from fcc to hcp, and

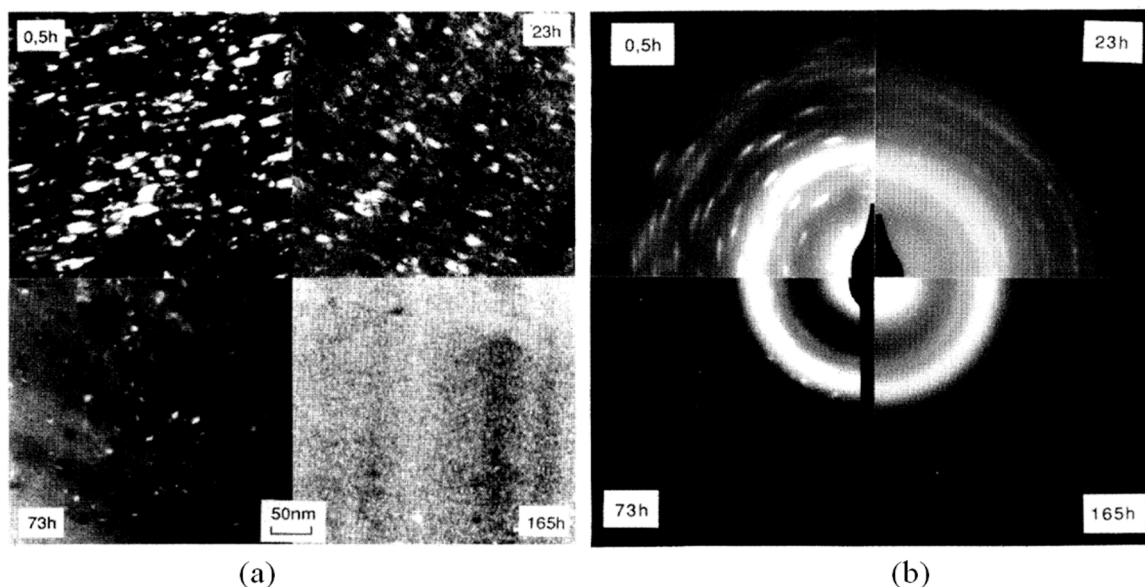


Fig. 14. (a) Dark field TEM micrographs of $\text{Ni}_{10}\text{Zr}_7$ milled at room temperature after 0.5 h, 23 h, 73 h, and 165 h; (b) corresponding electron diffraction patterns. Notice gradual amorphization [63].

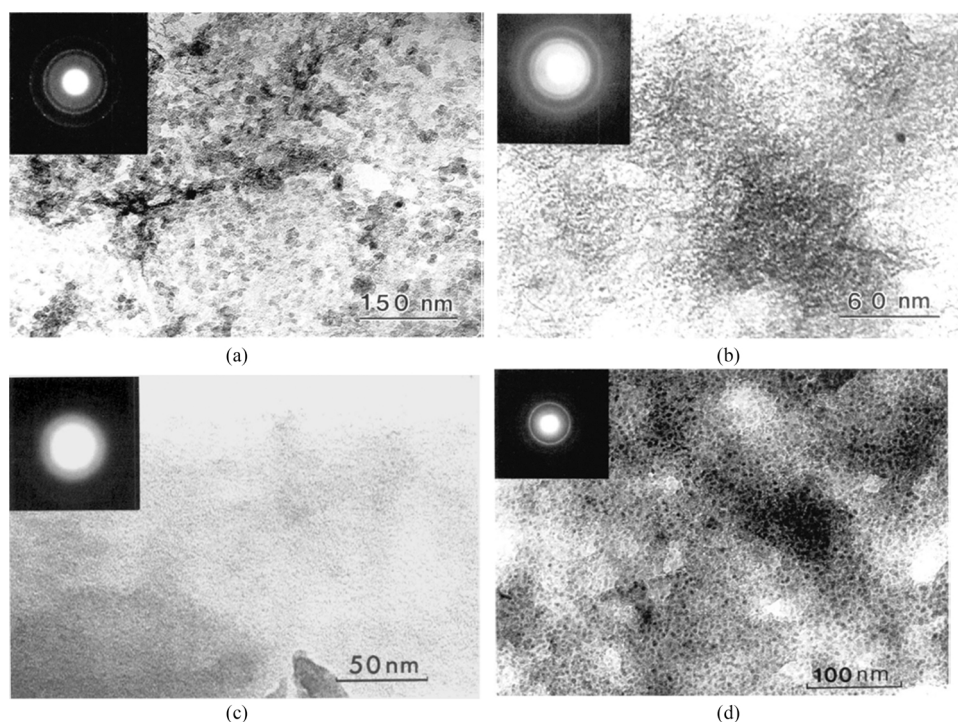


Fig. 15. (a)-(d) Bright field TEM micrographs of Ni_3Al powders milled after 5 h, 23 h, 50 h, and 50 h and subsequently annealed for 0.5 h at 450 °C [64].

amorphization was observed. The coordinated growth of stacking faults and twins along $\{111\}$ planes induced severely deformed regions, which can, at their intersection, rearrange into hexagonal packets; when the defect density reaches a threshold, they give rise to amorphous islands. As the deformation energy (defect density) increases, elastic deformation gives way to the generation and motion of dislocations, then to twinning, subsequently to phase transformations, and, in the end, in the extreme regime of high strain and high strain rate, to amorphization. The amorphization process can dissipate the large deviatoric stresses accumulated at the intersections of all kinds of crystalline imperfections, and thus inhibits the initiation and growth of nano cracks which could lead to failure. The amorphous phase should be harder than its crystalline counterpart because dislocations have no propagation path through the structure, a property also seen in bulk metallic glasses [58] and crystalline/amorphous nanolaminates [59–61]. Thus, amorphization is proposed as a deformation mechanism which helps to release the imparted strain energy. The boundaries between different deformation mechanisms can be loosely depicted by critical defect densities. These regions may have superior mechanical properties which potentially strengthen or toughen the material under extreme loading conditions.

3. Amorphization in intermetallic compounds

Amorphous alloys were formed by milling the crystalline $\text{Ni}_{50}\text{Zr}_{50}$ compound or the crystalline $\text{Ni}_{55}\text{Zr}_{45}$ alloy in a planetary ball mill [62]. In contrast, amorphous $\text{Ni}_{61}\text{Zr}_{39}$ can be generated by using a vibrating frame equipment. Thus, different milling methods can lead to different end products. The crystalline to amorphous transition of an alloy is an endothermic process. Milling can provide the energy required for this transition by introducing defects into crystalline compounds and breaking down crystallites in a powder particle, which increases their free enthalpy. When this free enthalpy exceeds that of the amorphous alloy, the crystalline compounds transform into the amorphous phase. Fig. 13 compares the enthalpy curves of the stable mixtures of two crystalline compounds and their amorphous alloy. The glass-forming range can be estimated from the difference in enthalpy between the two phases. When the increase in enthalpy is about 8 kJ/mol and Zr at%

is between about 40% and 50% amorphous alloys can be formed. Outside of this range the increase in enthalpy difference is not sufficient and a two-phase alloy consisting of amorphous and crystalline phases is formed.

Ni_xZr_y compounds [63] become fully amorphized when they are subjected to a milling intensity greater than a temperature and composition-dependent threshold. Milling intensity is defined as the amount of momentum transferred from the milling ball to the powder per unit mass per unit time. Below this threshold, a two-phase structure (crystalline and amorphous) is stable; and above this threshold the proportion of the amorphous phase increases with the milling intensity and decreases with increasing milling temperature. The intensity threshold increases with temperature and decreases with the hardness of the initial crystalline compound, which also controls the amorphization rate and the steady-state phase fraction in the two-phase equilibria. During milling, the environment of an atom changes in time due to two parallel mechanisms: thermally activated point defect jumps, as in classical thermodynamic equilibrium, and forced deformation such as shearing, powders sticking along new surfaces, etc. In Fig. 14 (a), the crystalline particles are distributed in an amorphous matrix, and the crystallites dissolve into the amorphous matrix until amorphization is fully achieved as milling time increases.

The fcc intermetallic compound Ni_3Al was subjected to mechanical milling in a high energy ball mill [64]. It transformed from an ordered fcc structure to a disordered fcc solid solution, and then to mixed phases of nanocrystalline and amorphous structure after continued milling. Milling of the fcc solid solution was dominated by the formation of dislocation cell structures which were refined into nanometer-sized crystallites. TEM (Fig. 15) showed an average grain diameter of 2 ± 1 nm for Ni_3Al powder after 50 h milling. This fine grain size is believed to lead to the crystalline-to-amorphous transition. The estimated free energy difference between the fcc and amorphous phases of Ni_3Al matched the calculated interfacial free energy of the grain boundaries.

One advantage of solid-state amorphization over its rapid cooling counterpart is that it does not restrict the dimensions of the final product, enhancing the ease of producing bulk amorphous materials. Ni-

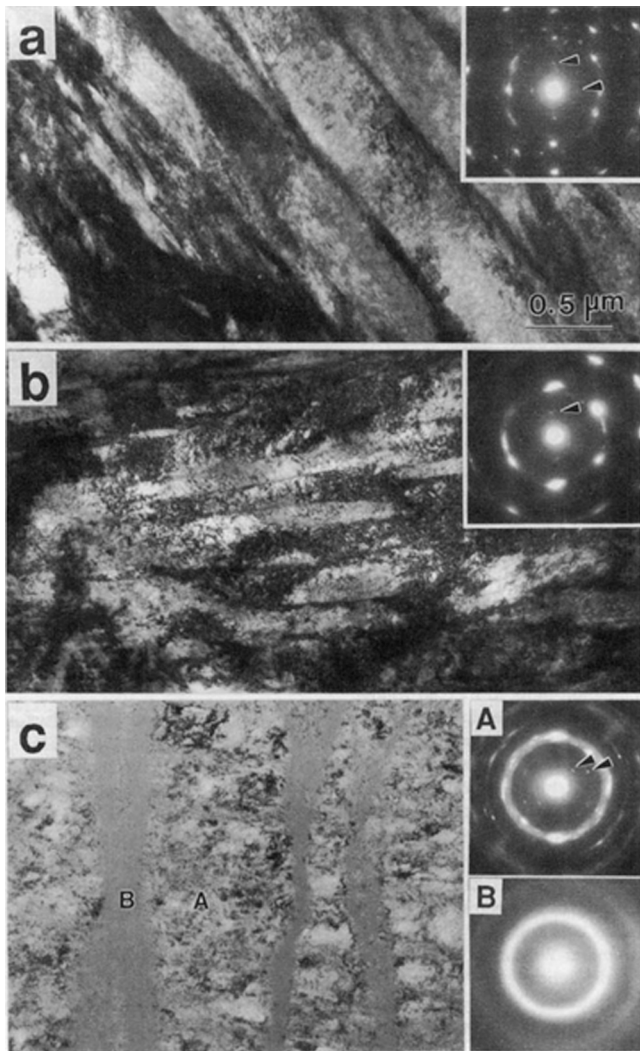


Fig. 16. Bright-field TEM micrographs and the corresponding diffraction patterns of (a) as-received, (b) 20% reduced, and (c) 60% reduced NiTi [65].

49.2 at% Ti alloy sheets were cold rolled at room temperature, generating a high dislocation density between 10^{13} and 10^{14} cm^{-2} , and suggesting that the accumulation of dislocations is a major driving force for the amorphization process [65]. The 60% reduced sample showed amorphous bands within the finely twinned crystalline matrix. Above 65% reduction, the sample fractured; the straight fracture surface was inclined $30\text{--}50^\circ$ to the compression direction. The TEM diffraction micrographs (Fig. 16 [65]) show both polycrystalline spots and a diffuse ring pattern, confirming the coexistence of crystalline and amorphous phases. The amorphous bands only extended in one direction and were not dependent on the orientation of the original twinned grains. Similar morphologies were observed in other heavily cold-rolled metals, suggesting that amorphous phases form in the shear band due to mechanical instability caused by the shear stress.

Nonequilibrium phases such as amorphous (Fig. 17) and intermetallic compound phases were produced and retained at the collision interface in the explosive welding of Ti/Ni clads [66]. There were crystalline particles D and E distributed in the amorphous phase identified by the diffraction patterns, Fig. 17 (d) and (e). These phases were formed by melting and rapid solidification of thin layers on the interface of both parent materials (Ti and Ni). The impact pressure generated by explosive welding promoted the formation of nonequilibrium phases such as the amorphous phase, indicating that shock processing has the combined features of rapid solidification, mechanical alloying, and

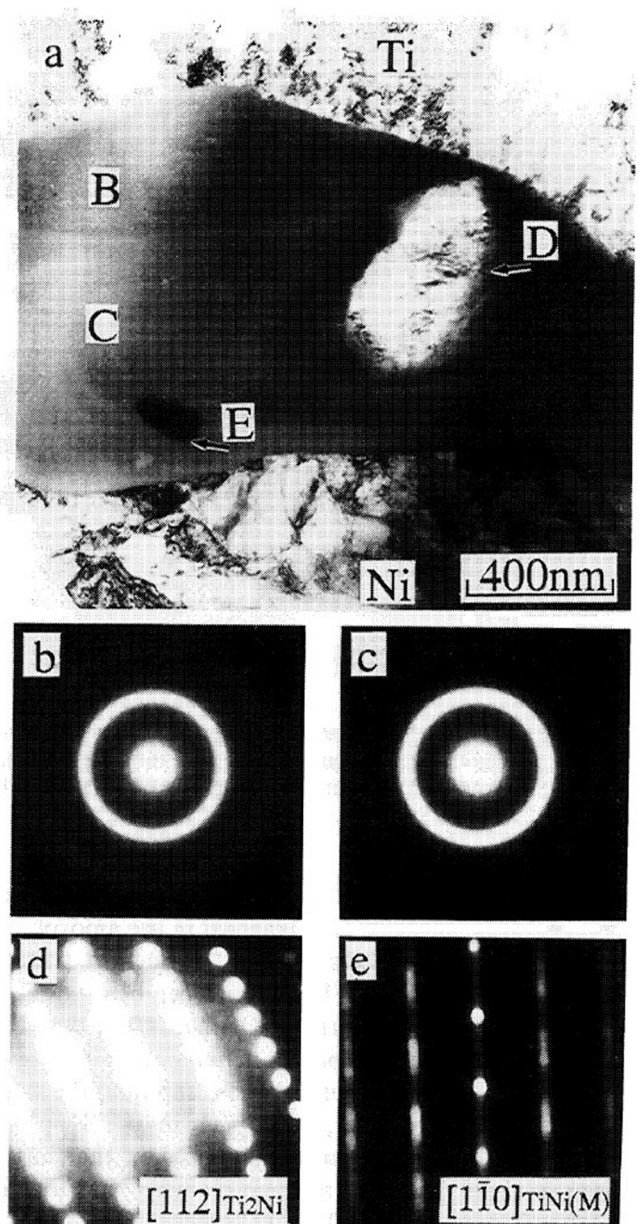


Fig. 17. (a) Bright field TEM image of collision interface in explosively welded Ti/Ni clad, exhibiting the formation of amorphous and crystalline phases. (b) to (e) Electron-diffraction patterns of the corresponding areas B to E in (a); B and C show amorphous regions and D and E show crystalline regions [66].

combustion synthesis, all of which facilitate the formation of nonequilibrium phases.

Amorphization was also observed in Nitinol (TiNi) subjected to high-pressure torsion [67,68], electron irradiation [69], ball milling [70], shot peening [71], and high-pressure extrusion [72]. High-pressure torsion (HPT) has been used as an effective method to produce bulk nanostructured materials with good mechanical properties [67]. As mentioned above, amorphization can be considered as an extreme case of refining grain size. The initial NiTi alloy (50.62 at% Ni and 49.38 at% Ti) disc sample had an austenite B2 (CsCl-type) structure with an average grain size of $30\ \mu\text{m}$. Torsion was applied to the TiNi sample at a 5 GPa pressure to a true strain of 7. Fig. 18 shows that most of the sample amorphized after the HPT. In agreement with the results obtained by Koike et al. [65], the sharp diffraction rings superimposed on an amorphous halo confirmed the presence of both nanocrystalline and amorphous phases, indicating that the amorphization transformation

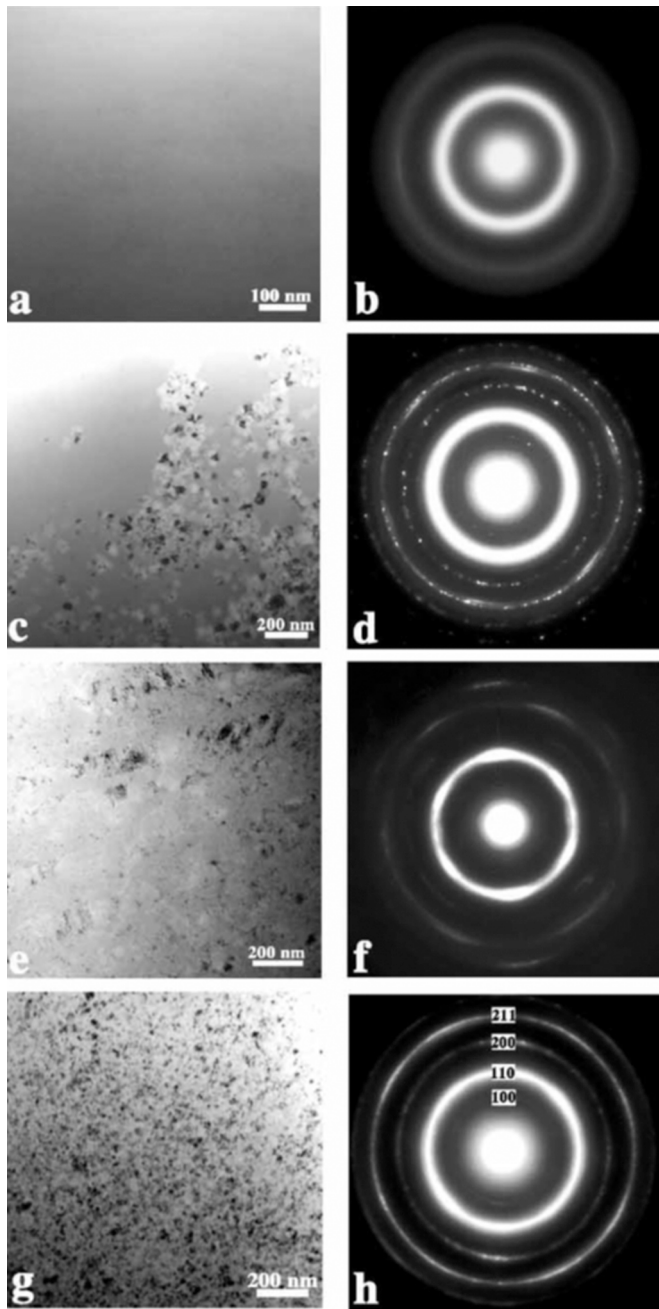


Fig. 18. TEM micrographs and the corresponding EDPs showing the coexistence of the amorphous nanocrystalline phases in TiNi subjected to high-pressure torsion [67].

under HPT is not homogeneous (Fig. 19). HRTEM micrographs show a disordered or amorphous phase originating from the dislocation core regions; amorphization was observed in both the interior of the grains and at the grain boundaries. This study concludes that the dislocations and grain boundaries both initiate the crystalline-to-amorphous transformation in TiNi.

Local canning compression of NiTi shape memory alloy subjected the material to a three-dimensional compressive stress state, which inhibited the initiation and propagation of micro-cracks and thus enhanced its plasticity [73]. Local canning compression can induce severe plastic deformation in NiTi alloy, leading to the formation of nanocrystallization or amorphization. At 25% reduction in height, dislocations and twins were observed. At 50% reduction in height, a small amount of nanocrystalline and amorphous phases occurred in the matrix

of NiTi, where the nanocrystalline phase was dominant. At 75% reduction in height, the amorphous and nanocrystalline phases were dominant, with a small amount of nanocrystalline phase distributed in the amorphous matrix (Fig. 20). Jiang et al. [73], proposed a sequence of microstructural evolution leading amorphization (Fig. 21). The sequence is essentially similar to other materials, with the added stress-induced martensite. Thus, one has the sequence austenite \rightarrow stress-induced martensite \rightarrow deformation twinning \rightarrow dislocation slip \rightarrow nanocrystallization \rightarrow amorphization.

Ultrasonic Nano-crystal Surface Modification (UNSM) is a method where a tungsten carbide tip is forced against a sample surface and vibrates at a high frequency, which leads to severe surface plastic deformation. Surface amorphization of the NiTi shape memory alloy was achieved by UNSM [74], which improved its hardness and thus significantly enhanced its wear resistance. TEM (Fig. 22) confirmed the amorphous nature by Fast-Fourier Transformation (FFT) and selected-area electron diffraction (SAED). Cell culture study also showed that the biocompatibility of the samples was not compromised by the UNSM process compared to the unprocessed samples. The high wear resistance and good biocompatibility suggests that UNSM is a potential process for creating better biomedical devices.

Nanocrystalline NiTi micropillars under uniaxial compression underwent plastic deformation mainly through localized shear band formation accompanied by large strain bursts [75]. Grains inside the shear band were reduced from 65 nm to 11 nm and even amorphized. The microstructural changes in the NiTi micropillars resembled those of bulk materials processed via macroscopic severe plastic deformation where a large plastic strain was imposed to obtain nanocrystallization. Fig. 23 (a) shows the surface morphology of the micropillar after plastic-deformation. Fig. 23 (b) is the bright-field TEM image, showing the shear band at 45° to the loading direction, which is the direction of the maximum shear stress. Inside the shear band (Fig. 23 (c)), the microstructure is a mixture of amorphous phase and nanograins as small as 11 nm, much smaller than the average grain size of the other parts of the micropillar (65 nm). The SADP of the shear band (Fig. 23 (c)) shows the coexistence of austenite (B2 lattice), martensite (B19' lattice), and amorphous phases. The refined 11 nm grains are more resistant to plastic deformation than the original 65 nm grains; as a result, the critical stress for bursts increases with the strain. Fig. 23 (d) is the illustration of the localized plastic deformation of the nanocrystalline NiTi micropillar. The experimental results indicate that micro-fabrication by severe plastic deformation could be a potential manufacturing technique.

High pressure torsion (HPT) is a suitable technique to deform brittle materials due to its quasi-hydrostatic loading condition which inhibits crack formation. In a ZrCu intermetallic compound [76], many shear bands nearly parallel to the shear direction were observed by optical microscopy after HPT deformation (Fig. 24 (a)). X-ray diffraction and TEM observation confirmed the presence of partial amorphization, localized within the nano-scale shear bands (Fig. 24 (b) and (c)). In the zone-melted Zr₅₀Cu₄₀Al₁₀, the amorphization was preferential in the ZrCu phase (Fig. 25), indicating that the initial martensitic structures played an important role in the amorphization process.

The interactions of dislocations with each other and other defects such as grain boundaries often result in strengthening of the material. Brittle failure occurs preferentially when dislocations are scarce. Another example of intermetallic compound is samarium-cobalt (SmCo₅) deformed by nanoindentation. For small grain sizes, the dominant deformation mechanism is grain boundary sliding, while for larger grain sizes, amorphous shear bands were found as well [77]. This unusual deformation mechanism leads to an inverse Hall-Petch (HP) relation of strength versus grain size which is opposite to the traditional HP relation observed in common metals. The HRTEM image (Fig. 26) shows a shear band without dislocations in its vicinity. FFT and its inverse patterns reveal that the shear band is amorphous while regions outside the band are crystalline. The amorphous shear band (about 2 nm

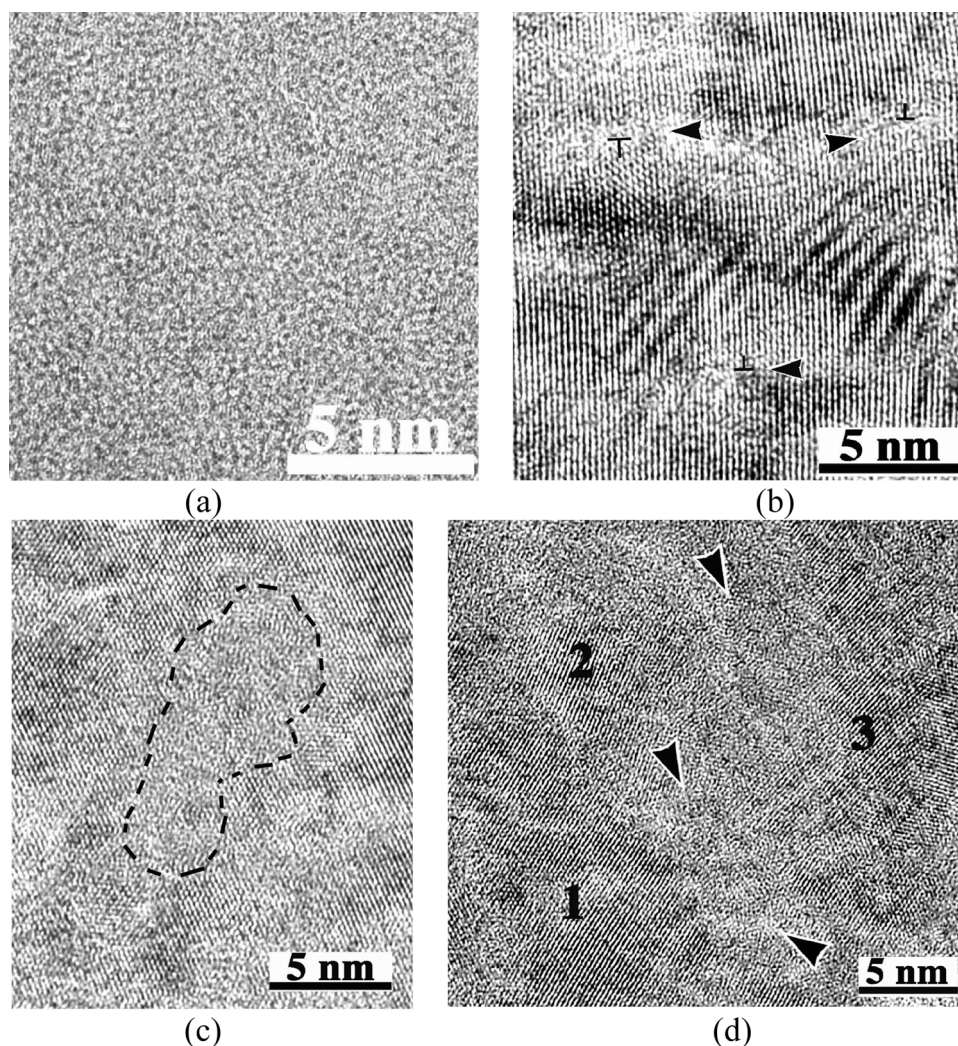


Fig. 19. HRTEM images of inhomogeneous morphologies (a) Amorphous phase. (b) Disordered regions originated from dislocation cores. Arrowheads denote the disordered regions. T or inverted T indicate edge dislocations. (c) Amorphous phase in the interior of a grain. (d) Amorphous phase at the grain boundaries. The numbers denote three grains, and the amorphous regions are indicated by arrowheads [67].

thick) in this case is the primary carrier for plastic deformation and is able to propagate in the grains without crack initiation. These amorphous shear bands in SmCo_5 inhibit fracture and increase the plasticity of the material. Two features are important for this mechanism to release the strain in the intermetallic compound: a high-energy barrier for dislocation glide and a low-energy barrier for amorphization. This deformation mechanism can be generalized to other intermetallic materials which generate similar amorphous shear bands when deformed.

4. Amorphization in covalently-bonded solids

Jeanloz et al. [78] were the first ones to observe, by TEM (Fig. 27), an amorphous phase within the crystalline matrix with a high density of dislocations in a single crystal of natural olivine ($\text{Mg}_{0.88}\text{Fe}_{0.12}$) $_2\text{SiO}_4$ disc sample subjected to 56 GPa shock pressure by multiple-reverberation for about 0.5 microseconds. The shocked sample had various degrees of deformation, and the amorphous zones were found within regions with the highest density of dislocations. Thus, it was concluded that amorphous olivine glass may form at shock compression above 50–55 GPa. Actually, olivine is partially ionic. The silica tetrahedra are covalently bonded and ionic forces connect neighboring tetrahedra.

Dislocation-free Si crystalline specimens were scratched on the chemically polished (001) surfaces by a diamond stylus along the [110] with a load of 2 g at the speed of 10 mm/s at room temperature. The

damaged zone consisted of a small amorphous zone distributed in a crystalline region with dislocations by TEM (Fig. 28) [79]. The transformation from crystalline to amorphous silicon was abrupt, creating a rough interface, while no polycrystalline layers or cracks were observed near the interface. Dents were not detected on the surface, nor cracks found near the scratch and the amorphous phase remained after removing the load. The driving force for the phase transformation is mainly the hydrostatic stress under high pressure testing. It was proposed that the very high shear stress generated by scratching resulted in the amorphization of the diamond cubic structure of the silicon crystal.

Fig. 29 shows TEM images of how amorphization in α -quartz initiates with forming planar defects and continues by the propagation of amorphous silica phase at these defect sites [80]. The thickness of the amorphous lamellae ranges from 1 to 100 nm. Similar microstructures have been found in quartz subjected to quasi-hydrostatic and non-hydrostatic compression, in diamond-anvil cells up to 40 GPa and from simple crushing as well. The geometric relationship between the crystalline and amorphous phases is consistent with the existence of a pressure-induced shear instability. The results suggest that there is a common deformation mechanism for solid-state amorphization in static and shock compression, meteorite impacts, and deformation by tectonic processes in the earth interior.

Cristobalite and quartz are both polymorphs of silicon dioxide (SiO_2). While cristobalite completely amorphizes between 22 and

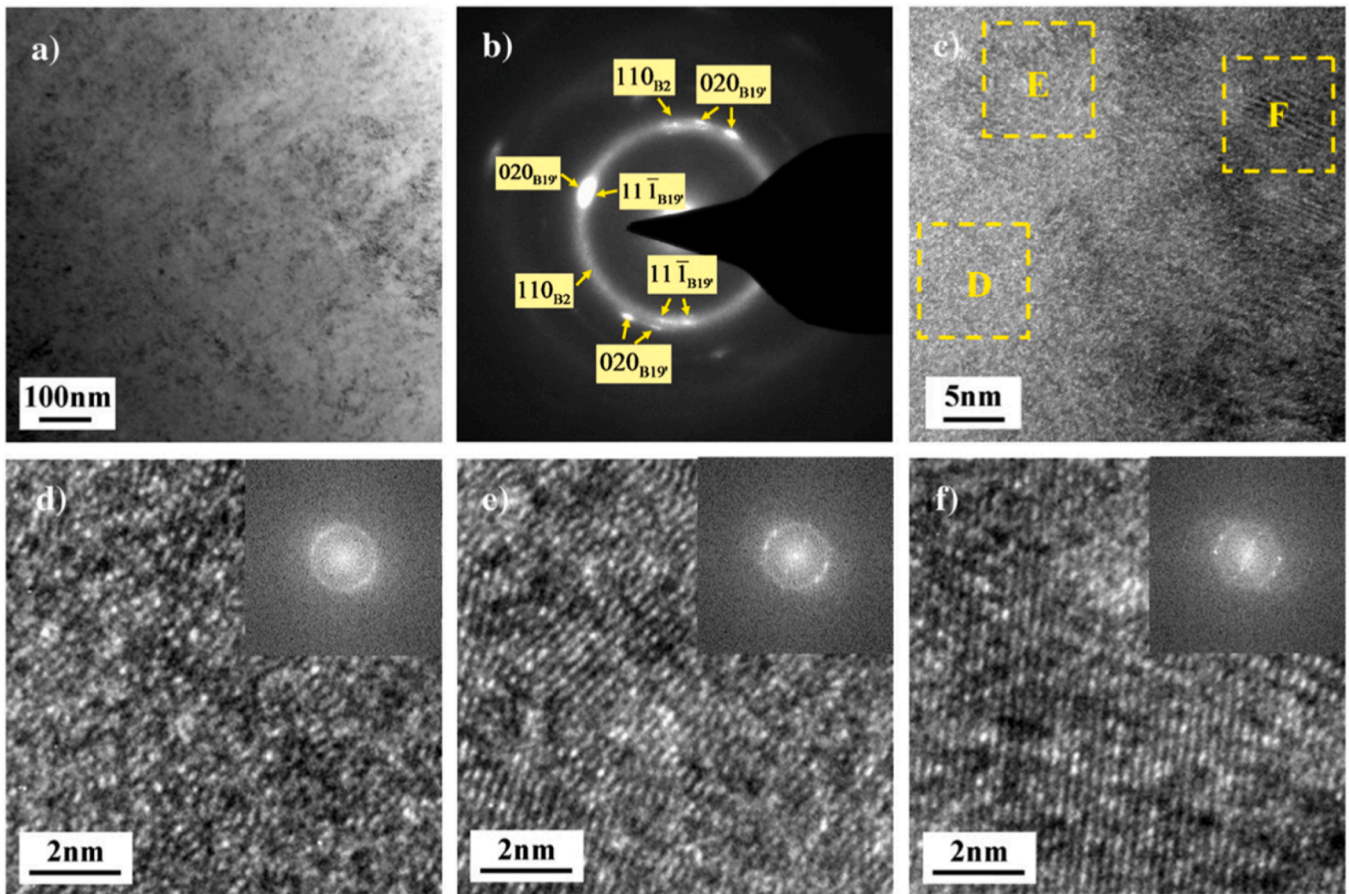


Fig. 20. TEM images of NiTi specimen deformed by 75% in height: (a) bright field image; (b) SAEDP showing the coexistence of amorphous and nanocrystalline phases, B2 austenite and B19' martensite; (c) HRTEM image exhibiting the retained nanocrystalline phase distributed in the amorphous matrix; (d) FFT of zone D in (c) revealing the amorphous nature; (e) FFT of zone E in (c) showing coexistence of amorphous and nanocrystalline phases; (f) FFT of zone F in (c) exhibiting dislocations and lattice distortion in nanocrystalline phase [73].

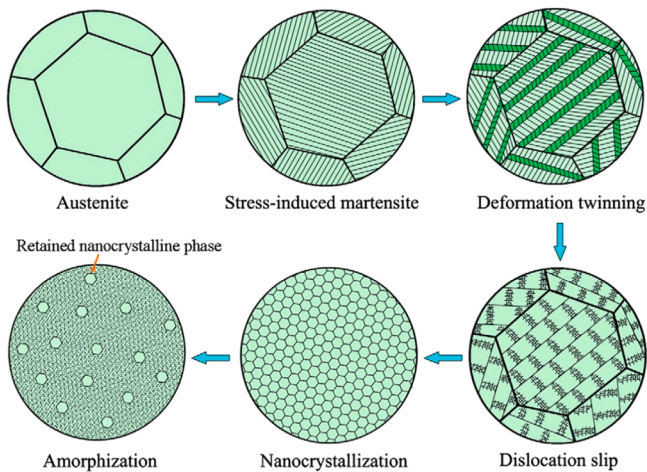


Fig. 21. Schematic diagram of microstructural evolution of nanocrystallization and amorphization of NiTi specimen under local canning compression [73].

28 GPa, quartz fully amorphizes between 35 and 40 GPa [81]. Although lamellar amorphization is common in shock compression of quartz, it was not detected in shocked cristobalite. Cristobalite is not available as large single crystals or aggregates, thus the experiments were performed on size-sorted powders with an average initial density of 62% encapsulated in a stainless-steel recovery capsule shocked by gas gun [81]. In

Fig. 30 (a), no evident Raman line shifts nor shock-induced features were found up to 22.9 GPa in cristobalite. TEM observations showed no sign of significant amount of glass. The decreased intensity and line broadening in the XRD and Raman spectra are probably due to the increase in twin density and extreme lattice bending. The specimen shocked at 28.2 GPa almost completely amorphized, with only less than 0.1% crystallinity. This specimen had a broader and weaker amorphous hump in XRD at $2\theta \approx 21^\circ$ (**Fig. 30** (b)), corresponding to a 0.40 nm interplanar lattice spacing. In contrast to shocked quartz, no distinctive shock-induced defects were observed in the shocked crystalline cristobalite grains. **Fig. 31** shows the interface between the crystalline and amorphous regions. Cristobalite amorphization did not follow twin boundaries, indicating twin strain energy did not have a large effect on amorphization. Both amorphous cristobalite and quartz have similar properties such as refractive indices and densities, as well as a similarly broadened Raman spectrum. They likely collapse to similar disordered structures under shock compression.

Another study investigated single crystals of α -quartz and α -berlinite (AlPO_4) compressed at different pressures at room temperature in a diamond anvil cell (DAC) [82]. Single crystal thin foils $\sim 30 \mu\text{m}$ thick of quartz and berlinite were optically polished before compression of different crystal orientations in DAC. There is a large pressure gradient, from ambient pressure at the rim to more than 30 GPa in the center. In quartz, the rim region remained crystalline with no signs of plasticity up to 5 GPa but some thin straight 10 nm amorphous lamellae were observed. At 10 GPa, quartz transformed to a two-phase mixture: the crystalline matrix had microcracks with inhomogeneous density, with the second phase thicker and more densely arranged lamellae with

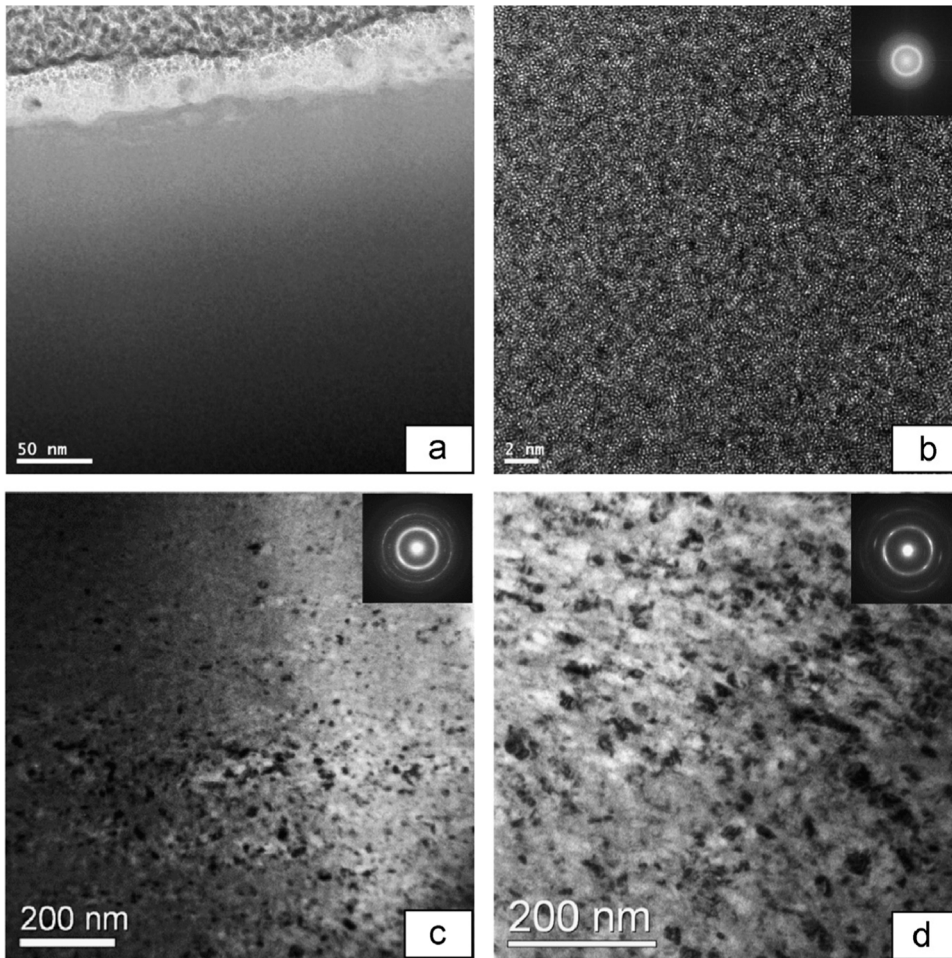


Fig. 22. TEM images on or near the surface of NiTi shape memory alloy after Ultrasonic Nanocrystal Surface Modification (UNSM) processing. (a) Top surface low magnification image; little contrast can be seen. (b) Top surface high-resolution image with corresponding FFT pattern; no long-range order observed. (c) Bright field TEM image and corresponding diffraction pattern at 4 μm below surface; partially nanocrystalline and partially amorphous at 4 μm below the surface. (d) Bright field TEM image and corresponding diffraction pattern at 7 μm below surface. Nanocrystalline nature increases with depth, become fully nanocrystalline at 7 μm below [74].

50–60 nm thickness (Fig. 32 (a)). Above 15 GPa, regions close to the center of the samples were mostly amorphous (Fig. 32 (b)). The crystalline regions were characterized by bend contours and gradually vanished at the boundaries (Fig. 32 (c)). Upon release, radial cracks formed. TEM images (Fig. 32 (d) and (e)) show veins filled with amorphous silica throughout the area. Berlinite was more ductile than quartz, with abundant dislocation activity induced by DAC. The recovered samples were heavily fractured, and diffraction patterns with spots and radial streaking indicated slightly (up to $\sim 10^\circ$) misoriented domains (Fig. 33 (a)). The diffuseness around the spot indicated that amorphization might occur. Indeed, thin amorphous lamellae were detected at lower pressures (2–5 GPa) in Fig. 33 (b). At larger pressures (5–10 GPa), thicker amorphous lamellae were observed. Above 10 GPa, most of the material was amorphous and slabs with sharp crystal-amorphous boundaries (Fig. 33 (c)) were formed. For quartz, this led to a two-stage amorphization process where shear lamellae first nucleated, then amorphized by the mechanical instability in the crystal. For berlinite compressed at a certain crystal direction, optical microscopy exhibited a large density of straight and thin lines throughout the specimen (Fig. 33 (d)). TEM showed that these lines were actually plastic slip lines caused by substantial dislocation density of up to $5 \times 10^{13} \text{ m}^{-2}$ (Fig. 33 (e)). At about 10 GPa in berlinite, thick amorphous lamellae developed in the densely dislocated areas, and eventually coarsened to complete amorphization. The lamellae orientation appeared to be crystallographically controlled and nucleated along planes with high shear stress because some of them became weakened under the shear stresses induced by the high pressure in both samples.

The mineral wollastonite (CaSiO_3) was found to amorphize at a pressure of 25.6 GPa at 300 K [83]. Energy dispersive x-ray diffraction

and Raman spectroscopy results showed the structure of CaSiO_3 . At high pressure and high temperature, the phase transition from crystalline wollastonite to perovskite was kinetically inhibited; therefore amorphization occurred instead (Fig. 34). It was also found that the perovskite phase became amorphous when released from high temperature and high pressure conditions. The activation energy barrier for this transformation prevented the formation of the wollastonite phase upon pressure release.

Serpentine, a common rock-forming hydrous magnesium iron phyllosilicate ($(\text{Mg,Fe})_3\text{Si}_2\text{O}_5(\text{OH})_4$) mineral, was observed with synchrotron radiation to undergo pressure-induced amorphization at 14–27 GPa and 200–300 $^\circ\text{C}$ in a multianvil apparatus (Fig. 35) [84]. When the temperature increased to 400 $^\circ\text{C}$ the mineral samples rapidly crystallized into high-pressure phases. This transformation is likely enhanced by high differential stress, which is similar to the effects of shear stress upon pressure-induced phase transitions found in olivine. It was concluded that amorphization of serpentine was an unlikely mechanism leading to deep-focus earthquakes because the temperature of subducting slabs was much higher than the temperature at which the rapid crystallization was observed in these experiments [85].

Chen et al. [86] were the first to observe shock-induced amorphization in boron carbide (B_4C) during ballistic testing. Armor-piercing projectiles with velocities between 750 and 1000 m/s impacted the B_4C composite laminates, producing pressures between 19 and 25 GPa. TEM micrographs (Figs. 36 and 37) show the impact tests results at 907 m/s (23.3 GPa) and 793 m/s (20.3 GPa), respectively. At higher impact velocity and pressure, amorphous bands were observed, while at lower velocity and pressure, planar faults such as microtwins and stacking faults were found instead of amorphous zones. These bands

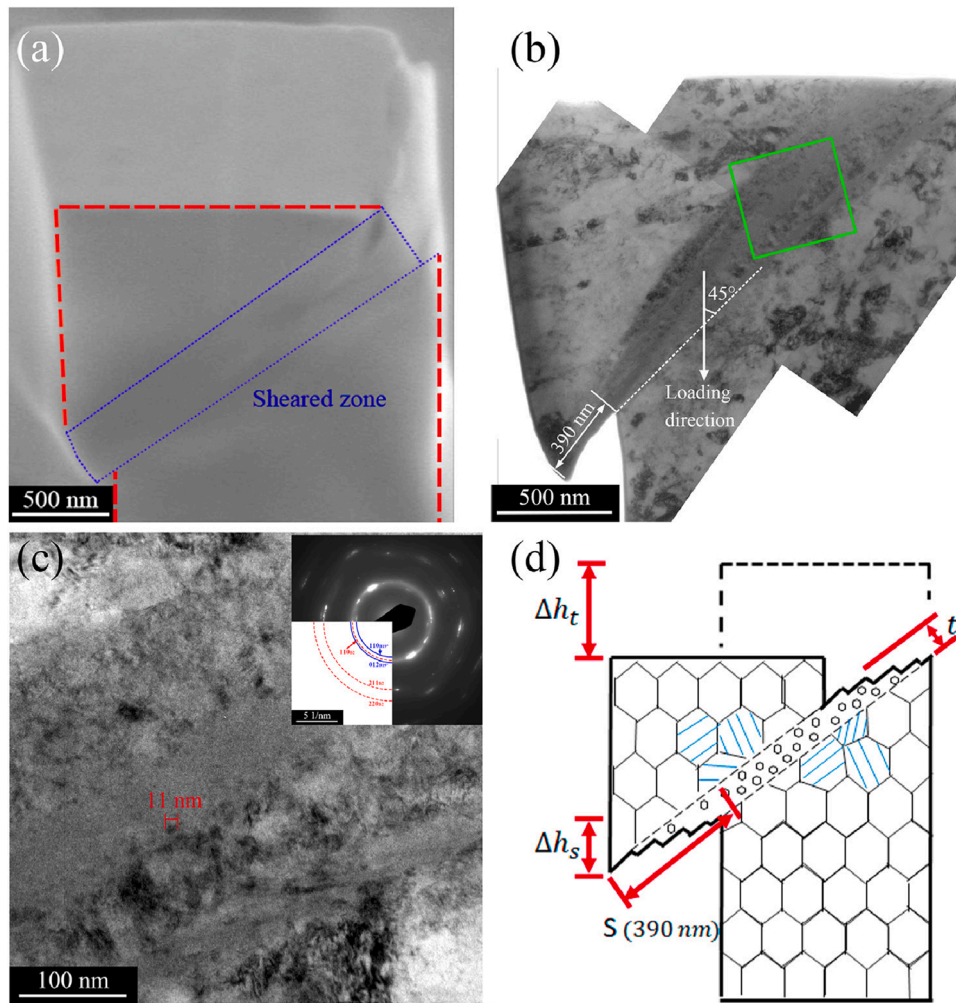


Fig. 23. (a) SEM image of the NiTi micropillar by plastic deformation, (b) TEM image of the localized shear band, (c) TEM image and the SADP of the green-boxed area in (b), and (d) an illustration of the plastic deformation of the nanocrystalline NiTi micropillar (blue lines represent the residual martensite) [75].

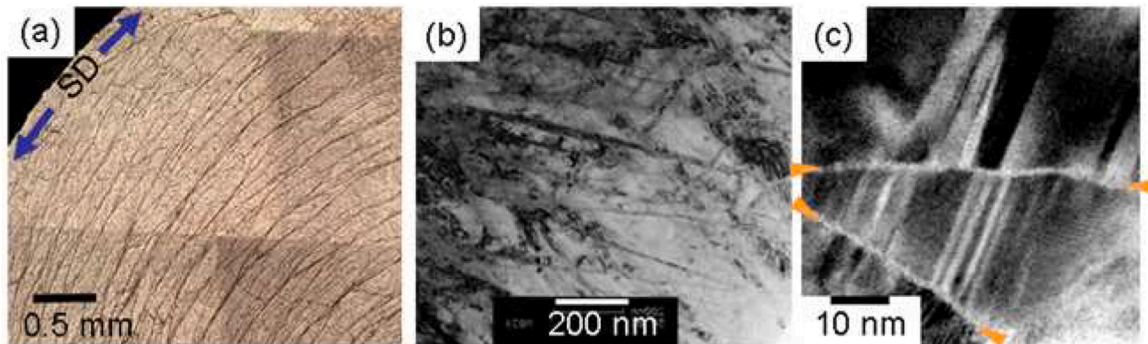


Fig. 24. Microstructures of ZrCu after HPT deformation for 30 turns. (a) Optical microscopy image. (b) TEM bright field micrograph. (c) HRTEM micrograph [76].

were 1–3 nm thick and only one band was observed in each grain, suggesting the complete amorphization was not achieved. Higher pressures may be required to complete the amorphization process, but the ballistic loading and resulting release of compression appeared to impede this process. The amorphous bands aligned closely with cracks and the uncracked bands extended into the B_4C grains, indicating that these amorphous zones may serve as crack paths for cleavage-like failure.

Another study on B_4C used quasistatic indentation to generate amorphization. Fine metallographic polishing and Raman spectroscopy

were combined to measure the spatial distribution of the amorphous zone under Vickers indentation (Fig. 38) [87]. The maximum amorphization intensity occurred just beneath the contact surface and decreased farther from the center. The amorphized zone was significantly smaller than the plastic zone, indicating that the threshold stress to initiate amorphization is higher than that for plastic deformation. It was argued that the amorphization in B_4C under a sharp indenter undermines the accuracy of its true crystalline strength as the area under the indenter immediately amorphizes upon contacting the indenter resulting in the measurement of a mix of amorphous and crystalline phases. The

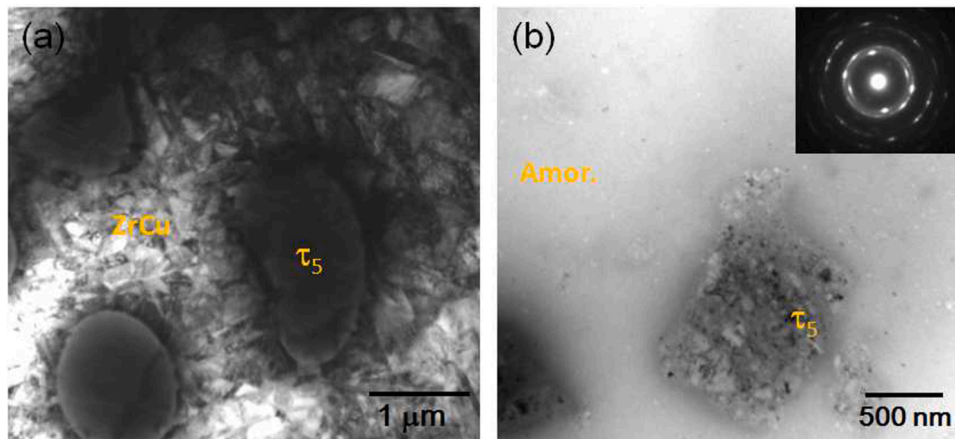


Fig. 25. TEM images of $Zr_{50}Cu_{40}Al_{10}$. (a) Before HPT deformation. (b) After HPT deformation ($N = 50$). Amorphized region shown in (b) [76].

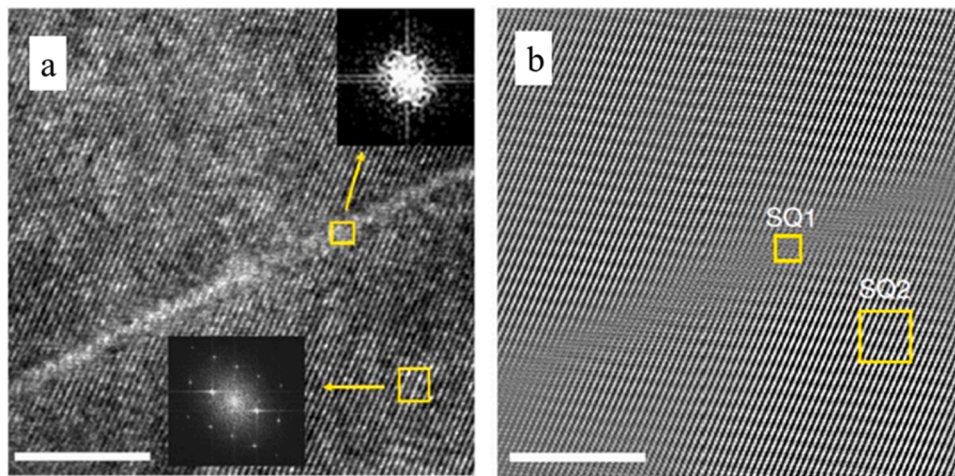


Fig. 26. Amorphous shear bands in nanoindentation deformed $SmCo_5$. (a) HRTEM image of a shear band and its vicinity and the FFT patterns. (b) The inverse FFT image. A blurred band corresponds to the amorphous shear band. Scale bars are 10 nm [77].

measured hardness values are lower than the true values for boron carbide because the amorphous B_4C is weaker and less resistant to penetration than the crystalline B_4C .

Although boron carbide has many superior mechanical properties, pressure-induced amorphization can disturb its crystalline order and weaken its shear strength [88]. Fig. 39 shows TEM observations of amorphous bands and a crack beneath indentation on a B_4C sample. Dislocations and lattice rotation were found near the amorphous zones. When grain sizes were refined, the tendency for amorphization was reduced, providing a potential method to minimize the effects of amorphization in B_4C .

Another study on B_4C examined the failure state related to stress-induced amorphization [89]. Microscopic observations showed that shear localized amorphization normally coexisted with stacking faults and twins. HRTEM micrographs (Fig. 40) support the amorphization deformation mechanism in B_4C and can probably be extrapolated to other ultrahard covalent materials. Dislocations have lower energy barrier for nucleation than that of the first-order phase transition; creating new dislocations or stimulating existing ones under high non-hydrostatic pressures is favored. Dislocation movements due to conventional lattice sliding were prevented by strong covalent bonds, and instead amorphization was initiated at the highly distorted symmetry-breaking dislocation cores. Fig. 41 is an illustration of this dislocation-mediated amorphization in B_4C , rather than direct phase transition from crystalline to amorphous structures. The measured

activation volumes, activation energies, and nucleation rates of two single-crystal B_4C samples were consistent with those of dislocation nucleation and significantly lower than that of the crystalline-amorphous phase transition. This mechanism could facilitate understanding failure in other ultrahard covalently-bonded materials under extreme loading conditions.

The combined results of the studies discussed above suggest that these localized amorphous bands can be another mechanism for high-rate deformation in B_4C and other materials.

Reddy et al. [90] reported shear-induced localized amorphization in boron suboxide generated by nanoindentation. The amorphous bands were orientated along the $(0\bar{1}11)$ crystal plane and had widths between 1 and 3 nm and lengths between 200 and 300 nm. Fig. 42 shows the STEM images of B_6O under the indented regions, with crack regions and shear bands indicated by black and white arrowheads. Many dislocations, rarely seen in the initial samples, were found near the deformation bands and microcracks, indicating that they likely play a role in the deformation process. The FFT pattern exhibited a diffuse halo, confirming the amorphous nature of the shear band. Inherent defects usually cause brittle failure of covalently-bonded materials with little plasticity. However, under extreme loading conditions such as shock or indentation, cracking is inhibited, and the material deforms through dislocation plasticity or phase transitions. Super-hard materials such as diamond, B_4C and B_6O have high Peierls stresses due to their strong covalent bonds, substantially inhibiting dislocation motion at low

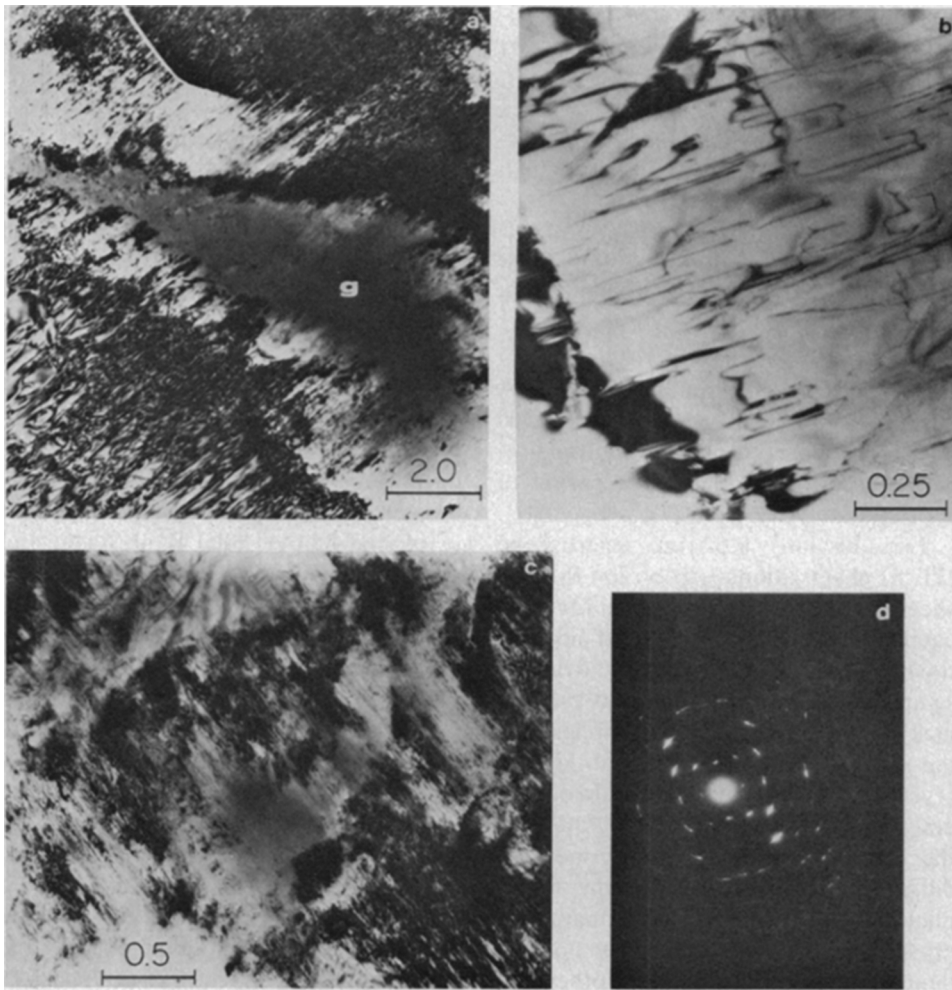


Fig. 27. (a) 200 keV Bright-field TEM images of shocked olivine. The area marked with a (g) is a nondiffracting amorphous zone within crystalline olivine (light areas) and contains a high density of dislocations. (b) 1 MeV Bright-field TEM image of shocked olivine showing dislocation densities as low-as 10^6 to 10^7 cm^{-2} , similar to those found in the starting material. (c) 1 MeV Bright Field TEM image of shocked olivine with amorphous patches (dark, no contrast) mixed with crystalline material of a high density of dislocations. (d) Electron diffraction pattern of the area in (c). Scales in micrometers [78].

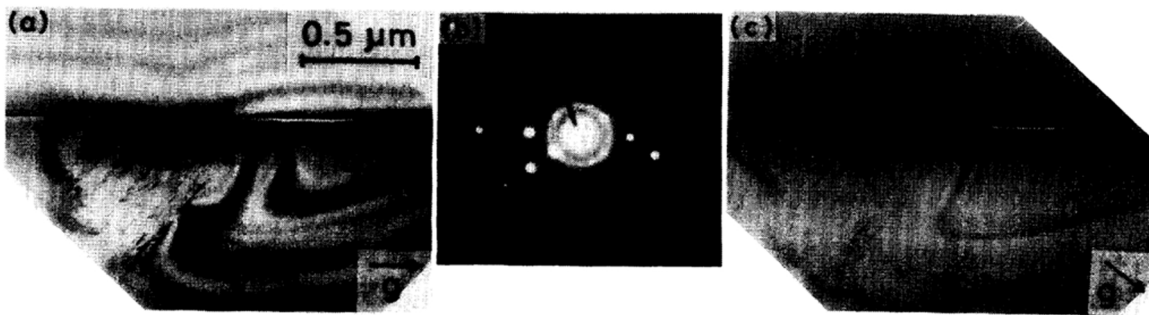


Fig. 28. Cross-sectional TEM images of the damaged zone by scratching (a) diffraction vectors g $[\bar{2}20]$ and (c) g $[\bar{2}22]$. (b) SADP of the damaged zone [79].

temperatures and leading to low fracture toughness. Even when crack propagation is inhibited it is difficult for these materials to deform plastically due to the inflexible covalent bonds. They may slip with dislocations and shear on relatively weak atomic planes, resulting in localized shear amorphization from the break in the local order and translational symmetry. The brittleness is not because of the rigid bonds breaking but shear-induced structural instability. While in other materials shear deformation usually produces plastic strains and reinforces a material's ductility, in highly anisotropic materials the sliding along weakly bonded crystallographic planes results in a collapse of the local structure and even failure.

Glassy carbon subjected to 50 GPa at room temperature in a diamond anvil cell and subsequently heated in situ via laser to 1800 K converts

into transparent “quenchable amorphous diamond” [91], which remains recoverable at ambient condition. Nanocrystalline diamond was observed at temperatures above ~ 2100 K. The initial glassy carbon was composed of randomly orientated fragments of curved carbon sheets. The high pressure and low temperature condition supply the energy for the sp^2 -to- sp^3 transition. The resulting local tetrahedral structure cannot form long-range tetrahedral order due to the low temperatures but forms the sp^3 -bonded amorphous diamond structure instead. During laser heating, when the sample transformed to transparent amorphous diamond, the temperature immediately decreased as a result of the poor laser absorption of the transparent phase, suppressing high temperature annealing which would lead it to the return to a crystalline phase. XRD, HRTEM (Fig. 43), and electron energy-loss spectroscopy (EELS) were

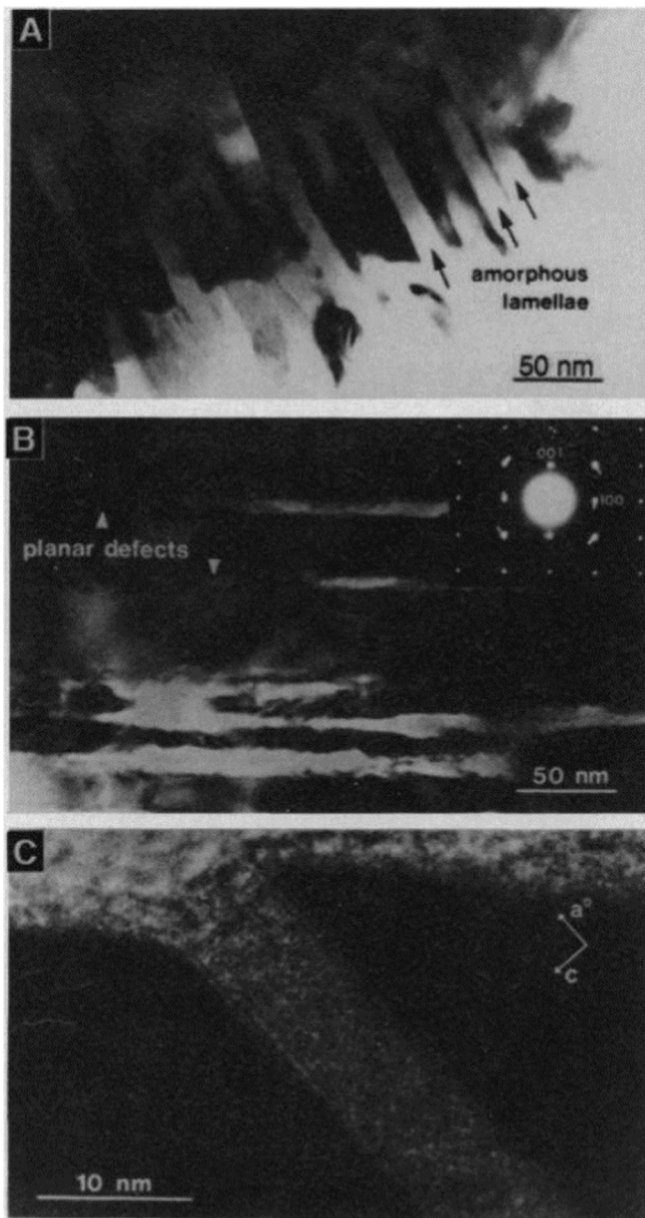


Fig. 29. TEM images of stress-induced microstructures in quartz. Planar defects are bounded by quartz, and the thickness of amorphous lamellae ranges from 1 to 100 nm. (a) Bright-field image shows amorphous lamellae (light bands, three indicated) and crystalline phase (dark areas) by compression between 21 and 25 GPa. (b) Nucleation and propagation of amorphous lamellae (light areas) on planar defects. SAED inset shows streaking and multiple spots. (c) HRTEM of amorphous lamellae in a crushed particle [80].

used to confirm the material's sp^3 bonding state and amorphous structure. This transparent amorphous diamond has the highest known density of amorphous carbon materials, with elastic stiffness comparable to crystalline diamond. The amorphous diamond is an isotropic, dense, transparent, super strong, and possibly superhard material.

Amorphous diamond with sp^3 bonding was also formed by laser heating glassy carbon at 50 GPa in DAC or shock compression of C_{60} to 55 GPa and 2000 K. By compressing C_{60} at about 27 GPa and 900–1000 °C, millimeter-sized amorphous carbon nearly completely sp^3 -hybridized was produced [92]. XRD patterns of carbon samples subjected to 20–27 GPa at 1000 °C show two broad and diffuse peaks, different from those of the starting fcc C_{60} precursor. Electron energy loss spectroscopy (EELS) spectra also confirms the sp^3 -hybridized nature

of the sample. Fig. 44 (a) is a low-magnification TEM micrograph of the jagged edge of an amorphous carbon sample, which has a similar fracture behavior to bulk glass. Fig. 44 (b) shows the HRTEM image of three-dimensionally organized carbon atoms with no long-range order. Amorphous features are characterized by diffuse halos of SAED patterns in the inset. In Fig. 44 (c), the inverse FFT of the HRTEM image shows many medium-range order (MRO) clusters randomly distributed in the sp^3 matrix, indicated by the orange boxes. The white dashed lines mark the 'crystal-plane-like' fringes of MRO structures similar to crystalline diamond in the inset. A larger interplanar spacing of ~ 2.2 Å than that of diamond (2.06–2.19 Å) reveals lattice distortion in the sample. The phase transition from collapsed fullerene to sp^3 amorphous carbon by heating is achieved by changing pressure and temperature conditions. Rapid quenching (about 500 °C s^{-1}) is also crucial to synthesize high-quality sp^3 amorphous carbon. In this study, the isotropic sp^3 amorphous carbon exhibits superior mechanical and physical properties, making it a potential candidate in different fields for amorphous solids.

Paracrystalline diamond has a well-defined crystalline medium-range order (MRO) of a few atomic shells. The paracrystalline state of diamond is distinct from both the crystalline or amorphous structures, consisting of sub nanometer crystals. It can be prepared with fcc C_{60} under high pressure and high temperature conditions [93]. The paracrystalline diamond is formed due to intensive nucleation sites in compressed C_{60} and by the second-nearest-neighbor short-range order of sp^3 bonding in amorphous diamond. Nanosized paracrystallites were distributed in the amorphous matrix as the crystalline MRO. In this study, an fcc fullerene C_{60} was compressed to 30 GPa at 1200–1800 K. HRTEM images show no long-range order nor lattice fringes, suggesting the disordered structure of the samples at about 1 nm (Fig. 45). Its amorphous nature is confirmed by the diffuse haloes in the FFT patterns. HRTEM images reveal a large number of ordered clusters of 0.5–1.0 nm size for samples annealed at 1400–1600 K. Lattice fringes approximately along the [110] and [010] zone axes of cubic and hexagonal diamond are identified within a 1 nm scale. The FFT patterns of the selected regions match cubic and hexagonal diamond, although both are highly distorted as indicated by the deviation of inclusive angles. The morphology of this paracrystalline diamond is different from amorphous diamond, characterized by the dominant formation of crystalline MRO clusters. Continuous random network type amorphous diamond has strong short-range order in the first two atomic shells, which substantially helps the development of MRO and diamond paracrystallites. The orientational sp^3 bonds between C_{60} units provide abundant nucleation sites, and the single-walled carbon nanotubes with well-arranged carbon bonds may supply sufficient sp^3 bonding sites for the formation of paracrystalline diamond contribute to new mechanical and physical properties and oxidation resistance, suggesting potential new applications for ultrahard materials.

Four covalently bonded materials (Si, Ge, SiC, and B_4C) were shocked using high energy lasers by Zhao et al. [94,95]. All four solids exhibited amorphization at pressures above specific thresholds. These four materials all have a negative Clapeyron slope, with the liquid having a higher density than the solid phase. The same effect should apply to amorphization, which is aided by both hydrostatic compression and shear. The rationale proposed by Patel and Cohen [96] and further developed by Levitas [97] was applied to the amorphization and the thermodynamics was explained. The post-shock TEM images (Fig. 46) reveal that the newly formed amorphous materials have a shear-band like morphology, which suggests that shear stress dominates this process. The threshold for amorphization depends on the strength of the material. The thickness of these shear bands is in the nanometer range, compatible with the extreme short durations of the shock pulses created by lasers

The mechanical coupling between Earth's lithosphere and asthenosphere depends on the mechanical properties of olivine-rich rocks of its

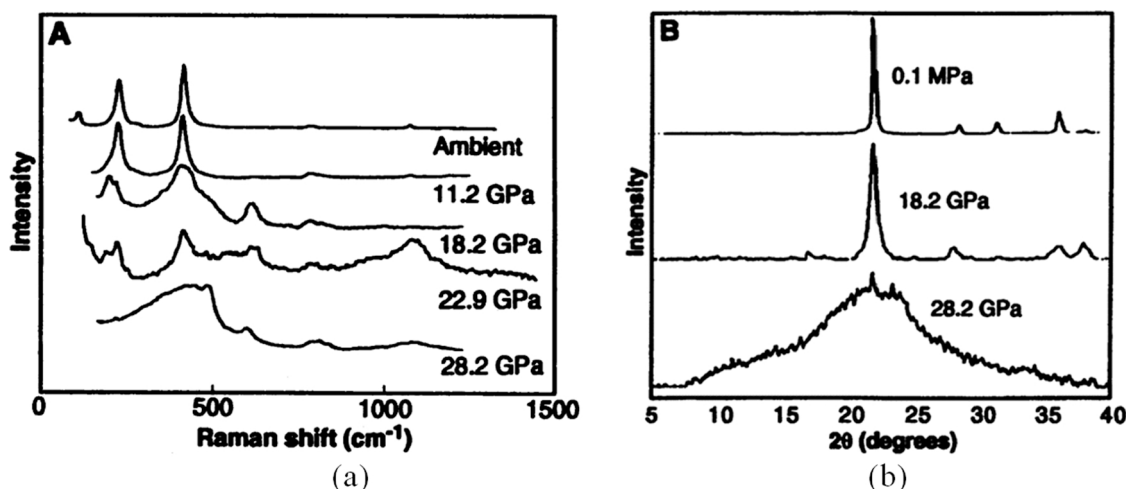


Fig. 30. (a) Raman spectra and (b) XRD patterns of cristobalite. Below 28.2 GPa, no significant line shifts or signs of amorphization in Raman or XRD with only a broadening and weakening of the characteristic peaks. At 28.2 GPa, broadened Raman lines and an amorphous hump in XRD pattern, indicating amorphous phases formed [81].

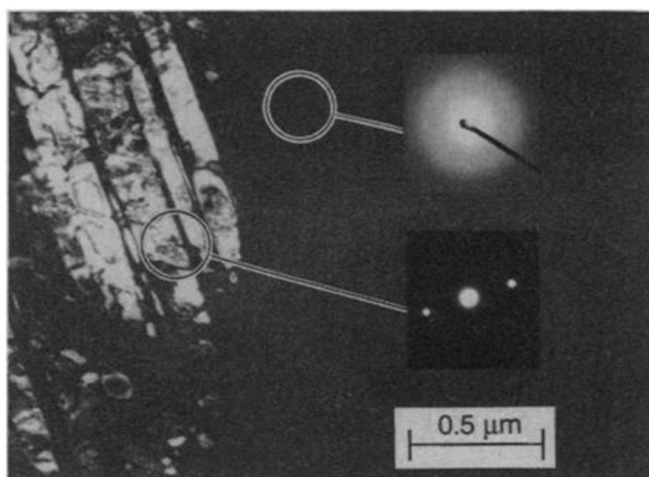


Fig. 31. Crystalline-amorphous border in cristobalite shocked at 28.2 GPa. Diffraction patterns show the sharp contrast between crystalline and amorphous regions separated by boundary of a few hundred nanometers. No amorphous lamellae are observed, which typically exist in shocked quartz [81].

upper mantle. In conventional crystalline materials, dislocation motion plays an essential role in plastic deformation. However, olivine does not have sufficient slip systems to accommodate all the strain conditions; thus, supplementary deformation mechanisms are required. Figs. 47 and 48 [98] show that in forsterite, the magnesium-rich end member of olivine solid solution series, amorphization forms at grain boundaries under static compression; the onset of its ductility was attributed to the activated mobility of grain boundaries in these amorphized layers. This could be one mechanism for plastic deformation of rocks deep within the Earth where such high stress conditions occur.

5. Amorphization in ionic materials

Several ionically bonded compounds exhibit amorphization. Among them, $\text{Ca}(\text{OH})_2$, commonly used to produce lime aggregate (by adding sand) and as a flocculant in the food industry, and resulting from the reaction of CaO and water, is attractive. Static compression of this simplest structure, among hydrous minerals, produces amorphization. $\text{Ca}(\text{OH})_2$ portlandite samples were compressed up to 37.6 GPa in a diamond anvil cell at room temperature [99]. In Fig. 49, between 10.7

and 15.4 GPa, the X-ray scattering disappeared, which indicates that amorphization occurred. At pressures above 10.7 GPa, a diffuse, low-intensity amorphous hump at 2θ of about 14° appears. This amorphous structure is retained up to 37.6 GPa. Upon the release of compression, the diffraction lines reappear between 5.1 and 3.6 GPa, revealing a reversible crystal-amorphous transition although with considerable hysteresis. The c direction is most compressible from 0 to 10.7 GPa due to the highly anisotropic elastic properties of crystalline $\text{Ca}(\text{OH})_2$. $\text{Ca}(\text{OH})_2$ is composed of sheets of $\text{Ca}(\text{OH})_6$ octahedra with hydroxyls hexagonally close packed surrounding the Ca^{2+} cations. The bonding between these sheets is weak hydrogen bonds. Strain in the a direction requires the Ca-O bonding to be compressed; however, the c direction can accommodate all strains by compressing the $\text{OH}\cdots\text{O}$ bonds for hydrogen bonds are weaker than ionic or covalent bonding of the same bond length. Hydrogen bonding can lead to large anisotropies in the elasticity of hydroxides, and therefore limits the understanding of the compression mechanisms in other complicated hydroxides prepared at high pressures.

Calcium phosphates are valued clinical and biocompatible materials and have been used widely in dentistry, prosthetics, and bone augmentation fields. Calcium phosphates are comprised of loosely packed polyhedra at ambient pressure, in different formations. In hydroxyapatite (HA), hydrated tricalcium phosphate (HTCP), and α tricalcium phosphate (α TCP), the polyhedra are arranged in chains. In dicalcium phosphate dihydrate (DCPD), they are in a layered structure, and in dicalcium phosphate anhydrous (DCPA) they are arranged as interconnected chains. The phosphate groups do not share corners or edges but are instead held together by cations and H_2O molecules. Calcium phosphate samples of 0.45 mm thick discs were compressed up to 10 GPa for 72 h in a Bridgman anvil; then X-ray diffraction (XRD) and Fourier transform infrared (FTIR) spectroscopy [100] were applied. These compounds amorphized at a 10 GPa pressure, with significant changes in the infrared spectra except DCPA. These changes are due to the lowering of site symmetry upon amorphization. At high pressures, HTCP, HA and α TCP began to collapse along their chain axes. HA and α TCP amorphized at around 10 GPa, while HTCP amorphized at only 2 GPa. These three compounds exhibit similar infrared spectra of the PO_4 group. The sheet structure of DCPD and DCPA collapsed in the sheet plane during the amorphization process, exhibiting low symmetry and similar PO_4 absorption bands.

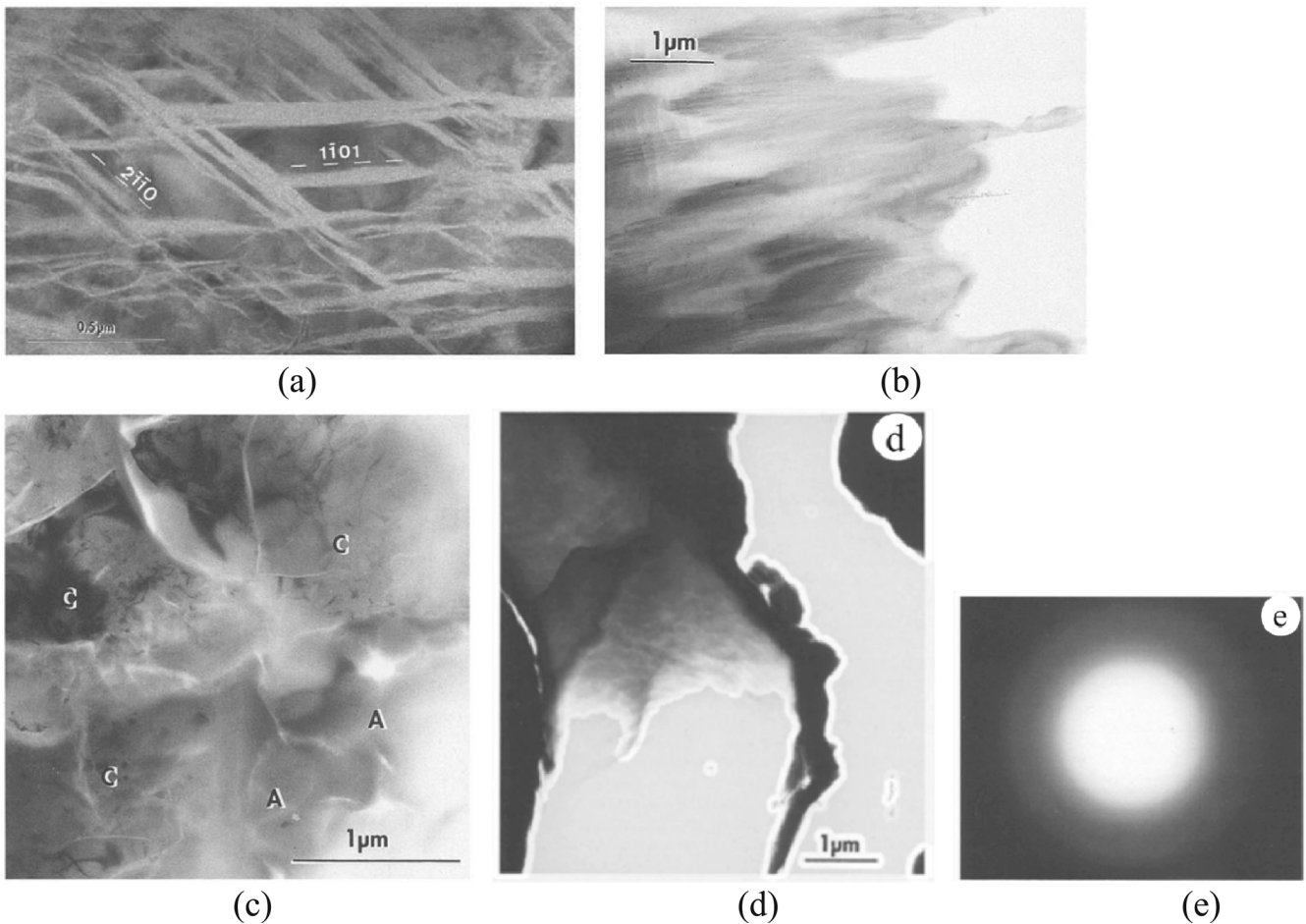


Fig. 32. TEM micrographs of quartz. (a) Dark field image. Amorphous lamellae appear in white. (b) Bright field image. Completely amorphized region. (c) Transition zone between amorphous and crystalline phases. Crystal region is characterized by the bend contours that vanished at the crystalline-amorphous boundaries. "C" for crystalline and "A" for amorphous. (d) Bright field image. Amorphous region with a radial crack. (e) Diffraction pattern of (d) [82].

6. Amorphization in biological materials

We have seen previously that many synthetic materials amorphize in extreme regimes such as high strain rate and high strain conditions. Section 5 discusses HAP amorphization; there is one example of a biological material undergoing amorphization: biogenic hydroxyapatite (HAP).

The impact surface of the fast-striking dactyl club of the mantis shrimp is a rare example of a natural material undergoing such extreme conditions [101]. Its dactyl club can generate forces up to 1500 N via acceleration above 10,000 g and velocity of 23 m/s. The club experiences extremely high loadings and needs to remain intact during the shrimp's feeding activities. It has evolved the special structure to localize damage and avoid catastrophic failure from high-speed impact. The outermost layer, i.e., the impact surface, of densely packed (about 88 vol%) ~65 nm bicontinuous hydroxyapatite (HAP) nanoparticles distributed within an organic framework is worn away on impacts and serves as the primary way to dissipate energy. Dactyl club samples were impacted at high strain rates (about 10^4 s^{-1}) with and without the outer protective layer. In the sample without the protective layer, penetration depths were twice compared to the one with it. It is possible that chitin and proteins interpenetrating in the nanoparticles harden, resulting in the localization of the failure and nanoparticles, therefore limiting the propagation of cracks. In this way, the organic network enables additional toughening and abundant damping. Although quasi-static indentation does not change the size and shape of HAP particles, they rotate, translate, and fracture into smaller primary grains of sizes

between 10 and 20 nm whereas the nanocrystalline networks crack at low-angle grain boundaries, generate dislocations, and then amorphize to dissipate some impact energy. Fig. 50 shows the TEM images of the impact surface of dactyl club and the illustration of its toughening mechanisms. This localized fracture and amorphization minimize the damaged zone to the renewable outer surface nanoparticle coating of the dactyl club.

7. Thermodynamics and kinetics of amorphization by deformation

We mention in Section 1 the different methods by which mechanical loads can be applied to metals in order to amorphize them. In this section we will present a general framework for amorphization by mechanical means. A simple criterion is:

$$G_c + G_d > G_a \quad (4)$$

where the subscripts c and a refer to the crystalline and amorphous form, respectively, and d corresponds to defects (from deformation or radiation effects). Fig. 13 of enthalpy vs. composition for the Ni-Zr alloys shows the difference between the amorphous (higher) and crystalline (lower) enthalpies. This difference is around 8 kJ/mol. However, Koch [102] estimated that the dislocations only account for about 1–2 kJ/mol. Thus, other effects must be considered. An important one is the destruction of order in intermetallic compounds due to plastic deformation. Phase transitions have thermodynamic parameters associated with them, as do internal interfaces formed by deformation and

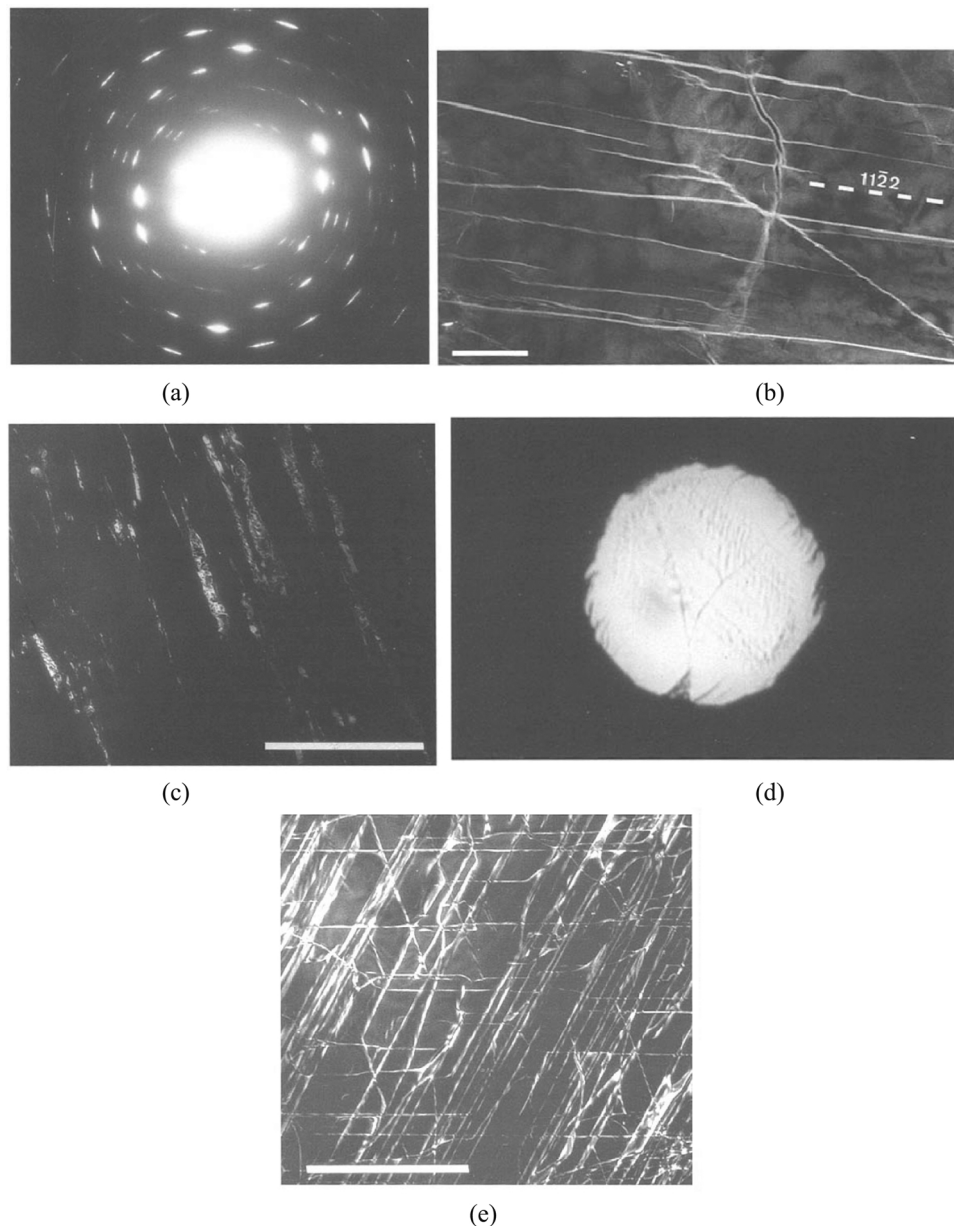


Fig. 33. TEM micrographs of berlinite. (a) EDP shows misoriented domains with diffraction spots surrounded by radial streaking. The diffuse central spot indicates the presence of amorphous phase. (b) Dark field image of thin amorphous lamellae with amorphous zone in white. Scale bar: 0.5 μm . (c) Dark field image of largely amorphized area with crystalline zone in white. Scale bar: 1 μm . (d) Optical microscopy image. (e) Dark field image of dislocations. Scale bar: 1 μm [82].

phase transitions. Thus, a more general expression is:

$$G_c + G_d + G_o + G_{gb} + \Sigma G_{pt} > G_a \quad (5)$$

where G_o is the free energy of disordering, G_{gb} is the energy of the additional interfaces generated by deformation or radiation, and ΣG_{pt} is the free energy increase from phase transitions.

External parameters are the stresses applied to the material, which can be decomposed into hydrostatic and deviatoric (or shear). In a more general formalism, we also need to consider the activation energy that represents the height of the energy that has to be overcome for amorphization to take place.

There exist theoretical analyses of this class of structural transitions in different degrees of complexity. The Patel-Cohen [103] and Eshelby [104,105] treatments provide an underlying energetics justification for the combined effects of hydrostatic and shear stresses on the thermodynamics. Levitas [106] provides a comprehensive theoretical

framework for this effect, incorporating the effects of external, internal, and transformation (Eshelby) stresses and strains on the structural changes. Indeed, the shear strains produced by shear stresses generate greater relative atomic motions than hydrostatic stresses and strains in shock compression. The expression for the work per unit volume, W , of a transformation for a stress state where only normal stresses operate in the unit cube aligned with the deformation direction (Fig. 51) [95] can be written as:

$$W = \sigma_0 \varepsilon_t + \tau \varepsilon_s + G_d + G_o + G_{gb} + \Sigma G_{pt} + \gamma A \geq \Delta G_a(T) \quad (6)$$

where ε_t is the spherical compression strain generated by the change of crystalline to amorphous phase and ε_s the deviatoric component of strain in a stress-free transformation, σ_0 is the hydrostatic stress $((\sigma_{11} + \sigma_{22} + \sigma_{33})/3)$, ε_s is the shear strain generated by the change of crystalline to amorphous phase. The term G_d represents the energy per unit volume of the local defect structure ($=\rho^d G_b^2/2$, where ρ^d is the local density of

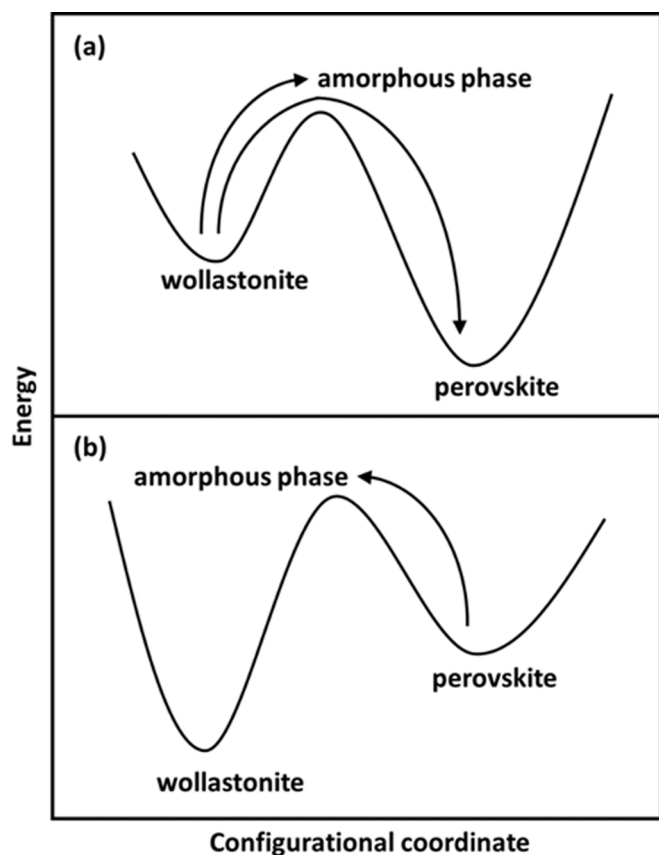


Fig. 34. Energy vs configurational coordinate diagram of the relative stabilities of the wollastonite and perovskite phases of CaSiO_3 . (a) At pressures > 17 GPa, perovskite is stable. Wollastonite transforms to perovskite at high pressures and high temperatures, indicated by the long arrow. (b) At ambient pressure, wollastonite is stable. When release the pressure and at ambient temperature, perovskite becomes amorphous because the transformation to wollastonite is inhibited, indicated by the short arrow in (b) [83].

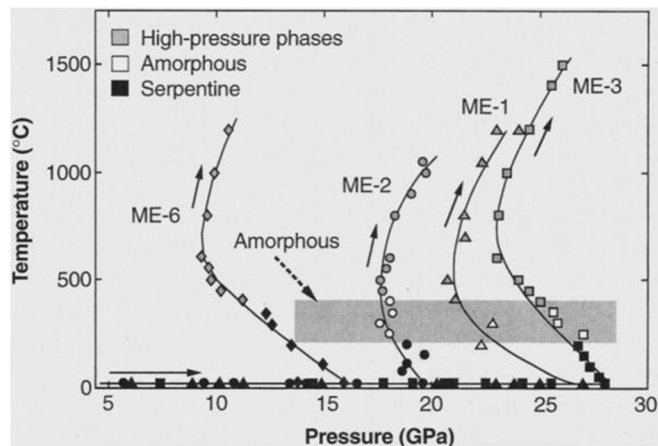


Fig. 35. Summary of the experiments on the amorphization of serpentine. Amorphous zone indicates the T-P conditions where amorphization of serpentine was observed with no high-pressure crystalline phases formed. Initial materials were Antigorite for ME-1, ME-2 and ME-6, and lizardite for ME-3 [84].

dislocations prior to amorphization, G is the shear modulus, and b is the Burgers vector). Several terms are added to Levitas' equation: the energy change for phase transitions, the energy of the grain boundaries

produced by extreme deformation, G_{gb} , as well as γ , the interfacial energy (A being the interfacial area between the amorphous and crystalline region). Here, $\Delta G_a(T)$ is a critical temperature-dependent value of the energy per unit volume that has to be overcome for the transformation to take place (activation energy). We apply it here to amorphization.

There is no unanimity nor need to be about the relative importance of the various contributions presented above. It is known that the extensive plastic deformation taking place during the deformation of powders of different compositions in ball milling, forming multilayers with high density of defects is an attractive method to generate amorphous compounds through the reaction of the elements. This was first done by Yermakov [107] and later by Koch et al. [108]. There are two classes of experiments, according to Koch [102]: *mechanical alloying*, where powders of different metals are milled together. At some critical deformation, diffusion couples form between the thin slivers that are highly deformed. The second one is *mechanical milling* where the powders have the same composition.

Cho and Koch [51] used ball milling to generate amorphous Nb_3Sn from crystalline $\text{Nb}+\text{Sn}$, $\text{Nb}+\text{NbSn}_2$, and Nb_3Sn . They conclude that the free energy of disordering contributed ~ 5 kJ/mol whereas the energy of the grain boundaries for a grain size of 5 nm contributed ~ 7 kJ/mol. These two contributions almost reach the 15 kJ/mol difference between the amorphous and crystalline structures. Donovan et al. [109] measured the enthalpies of the crystalline to amorphous transition in Si and Ge and obtained values of 11.6 and 11.9 kJ/mol. Weeber and Bakker [62] calculated the difference in enthalpy for Ni-Zr alloys and obtained values around 8 kJ/mol at the composition $\text{Ni}_{50}\text{Zr}_{50}$. These values are shown in Fig. 13. These values for the enthalpies of amorphization are consistent and provide a good guideline for the energy input required to amorphize materials.

Szlufarska et al. [110], using MD, predict that amorphization under a nanoindenter in SiC was the result of dislocation interaction, specifically the coalescence of loops generated by the high stresses. The experimental results by Wu et al. [111] are somewhat different: they observe a direct amorphization of 6 H-SiC under the nanoindenter coinciding with the first 'pop-in' of the loading curve. Subsequent 'pop-ins' are the result of amorphization triggered by dislocations.

One may argue that the deformation is not homogeneous but distributed in bands that have high dislocation densities, whose energy can locally reach high levels. This is accentuated by the intersections of these slip bands, essentially doubling the energy.

Although the exact mechanism of deformation-induced amorphization is not yet known, some thoughts, applicable to low stacking-fault energy materials, are advanced below. Fig. 52 [57] shows a general deformation sequence in a low stacking-fault energy alloy or compound starting with the generation of stacking fault packets (A) which then form on different planes (B) and intersect (C), forming phase transitions (D) which eventually amorphize (E). This example shows that dislocation energy and the increase due to a phase transition can generate sufficient energy to overcome the energy barrier ΔG_a in Eq. 6 and can promote amorphization. Idrissi et al. [112] comment at length on possible sequences leading to deformation-induced amorphization, including grain-boundary sliding. Thus, our knowledge in this domain is far from complete.

7.1. Kinetics of amorphization

There are no theoretical or experimental efforts, to the authors' knowledge, of the kinetics of deformation-induced amorphization. One sequence that lends itself to analysis is the one depicted in Fig. 52 and that is characteristic of low-stacking fault FCC alloys, such as stainless steel or HEAs. The situation depicted in Fig. 52 is amenable to quantitatively predict the fraction amorphized as a function of externally applied strain and temperature. In low stacking-fault energy alloys and compounds, plastic deformation is often not homogeneous and

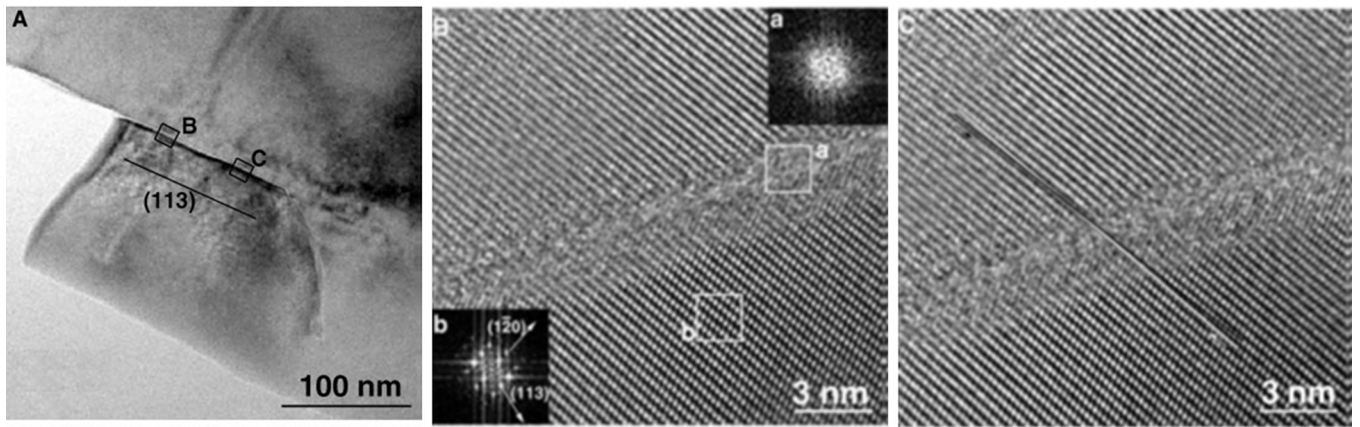


Fig. 36. TEM images of B_4C fragment produced by ballistic test at 907 m/s (23.3 GPa). (a) Bright-field image shows a planar defect from a corner of the fracture surface. (b) HRTEM image of the amorphous band and surrounding region in (a). The lattice corresponds to $[101]$ direction of crystalline B_4C . The loss of lattice fringes in the band indicates localized amorphization. FFT inset patterns also confirms the presence of an amorphous phase. (c) HRTEM image of the boxed area C in (a). The width and appearance of the amorphous zone are the same as in (b). Arrows represent slight lines of lattices across the band. Misalignment of the lattice fringes on two sides of the amorphous band was 1° , ruling out rebonding of two cracked surfaces. Absence of observed melting indicates this amorphization was a solid-state transition caused by development of a shear instability and elastic collapse of the lattice due to the high pressure and impact rates of the ballistic test [86].

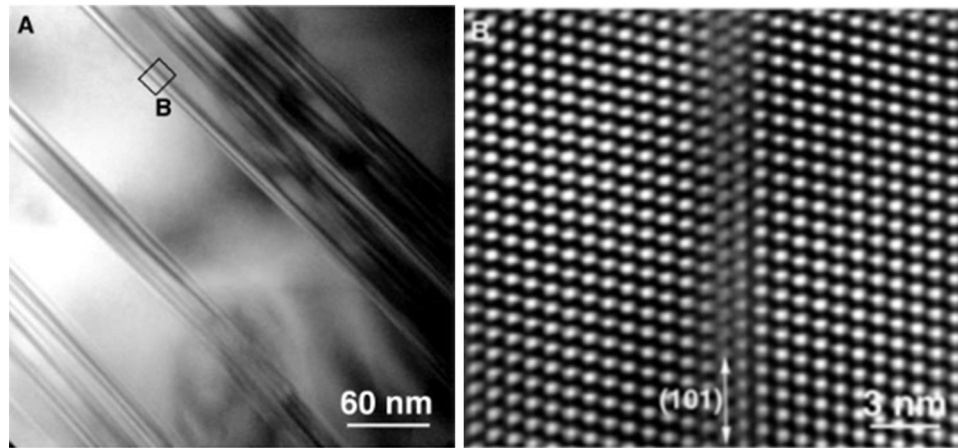


Fig. 37. Boron carbide fragments produced by ballistic impact at 793 m/s (20.3 GPa). (a) Bright-field TEM image showing planar defects. (b) HRTEM image of the area marked in (a) shows that these planar defects are microtwins and stacking faults. As the impact velocity was subcritical, no amorphous bands were formed [86].

generates profuse deformation bands composed of stacking faults, twins, and martensite. Our model presented here, based on the Olson-Cohen model [113] for the kinetics of strain-induced martensitic nucleation, assumes that the hierarchy of deformation leads from the γ phase to ε martensite and then to amorphization since ε martensite has a higher free energy than the original γ phase. The derivation was originally presented in the Supplementary Information section of [57]. Both ε -martensite and twins are generated by the coordinated motion of partial dislocations, shown in Fig. 52 (a) and (b), respectively. The principal difference is that twinning is generated by the movement of partial dislocations on consecutive close packed $\{111\}$ planes, producing a shear strain of 0.707, whereas the γ to ε transformation involves the movement of partial dislocations on alternate $\{111\}$ planes, with an associated shear strain of 0.354. In this model, we assume that the fraction of material in the deformation bands, f_{db} , increases with strain γ as:

$$\frac{df_{db}}{(1-f_{db})} = \alpha d\gamma. \quad (7)$$

where α is a constant that relates the increase in the fraction of material, df_{db} , occupied by deformation bands to the increase by the imparted plastic strain, $d\gamma$. The fraction of undeformed material decreases with

plastic strain. It is represented by term $(1-f_{db})$ in the denominator. Integration of Eq. (7) gives rise to:

$$f_{db} = 1 - \exp(-\alpha\gamma), \quad (8)$$

This accounts for the gradual exhaustion of material in which deformation bands can develop. The number of deformation bands per unit volume, N_{db} , is related to the fraction transformed through:

$$N_{db} = \frac{f_{db}}{V_{db}}. \quad (9)$$

V_{db} is the volume of a deformation band, which is equal to its thickness t_{db} multiplied by the area A_{db} .

Each deformation band is comprised of ε martensite, twins, and partial dislocations; the first two contribute with their characteristic shear strains: $\gamma_\varepsilon = 0.354$ and $\gamma_t = 0.707$. The third strain, f_{pd} , is variable and dependent on the number of partial dislocations. Hence:

$$\gamma_{db} = f_\varepsilon\gamma_\varepsilon + f_t\gamma_t + f_{pd}\gamma_{pd}, \quad (10)$$

where f_ε , f_t , and f_{pd} are the fractions of ε , twins, and partial dislocations in the deformation bands and $f_\varepsilon + f_t + f_{pd} = 1$. The fractions of these deformation mechanisms are dependent on strain, strain rate, and temperature. They determine the total shear strain in a deformation

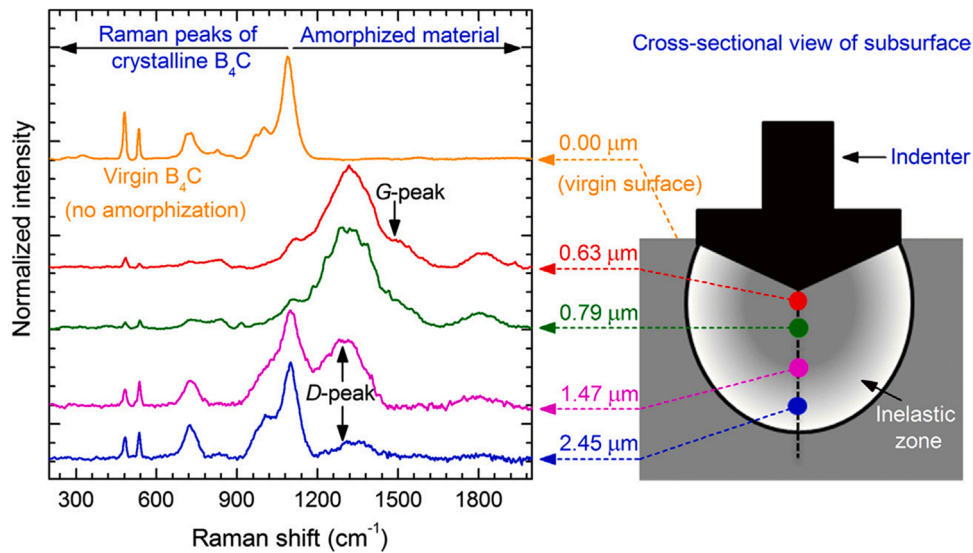


Fig. 38. Raman spectra from the original surface and subsurface regions at different depths after Vickers indentation in B₄C of a 0.98 N load. The intensity of amorphization is the maximum directly beneath the indenter and decreases deeper into the sample [87].

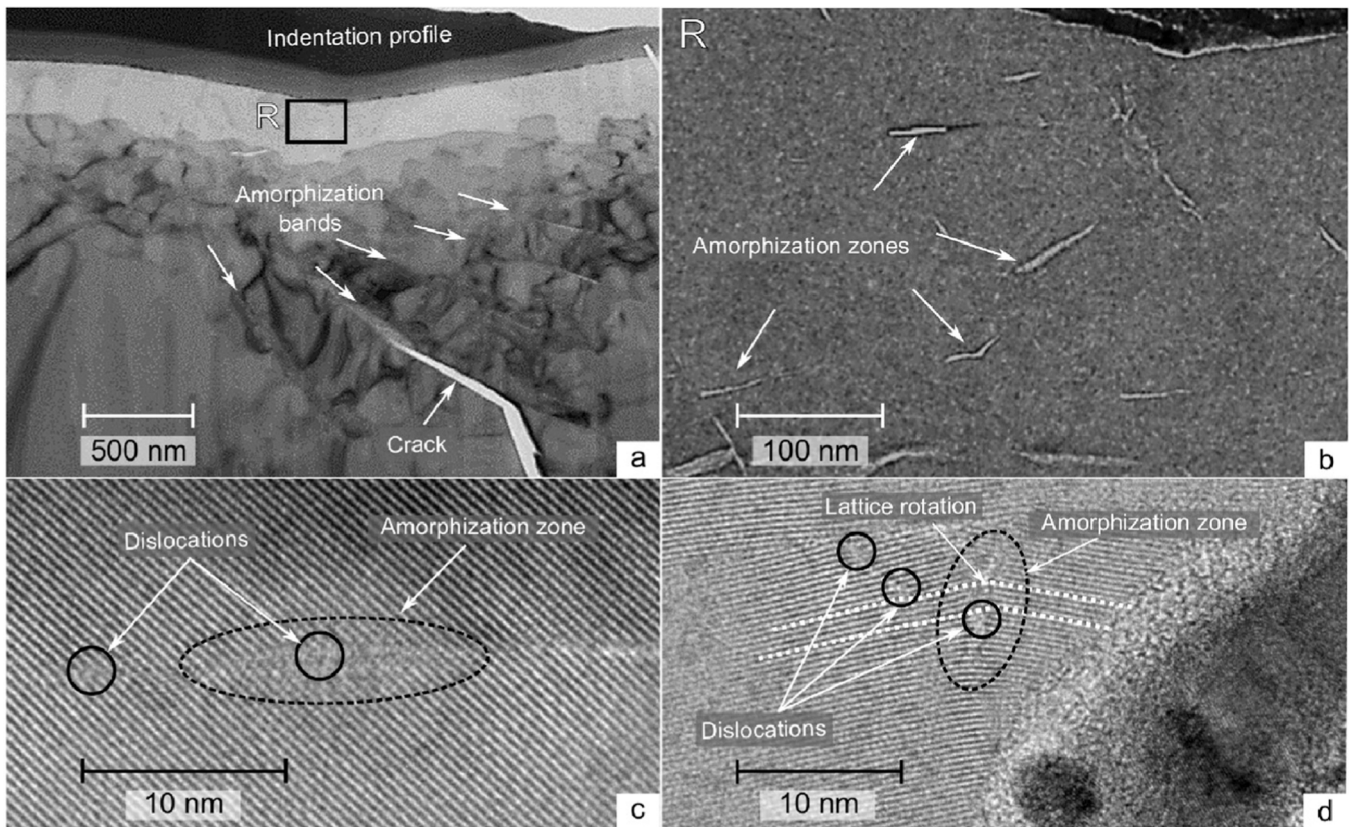


Fig. 39. TEM of amorphous zones generated by indentation in B₄C. (a) Thin and micrometer-length amorphous bands and a crack beneath the indented surface. (b) Magnified region (R) showing several nanometer-sized amorphization zones. (c) and (d) Higher magnifications at the amorphous zones in (b). Dislocations and lattice rotation in the vicinity of amorphous zones. Solid circles indicate lattice dislocations [88].

band and therefore the parameter α in Eq. (8).

A simplified picture is presented in Fig. 52 (c) in which only one fully formed ϵ martensite packet is shown. The intersection of ϵ martensite packets (Fig. 52 (d)) generates additional strain. As mentioned above, each packet has a thickness t_{db} (shown in Fig. 52 (d)). We assume that the volume of the amorphous region is determined by the thickness of the intersecting ϵ martensite packets which, on its turn, is equal to $f_{\epsilon}t_{db}$.

The amorphized region is shown in Fig. 52 (e). Assuming the amorphization occurred at the intersection of the deformation bands which is power law proportional to the number density of the band itself, one can eventually arrive at a sigmoidal relationship of the amorphous volume fraction as a function of strain,

$$f_a = K[1 - \exp(-\alpha\gamma)]^n \quad (11)$$

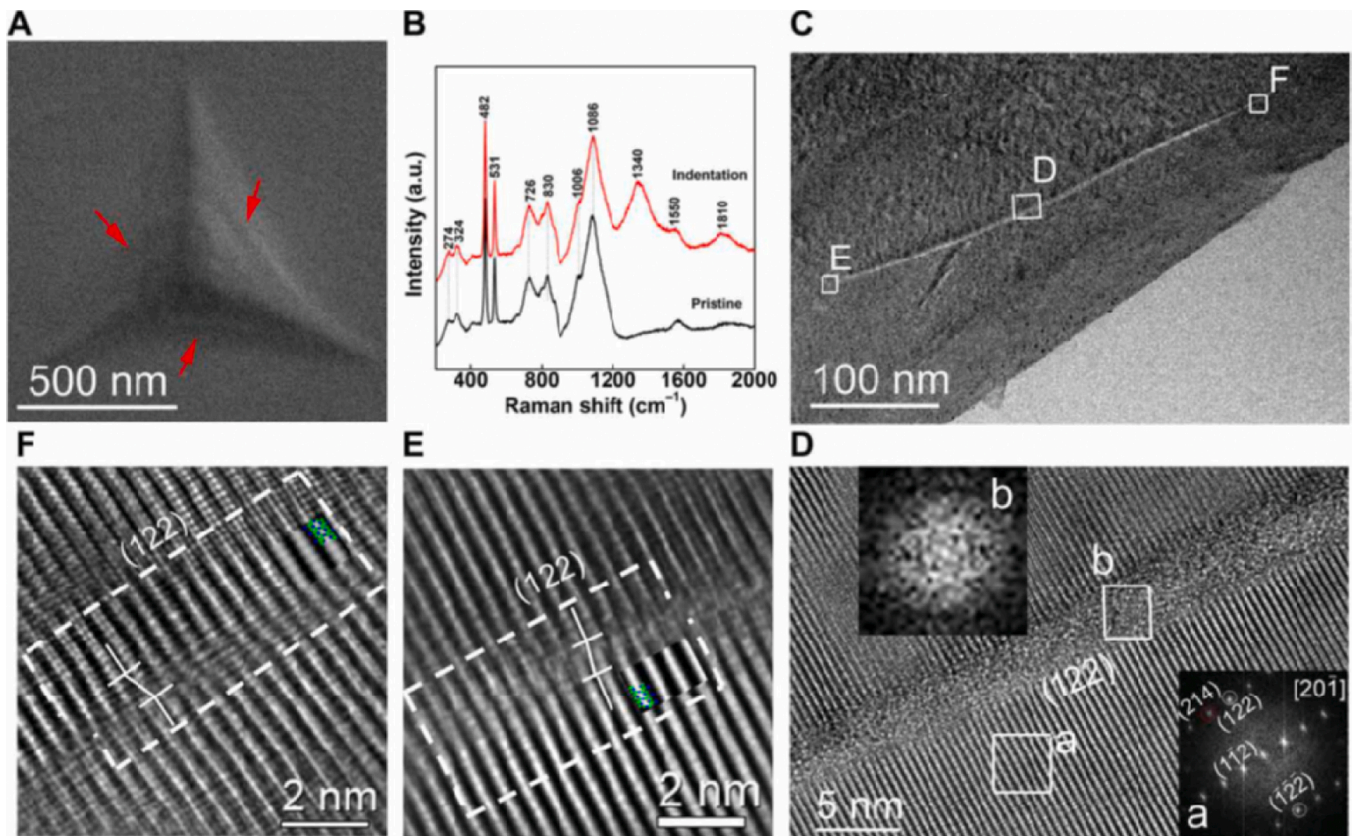


Fig. 40. Characterization of (214) single crystal B_4C after nanoindentation. (a) Scanning electron microscopy (SEM) image of nanoindentation after 25 mN load. No cracks observed. (b) Raman spectra of initial sample (black curve) and indented (red curve) of samples. Extra peaks at 1340, 1550, and 1810 were found in the indented sample, corresponding to the characteristic Raman modes for amorphous B_4C . (c) TEM image the cross section of indented region showing a shear band with ~ 300 nm length and $\sim 1-4$ nm width. (d) HRTEM of boxed area D shows the lack of crystal lattice within the shear band along the (122) plane. FFT (inset b) within band showed the amorphous diffuse halo ring, compared to the FFT (inset a) of the crystalline material on either side of the $[20\bar{1}]$ zone axis. (e) HRTEM image shows the shear displacement at the origin and the tip of the amorphous shear band. (f) HRTEM image of the terminal end of the amorphous band showing the shear displacement. The shear displacements in both (e) and (f) can be characterized by a pair of dislocation dipoles [89].

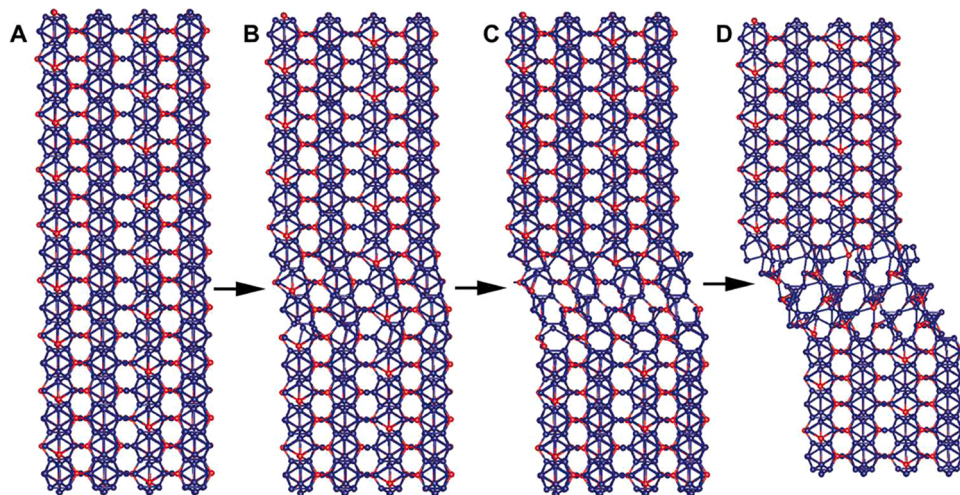


Fig. 41. Diagrammatic representation of dislocation-mediated amorphization in B_4C . (a) Perfect lattice before deformation. (b) Shear deformation distorted the perfect crystal. (c) Dislocation kink formed by shearing. (d) Amorphization developed from dislocation under shear deformation [89].

The proportionality constant K incorporates various material (stacking-fault energy, fraction of ϵ martensite in the deformation packets, probability of nucleation of amorphous region at band intersections, thickness of the deformation bands, and others) and external (strain rate and temperature) parameters presented in [57]. Eq. (11) can

serve as a framework for a theory on the kinetics of deformation-induced amorphization. The determination of the various parameters requires systematic experimentation, which has not been conducted yet. Other materials will exhibit different deformation sequences which are also amenable to analysis.

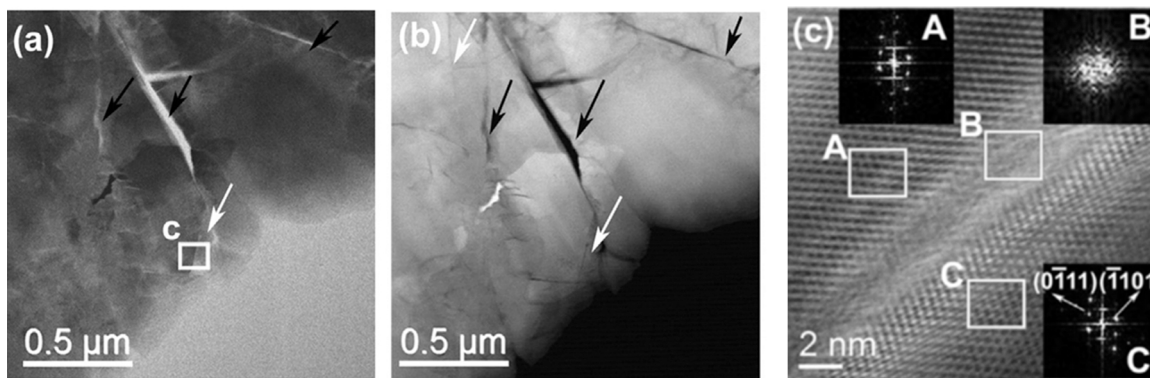


Fig. 42. STEM images of boron suboxide (B_6O) subjected to nanoindentation. (a) Bright-field and (b) Dark-field micrographs show cracks (black arrowhead) and shear bands (white arrowhead) under the indented region. (c) Magnified BF-STEM image of the amorphous band along the $(0 \bar{1} 1 1)$ direction (inset FFT pattern A). The loss of lattice fringes indicates the amorphization (inset FFT pattern B) [90].

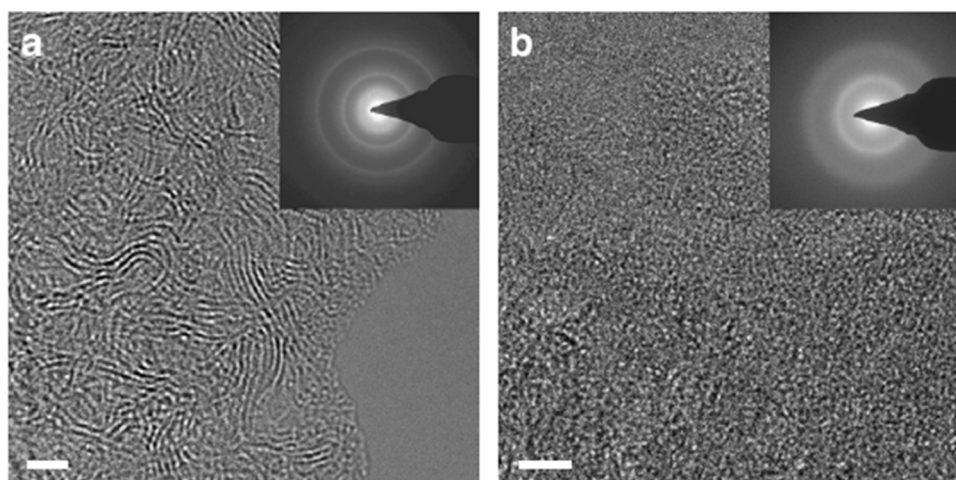


Fig. 43. TEM images of amorphous diamond produced by high pressure and in situ laser heating from glassy carbon. (a) HRTEM and selected area electron diffraction (SAED) patterns of glassy carbon (b) HRTEM and SAED images of the recovered amorphous diamond confirm its disordered amorphous nature. The scale bars in (a) and (b) are 2 nm [91].

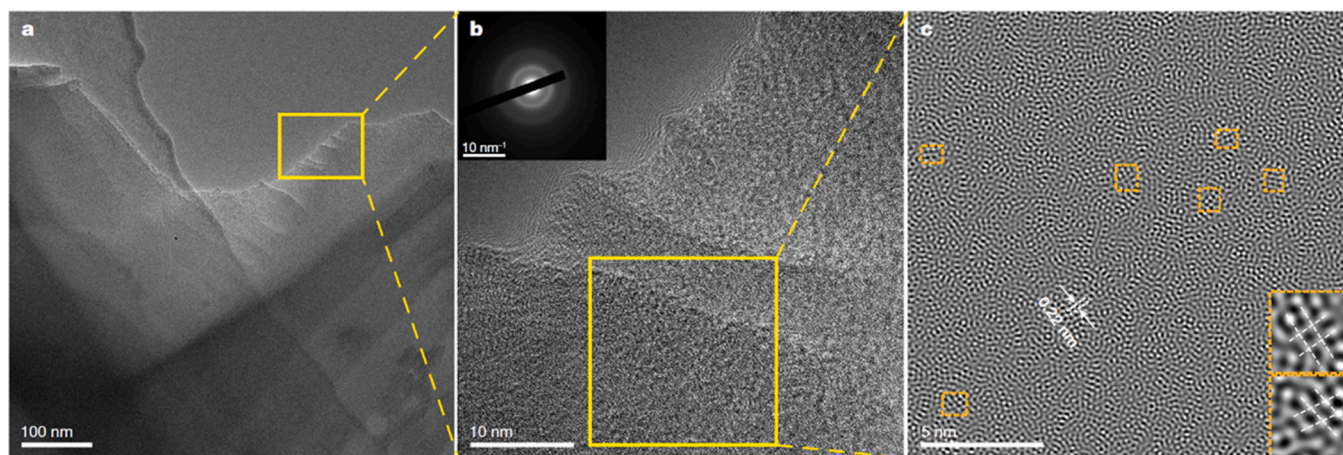


Fig. 44. TEM images of the amorphous diamond sample. (a) At low magnification. (b) HRTEM image of the yellow boxed region in (a). Inset is the corresponding SAED pattern. (c) Inverse FFT image of the yellow boxed area in (b). Orange boxed regions exhibit randomly oriented MRO clusters of interplanar spacing of $\sim 2.2 \text{ \AA}$ similar to that of diamond. Insets show diamond-like intersecting angles between the 'crystal-plane-like' stripes [92].

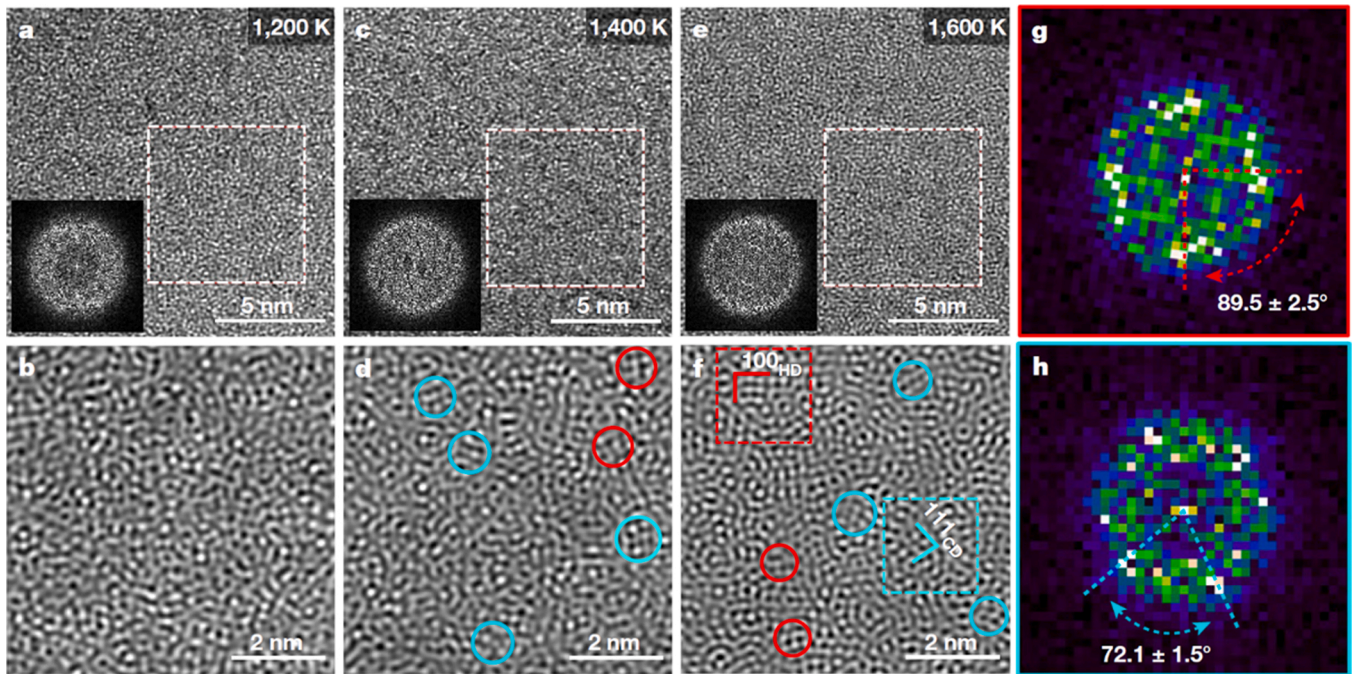


Fig. 45. HRTEM micrographs of diamond samples recovered from 30 GPa and 1200–1600 K. (a)–(f), HRTEM images and corresponding inverse FFT images. Insets are FFT patterns of the white boxes ($7.0 \times 7.0 \text{ nm}^2$) in (a), (c) and (e). The cyan and red circles in (d) and (f) exhibit some of the MRO clusters. In (f), the lattice fringes marked by the cyan and red solid lines match (111) and (100) crystal planes of cubic and hexagonal diamond. (g) and (h) are FFT patterns of the red and cyan boxes ($2.0 \times 2.0 \text{ nm}^2$) in (f). The brighter spots on these diffuse haloes marked by the arrows confirm cubic and hexagonal diamond like MRO clusters in (f) [93].

8. Fundamental mechanisms of deformation in amorphous materials

This section presents the principal mechanisms of plastic deformation which can lead to amorphization. Many amorphous materials have superior mechanical performance under specified circumstances. Previous attempts to reconcile dislocation theory with plastic deformation of glasses have failed, so new mechanisms had to be postulated. These theories fall into two groups: free volume (initially proposed by Spaepen [114]) and shear transformation zones (initiated by Argon [115]). These theories are being corroborated by molecular dynamics simulations and advanced characterization techniques. Generally, as the deformation energy from a defect density increases, elastic deformation yields to dislocation multiplication and movement, then to twinning, subsequently to phase transformations and finally, under the extreme conditions of high stress, high strain, and high strain rate, solid state amorphization can take place (Fig. 53) [116].

8.1. Free volume theory

Free volume is defined as the empty space in a solid or liquid that is not occupied by molecules. When the temperature changes, the free volume also changes. In amorphous materials, free volume can be considered as the carrier for plastic deformation, in an equivalent role to dislocations in crystalline materials.

In free volume regions, inelastic relaxation through local atom rearrangements is possible due to the weak mechanical coupling to the surrounding atomic structure. These sites are called soft spots where amorphous structure destabilization preferentially initiates as a result of passing through the glass transition temperature or local shearing from applied stresses.

When shear stress is applied to crystalline materials, the initial volume during plastic deformation is unchanged because the periodicity of the crystal structure along slip planes leaves identical atomic positions and vicinities for the slipped material. In contrast, in amorphous materials the free volume increases during plastic deformation and some

voids are left behind due to the randomness of their structure (Fig. 54) [117]. The nano-voids are more likely to nucleate in tension rather than in compression, indicating that the hydrostatic pressure plays an important role in the nucleation of nano-voids.

Dislocations and shear bands are generated by different micro mechanisms in crystalline materials and amorphous metals by mechanical deformation, respectively (Fig. 55) [117]. Shear banding in glassy materials plays a key role similar to dislocations in crystalline materials in mediating plasticity and failure.

Plastic flow in amorphous metals is initiated at some locally perturbed zones. The flow localizes as a result of strain softening from accumulated defects observed at the atomic scale (Fig. 56) [117–119]. Amorphous metals tend to fracture abruptly along these shear band planes, especially when subjected to tensile loading. This mode of material failure has impeded many structural applications.

Spaepen [114] proposed a single atom model (Fig. 57 (a)) [117] for the formation of free volume in amorphous materials in 1977, characterizing it as the elastic energy required to push an atom into a small empty space. Macroscopic plastic flow is considered to be the sum of these individual atomic jumps. The atoms tend to jump to the stress direction when an external stress is applied, forming the plastic flow in amorphous metals.

8.2. Shear transformation zone theory

The Shear Transformation Zone theory (STZ) was proposed by Argon in 1979 (Fig. 57 (b)) [115,117] based on an atomic-analog bubble-raft model, explaining the shear deformation as spontaneous and cooperative rearrangements of small clusters of randomly close-packed atoms in amorphous solids. These clusters, up to around 100 atoms, are subjected to inelastic shear deformation from a lower energy configuration to a higher energy and volume configuration, resulting in stress and strain reconfiguration in the STZ region. Local motion of STZs around the free volume sites push apart surrounding atoms, leading to dilatation and strain softening in the vicinity.

A number of simulation studies have recognized that single plastic

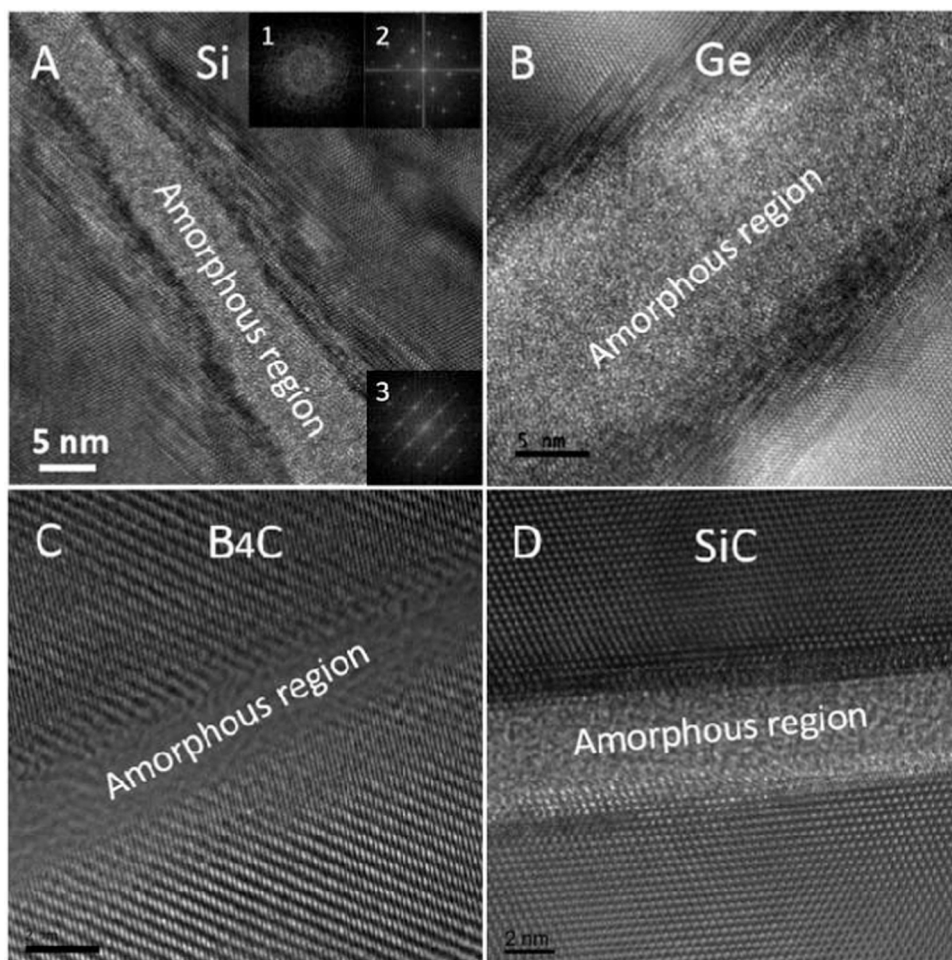


Fig. 46. HRTEM images of amorphous bands in four covalently bonded solids: (a) Si, (b) Ge, (c) B₄C, and (d) SiC. High density of stacking faults was found at the interface between crystalline and amorphous phases in Si and Ge while not at the interface in B₄C and SiC [94].

events in amorphous metals can be illustrated by local stress fields with quadrupolar symmetry, analogous to Eshelby's inclusions within an elastic continuum (Fig. 58) [120]. Because of the mismatch between the sheared zones and the surrounding matrix, extra volume must be created when amorphous metals are sheared. These zones are softer, allowing the material to flow, and these nonaffine displacements cause particles within the shear plane to leave the glassy cage outward along a particular line from both ends, while pushing the particles perpendicular to the line inwards towards the center of the glassy cage from both directions, causing local density to change. As a result of an alignment of Eshelby-like quadrupoles, shear banding develops.

Fig. 59 [120] shows some high and low density regions within amorphous shear bands propagating along the direction of these shear bands in some metallic glasses. The periodicities vary between 135 and 163 nm. This alternating density due to the alignment of Eshelby plastic events is considered as a response to plastic shear deformation in metallic glasses and may be postulated for other amorphous materials.

Crystalline materials generally deform through the generation and propagation of lattice defects. However, nanoscale amorphization, which is defined as the formation of nanoscale amorphous regions in crystalline solids, is suggested as an alternative deformation mechanism under extreme loading conditions. It is shown that nanoscale amorphization can facilitate the movement of plastic flow in crystalline nickel and silicon nanowires (Fig. 60) [121].

Fig. 61 [122] compares the differences of microstructural defects between bulk metallic glasses and polycrystalline metals. While dislocations carry the plasticity in crystalline materials, bulk metallic glasses

deform via the activation of shear transformation zones (STZs). A STZ's activation energy depends on its local composition and can be tuned by microalloying to modify its mechanical properties. Solutes in crystalline materials normally pin and impede dislocation motion. Precipitates and secondary phases can cause precipitation hardening in polycrystalline metals. In amorphous metals, the heterogeneous microstructure helps to stabilize the glass to avoid catastrophic failure. The interfaces separating glassy grains within nanoglasses prepared by cold compaction of glassy nanoparticles are found stable if local strain does not exceed the flow strain of the bulk metallic glass. These interfaces are characterized by an excess free volume and lack of short-range order. Some experimental studies on iron-scandium nanoglass exhibited improved ductility in nanoindentation compression, and MD simulation of Cu-Zr nanoglasses showed that interfaces served as precursors for shear-band formation, restraining strain localization and contributing to more homogeneous deformation.

9. Molecular dynamics simulations

In the past few decades Molecular Dynamics (MD) simulations have evolved as an effective tool to study the motions of atoms and molecules in a wide range of materials and environments. Molecular Dynamics involves the use of computer simulations to study the movements of the particles in a system. In general, the forces between particles in the system are calculated purely from the positions of the particles themselves, which are used to calculate how those particles move without any other prior conditions. This type of simulation from the ground up has

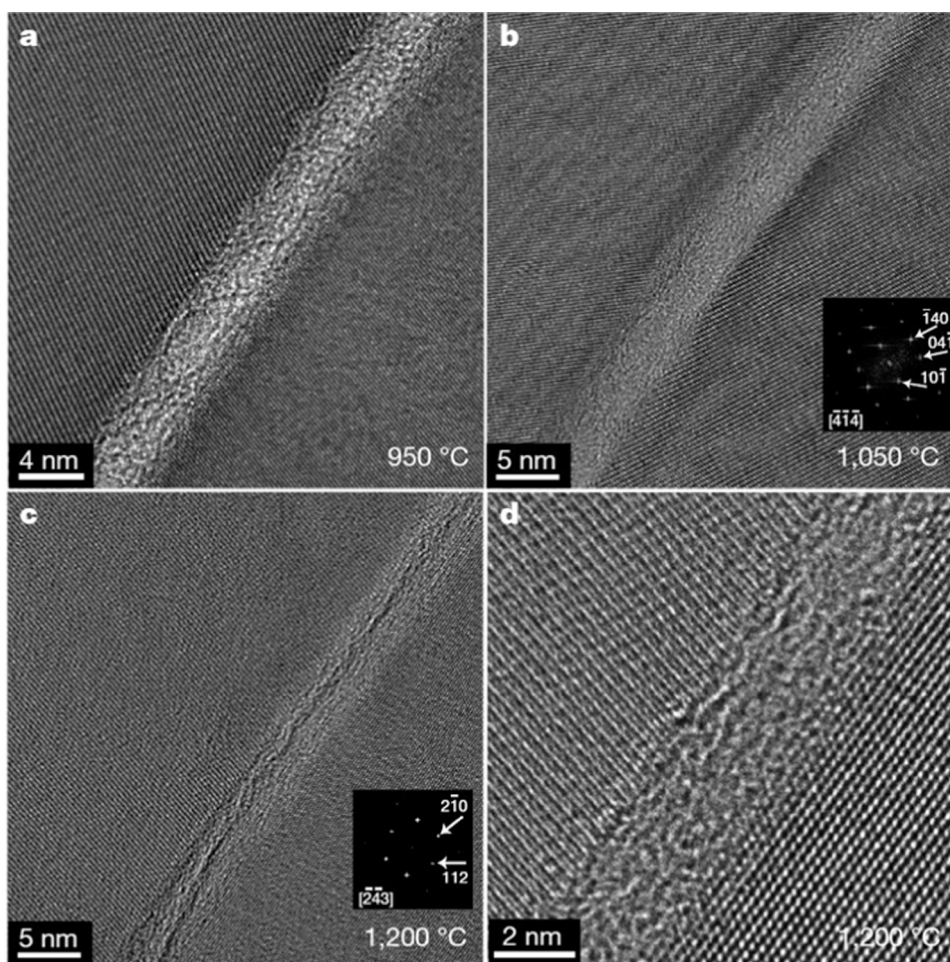


Fig. 47. HRTEM images of two different grain boundaries in forsterite specimens by static compression in a Paterson press at 0.3 GPa at (a) 950 °C, (b) 1050 °C, (c) and (d) 1200 °C. At 950 and 1050 °C boundaries show presence of intergranular amorphous layer. At 1200 °C amorphous layers were still present but much less frequent, about ten times less. FFT insets of (b) and (c) confirm the crystal structure of forsterite [98].

successfully recreated many of the properties of materials and helps to understand exactly why materials behave as they do. As computational power increases, the capabilities of these simulations to capture larger and more complex systems has expanded as well. Studies have been performed that focus on analyzing amorphization and how its mechanisms work at an atomic scale. By analyzing the motion of the atoms within the material before and during the onset of amorphization, the exact mechanisms leading to amorphization can be examined. Other studies may focus more on how plastically deformed amorphization differs between materials depending on factors such as shape or morphology. The types of deformation most studied for deformation-induced amorphization mimic those used in real world experiments, such as crack-tip tensile tests, hydrostatic compression, diamond anvil cells, nanoindentation, nanowires, shear strain rate, and shock experiments.

One of the limiting factors in the accuracy of molecular dynamics studies is the potential used to describe the relationships between atoms. The forces between particles are calculated directly from these potentials, meaning that their accuracy is directly tied to the development of the system. These interatomic potentials are constantly being developed and improved to better describe pure elements and to expand the capabilities to more complex alloys, compounds, and complex structures. There are classical empirical potentials which use parameters fitted to material properties, as well as ab initio potentials which calculate material properties from their electronic structure. For studying metallic materials, the classical EAM (Embedded Atom Method) potential is

widely used as it describes the bonding behavior of metals well. For ionic or more complex materials, it may be necessary to use ab initio potentials as it is more difficult to model them with classical potentials. For many materials multiple empirical potentials exist, which may all produce different results under the same simulations. An example is silicon: the Stillinger-Webber, Tersoff, and Modified Embedded Atom Method (MEAM) potentials are useful, and each one has advantages over the other ones for specific aspects. Benchmarking of potential performance is an important part of selecting the one which best fits the conditions of the experiment and best reproduces the experimental results.

Early work started when computational power was more limited and the theory was not as developed, involving studying supercells composed of small numbers of atoms and studying the crystalline formations between them. A series of studies on α -Quartz amorphization found that the structure would change to an amorphous phase upon reaching 20–35 GPa pressures, in agreement with the experimentally found amorphization of quartz around 30 GP [123–125]. In the simulations, increasing the pressure of the system of atoms led to changing coordination numbers between silicon and oxygen atoms. With increasing pressure, the silicon atoms changed from fourfold to sixfold coordination as seen in Fig. 62. Further pressurization leads to mechanical instabilities and eventually the amorphization of the material.

Several phase changes were observed during the process, including the identification of a new structure when using a 27-atom supercell to observe the crystalline phase changes. Binggeli et al. [123] found that a new crystalline phase was formed prior to amorphization after

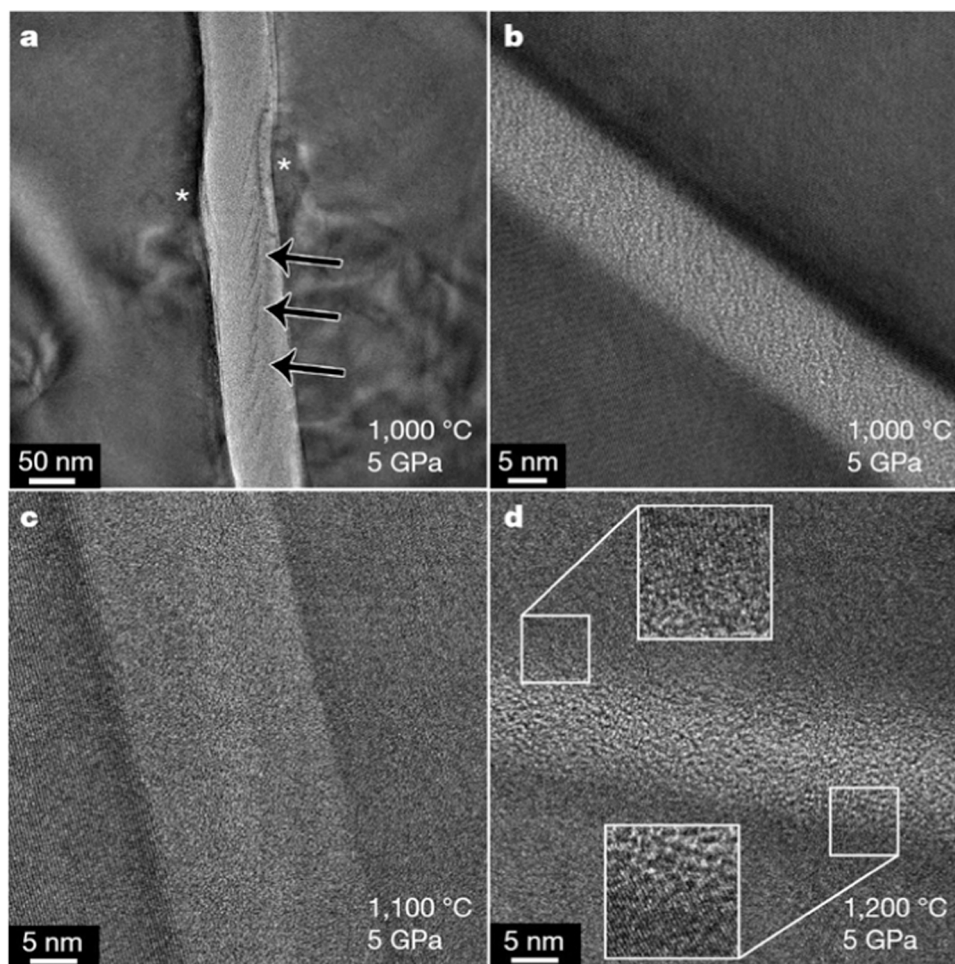


Fig. 48. HRTEM images of forsterite specimens by static compression in the multi-anvil press. (a) 5 GPa, 1000 °C. (b) 5 GPa, 1000 °C. (c) 5 GPa, 1100 °C. (d) 5 GPa, 1200 °C. (a) The asterisks indicate the displacement of the amorphous lamella; the black arrows denote shear bands. Insets in (d) show magnified views of the glassy film and lattice interface [98].

compression to 33 GPa and an annealing process. The original SiO_4 tetrahedra were changed into edge sharing SiO_6 octahedra in a denser configuration, as seen in Fig. 63 [125]. Further studies in related materials such as berlinite and coesite found similar mechanisms of amorphization [126].

9.1. Applied pressure – tensile and compression

Amorphization has been found in crack-tip studies performed on fcc Cantor alloys and supported by molecular dynamics studies of the same material [127]. Fig. 64 shows the MD results of the simulated crack-tip response to applied tensile stress and the transformation from the crystalline to amorphous phase. The structure at the crack tip sequentially evolves from crystalline to lamellar, then spotted, then amorphous patterns. The transformation begins near the crack tip as dislocation tangles gather, and is possibly due to the high lattice friction and grain boundary resistance to dislocation glide in these high entropy alloy fine grained microstructures. Once the amorphous phase has formed in the area, it can additionally help inhibit crack propagation by forming amorphous nanobridges in the crack's wake. This provides an extrinsic toughening mechanism for the material, complementing conventional mechanisms such as energy dissipation through plasticity and phase changes ahead of the crack tip.

Hydrostatic compression tests performed on $\text{Ge}_2\text{Sb}_2\text{Te}_5$ (GST), a common material used for memory storage, have also shown the creation of amorphous material at pressures above 18 GPa [128]. A

molecular dynamics simulation found that the initial structure transformed first to an amorphous state with a cubic framework and coordination number of 6, increasing to a trigonal framework with a coordination of 8 as pressure increased (Fig. 65). As the pressure was increased, bond lengths shortened resulting in their strengthening, but also resulted in structural instability due to coulombic repulsion. When the structure was released to ambient pressure, the remaining amorphous cubic phases returned to their initial cubic phase, but the transformed trigonal amorphous phase transitioned to another amorphous phase similar to that of melt-quenched GST (Fig. 66) with high coordination and low bond strength.

9.2. Nanoindentation

Nanoindentation is one of the most studied areas of amorphization using molecular dynamics. The size of MD simulations and the scale of nanoindentation experiments are well matched. In nanoindentation, a tip with a known size is pressed into a small volume of the material, generating real time measurements from load-displacement curves. Atomistic simulation is useful because it can capture microscopic deformations and phase changes as they occur during the process. Many materials have been studied both experimentally and with simulations, including silicon, silicon carbide, silicon nitride, aluminum nitride, and others [110,129–134]. A common feature seen in these studies is the pile-up of dislocations directly underneath the indenter tip. At low indentation values, before the onset of plasticity, there is reversible

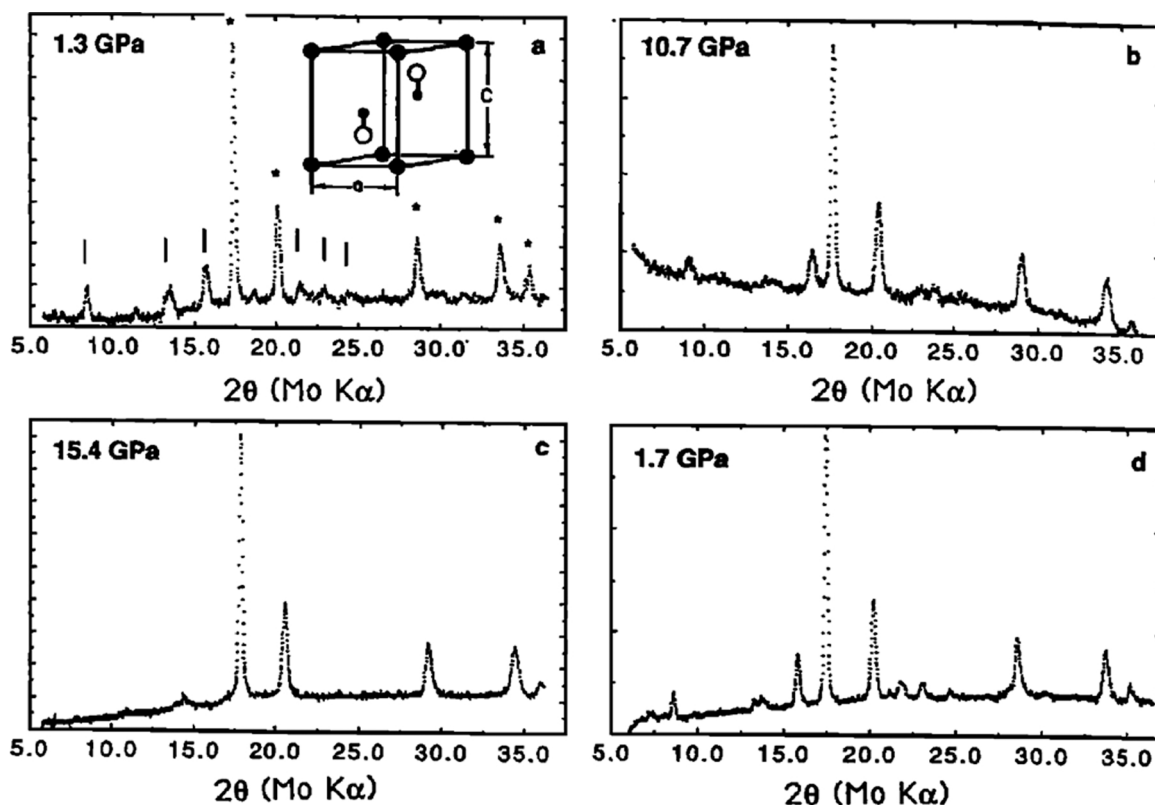


Fig. 49. Powder X ray diffraction of $\text{Ca}(\text{OH})_2$ and Au in the diamond cell on increasing pressure. (a) The lines corresponding to $\text{Ca}(\text{OH})_2$ and Au. The inset is a (110) projection of the $\text{Ca}(\text{OH})_2$ unit cell. (c) At 15.4 GPa, $\text{Ca}(\text{OH})_2$ has amorphized according to the broad feature at 14° . (d) Upon release, $\text{Ca}(\text{OH})_2$ recrystallizes between 3.6 and 5.1 GPa [99].

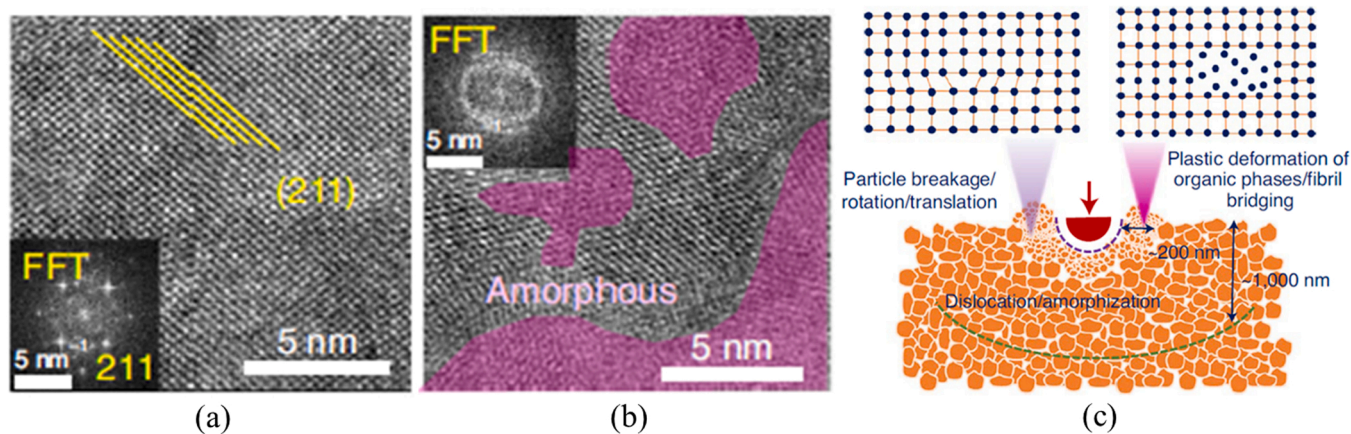


Fig. 50. Dactyl club samples after impact tests. (a) Perfect (211) plane in crystalline matrix. (b) Impact-induced amorphization. (c) Different toughening mechanisms of surface nanoparticles from high-strain-rate impact [101].

amorphization. Beyond a critical loading point, further amorphization occurs along with the onset of dislocations. These amorphous regions and dislocations spread from the indented surface.

A particular benefit of molecular dynamics simulations is the ability to see snapshots of the system as defects and phase changes occur. The top of Fig. 67 [129] shows the initial configuration of a nanoindentation experiment on 3 C-SiC. The bottom of Fig. 67 shows the evolution of the amorphous phases and emergence of dislocation loops as the indentation increases.

In Fig. 68 [133], we see a load indentation curve in single crystalline silicon. Three distinct zones can be seen: zone 1 is elastic and zone 2 is plastic. A distinct discontinuity can be seen starting in zone 3, a so-called

“pop-in” event, indicating a change in deformation mechanism. It was found that amorphous silicon dominated the deformation process at this stage. A combination of large shear stresses and associated hydrostatic pressure created the lattice distortion that led to this amorphization.

Fig. 69 [134] explores how grains and grain sizes affect the development of the amorphous phase in silicon. Amorphization occurred under the nanoindenter tip, at a depth which matched the calculated value using Hertz contact theory for the depth of maximum shear stress based on indenter radius of contact and contact stress. In the single crystal experiment, results were similar to those of other silicon studies. When grain boundaries were introduced, amorphization tended to follow them as they provided the path of weakest connection with

A SHOCK COMPRESSION = HYDROSTATIC COMPRESSION + SHEAR

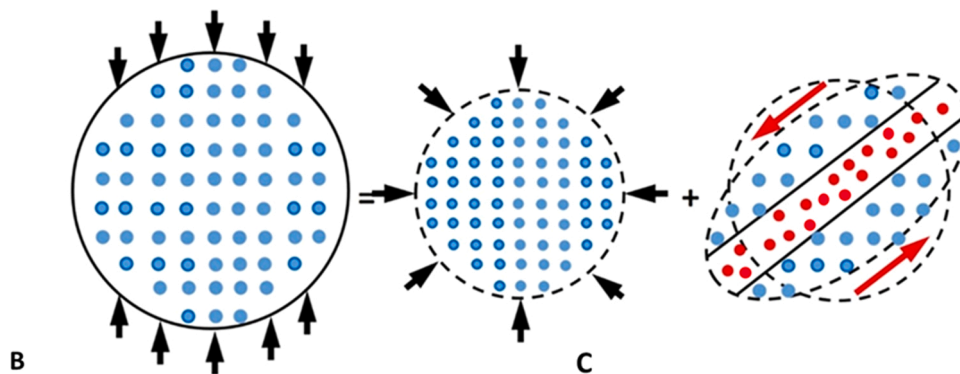


Fig. 51. Shock compression and its hydrostatic and deviatoric (shear) stress components. The regions of maximum shear stress at 45° from the shock direction actually form a cone [95].

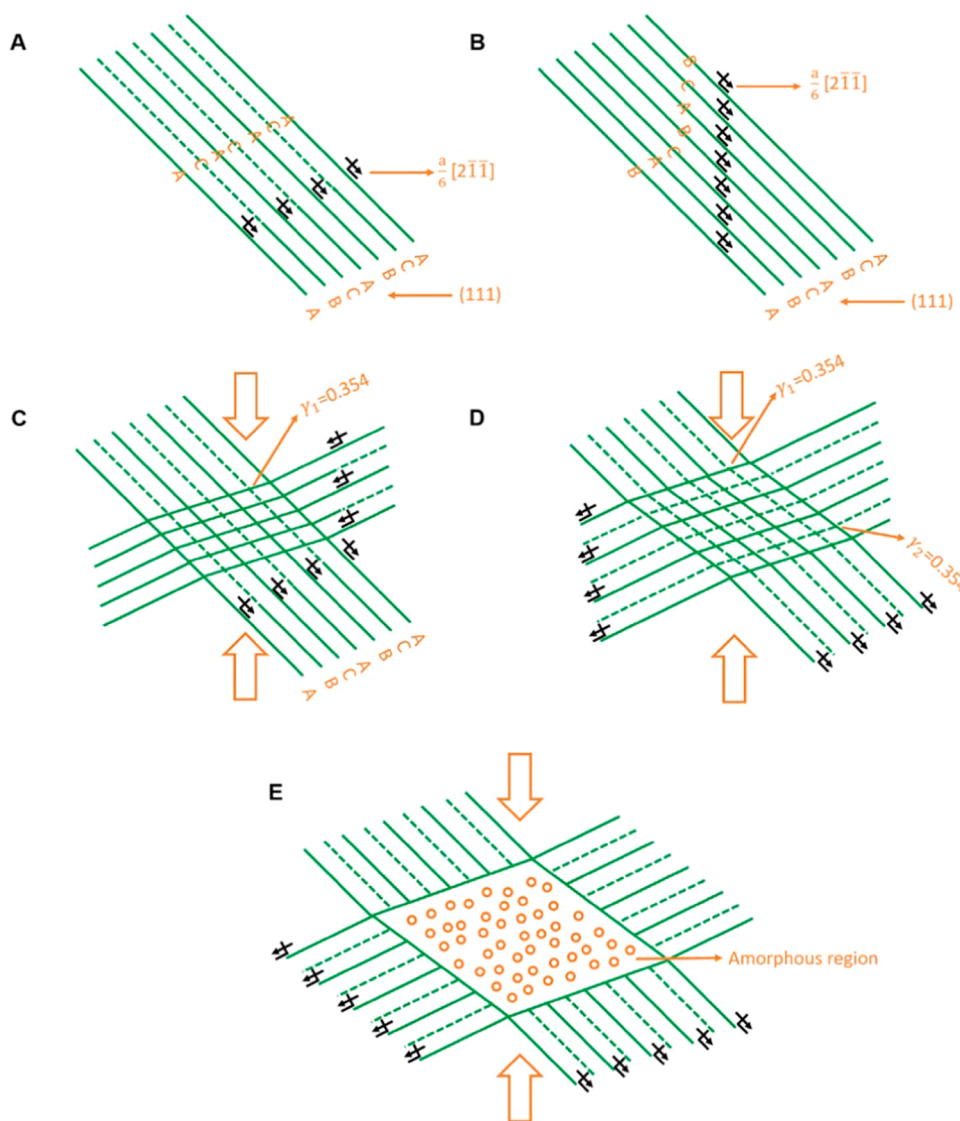


Fig. 52. A general deformation sequence in an alloy or a compound with low stacking-fault energy. (a) Stacking fault packets are generated, (b) form on different planes, (c) intersect, (d) form phase transitions, and (e) eventually amorphized [57].

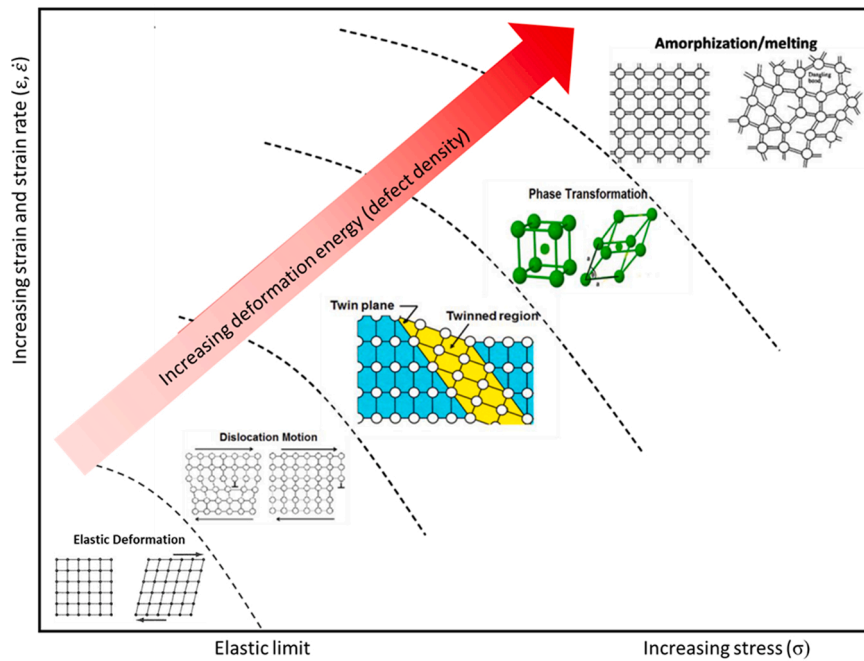


Fig. 53. Evolution of deformation mechanisms as the strain and strain rate increase. The boundaries between domains highly depend on materials' properties [116].

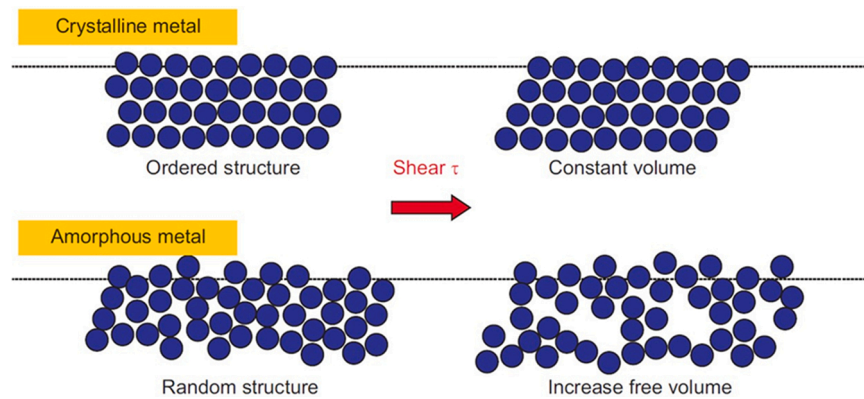


Fig. 54. Spaepen's free volume theory in crystalline vs. amorphous metals [117].

produced complex stress distributions for the amorphous region to propagate through. It was found that horizontal spread of the amorphous region was faster, also due to the maximum shear stress occurring at a specific depth [134].

9.3. High strain rate studies

High strain rate, whether through a gas gun or pulsed laser experiment or simply setting a deformation rate in a molecular dynamics simulation, is another method of producing amorphization through plastic deformation. Molecular dynamics is particularly adept at simulating these experiments as the time scales at which they occur is on the order of picoseconds and nanoseconds (for laser shock experiments), which closely matches the time scale of the simulations. At sufficiently high strain rates, standard methods of material deformation or failure can be kinetically inhibited [135,136]. Fig. 70 [136] shows nickel nanowires deformed above a strain rate of $10^7/s$. They no longer undergo necking and failure, and instead transition to an amorphous state where the entire nanowire deforms nearly uniformly.

Shock experiments also reach extremely high strain rates capable of creating amorphous phases in materials. In experiments on silicon, it

was found that amorphization occurred at strain rates of $10^7/s$, and above a shock pressure of 11 GPa [137,138]. A time evolution of a shock wave passing through silicon can be seen in Fig. 71. As the shock passes through the crystal, shear bands and dislocations are created in its wake. When the shear bands intersect, they can form amorphous regions. This process was described thermodynamically by the changes in Gibbs free energy between the amorphous phase, the shock temperatures reached, and a critical stacking fault density necessary for the amorphous phase to become energetically favorable [137]. Similar studies using laser shock to induce amorphization were conducted in materials such as silicon carbide and germanium, with corresponding molecular dynamics simulations [139,140].

Fig. 72 [122] reveals the processes which lead to shear-band formation. At lower strains, no surface defects could serve as stress concentrators. Fig. 73 [122], at higher strain, shows a STZ that is activated at the surface and leaves behind a kink. At an even higher strain, the kink serves as a stress concentrator and leads to shear localization; the embryonic shear band propagates through the sample and reaches the opposite surface at about 13% strain, when shear band slip occurs.

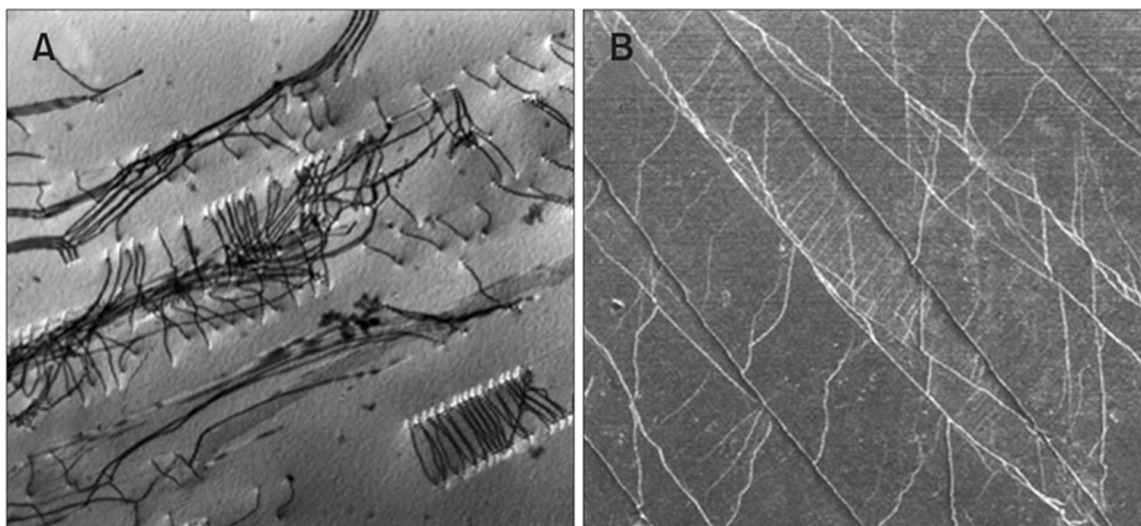


Fig. 55. Micrographs show the dislocations in crystalline material and shear bands in amorphous material. (a) TEM image of deformed 316 stainless steel exhibiting dislocations and dipoles on (111) planes (b) SEM image of deformed bulk metallic glass with many shear bands [117].

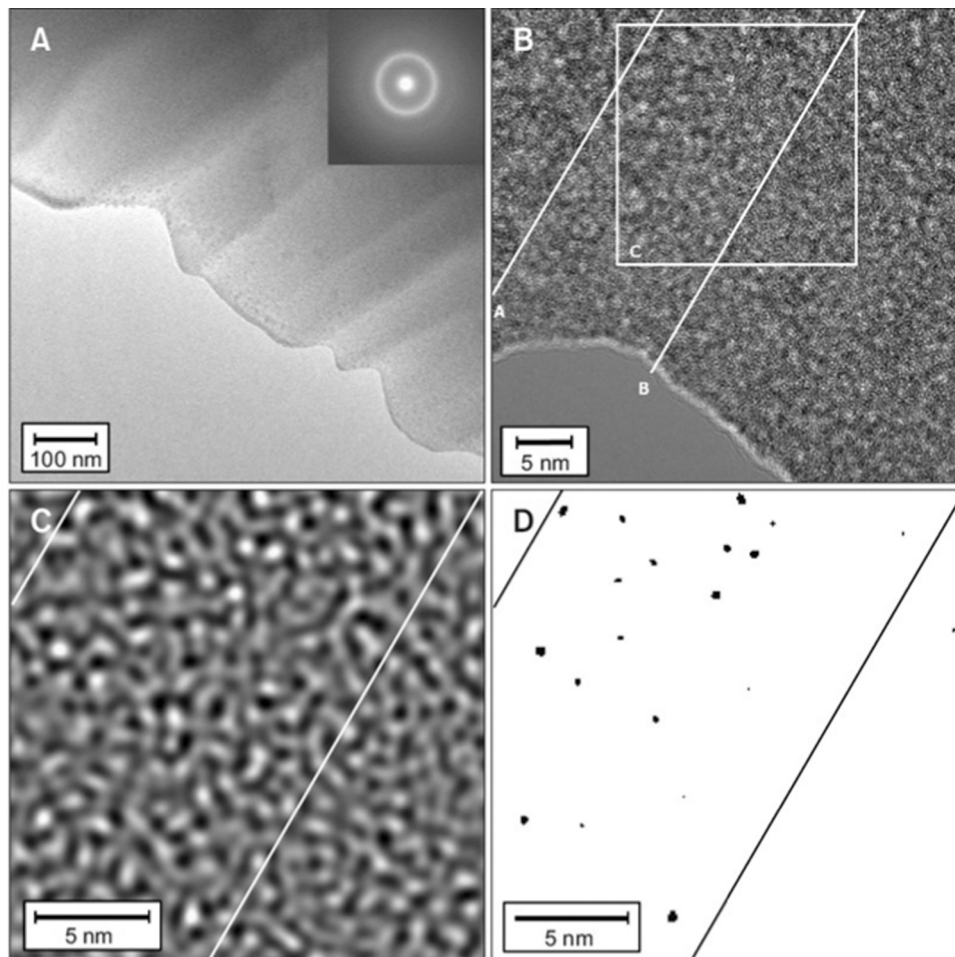


Fig. 56. (a) Low magnification and (b) HRTEM micrographs of the shear band area induced by bending an amorphous metal. (c) FFT pattern. (d) Same image as (c) with black spots corresponding to white areas in (c), indicating regions of excess free volume. The free volume has preferentially accumulated and nanovoids (1 nm or less) are observed within the shear band [117–119].

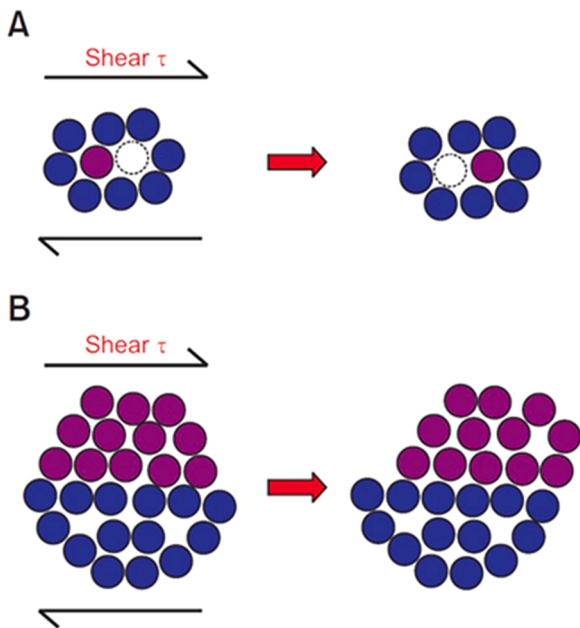


Fig. 57. Two different atomic scale deformation mechanisms proposed for amorphous materials. (a) Spaepen [1977], free volume model, an individual atomic jump (macroscopic diffusion and flow). (b) Argon [1979], a shear transformation zone (spontaneous and cooperative rearrangement of a cluster of atoms) [117].

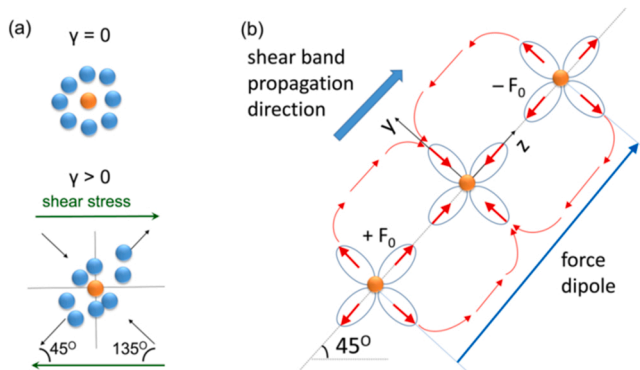


Fig. 58. (a) Shear deformation in metallic glass renders particles within the shear plane to leave the glassy cage outward along the 45° line from both ends, meanwhile pushes the particles perpendicular to the line inwards towards the center of the glassy cage from both directions, thus local density changes. (b) Density change and shear band formation are caused by an alignment of Eshelby-like quadrupoles along the 45° direction [120].

9.4. Shear strain studies

Pure shear has also been observed to form amorphous phases in materials, particularly in cases such as friction or wire drawing. In a friction study on diamond, it was found that friction between diamond layers inevitably caused the formation of an amorphous layer at the topmost surface of the diamond crystal, as seen in Fig. 74 [141]. The coordination of the carbon atoms during the deformation changes largely from 4 to 3, or a change in carbon hybridization from sp^3 to sp^2 . The thickness of the amorphous layer increases with time as the friction force is applied and is also affected by the orientation of the crystal surface.

Another study on copper and niobium interfaces also observed the effects of severe plastic deformation on a shear surface resulting in the formation of amorphous layers. Depending on the orientation

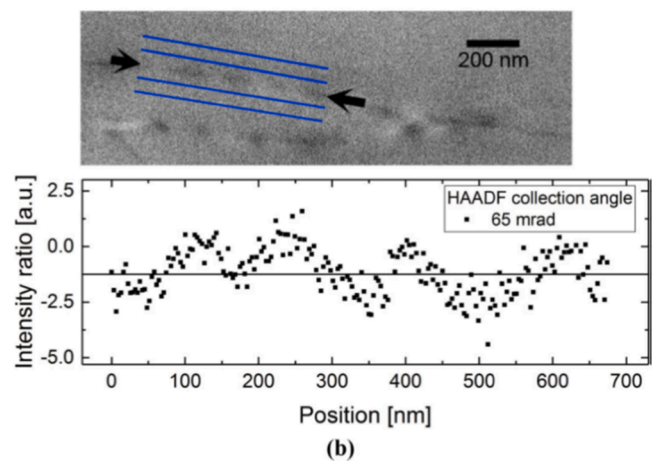
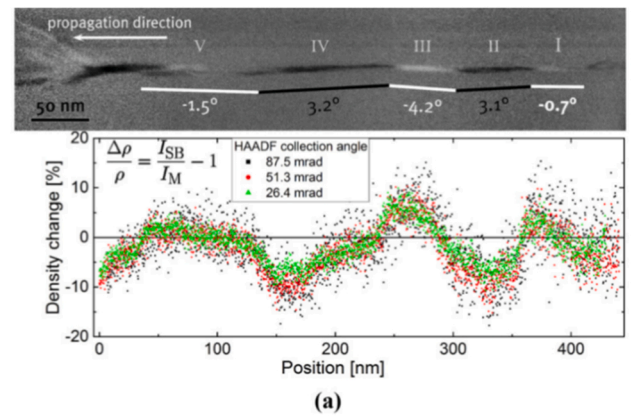


Fig. 59. (a) Top: High-angle annular dark-field (HAADF)-STEM image exhibits brightness contrast reversals in a shear band of $Al_{88}Y_7Fe_5$ metallic glass by cold rolling. Bottom: Corresponding quantified density oscillations along the shear band. (b) Top: HAADF-STEM image exhibits brightness contrast reversals in a shear band of a $Zr_{52.5}Cu_{17.9}Ni_{14.6}Al_{10}Ti_5$ BMG sample by compression. Bottom: Corresponding quantified density oscillations along the shear band [120].

relationship between the interfaces, amorphization occurred at high strains [142]. Some orientations deformed only elastically via pure interface sliding, while in other directions dislocations glided through the layers creating a change in the orientation relationship. Once the amorphous layer had been formed, all subsequent deformation occurred within this layer. The amorphous layer thickness also increased with strain, as seen in Fig. 75 [142], growing with its square root.

10. Conclusions and perspectives

Amorphous metals (metallic glasses) have found some unique functional and structural applications. The first one among them was in the core of high power transformers (Metglas), a development by Allied-Signal. These relied on thin films produced by rapid cooling from the melt (melt spinning). Another application was in razor blades for their properties of high hardness and wear resistance. The development of bulk metallic glasses at Caltech by Prof. Johnson's group [143] enabled thicker sections to be produced. These stimulated the formation of a company, Liquidmetal Technologies, with commercial products such as golf clubs, cell phone covers, and coatings. Their high strength (~ 1.25 GPa) as well as high elasticity (low modulus) enabled these unique applications. These products are cast directly from the melt. Bulk metallic glasses are reviewed by Wang et al. [144].

The other alternative, amorphization by mechanical deformation, has not yet yielded any commercial applications, although it is an

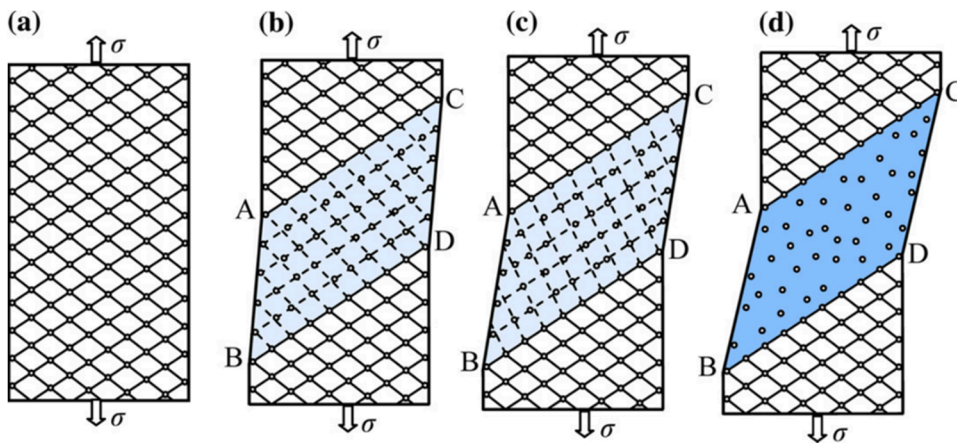


Fig. 60. 2D evolution of amorphization in the cross section of single crystalline fcc nanowire under tensile loading. (a) Initial state. (b) Spatially inhomogeneous multiplane shear is generated by shear stress within the region ABCD 45° from the loading direction. (c) The average shear stress keeps increasing until achieve the Burgers vector magnitude of twinning Shockley partials. Then 2D amorphous state forms in the crystallographic planes. (d) The conventional 3D amorphous phase forms within the plastically sheared region ABCD because of the elastic instability [121].

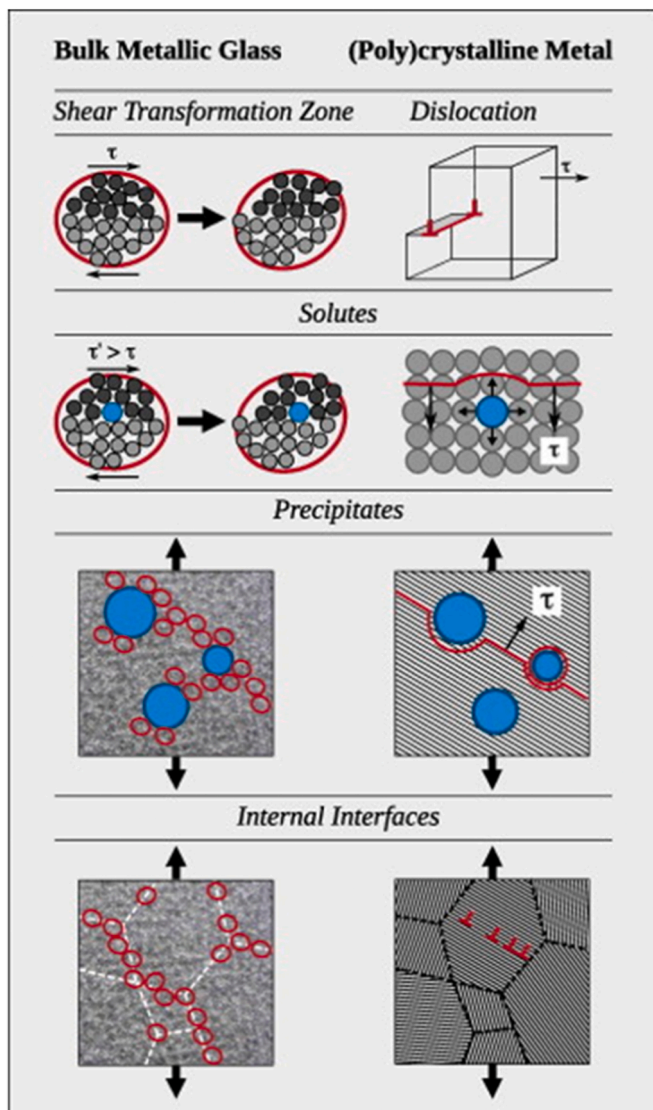


Fig. 61. How different microstructural defects can modify mechanical properties in both polycrystalline metals and bulk metallic glasses. Although the micro-mechanisms are quite different, the same methods can be used [122].

avenue that is being pursued. The most common of them, ball milling of powders and their subsequent consolidation, presents a bright prospect for commercialization.

In this review, we concern ourselves with the fundamental aspects of amorphization by plastic deformation. These are presented for different materials according to their class:

1) Metals and alloys:

A large number of metallic alloys have shown amorphization: Cu-Nb-(Si, Ge or Sn) alloy systems, Nb₃Sn, stainless steel, graphite flakes in gray cast iron, Cantor and some other high-entropy alloys. This phenomenon has only been observed in one pure metal: nanocrystalline nickel by quasi-static compression. Crystals are conventionally considered as deforming through generation and propagation of crystal lattice defects. The process may lead to, in favorable conditions to the formation of nanoscale amorphous regions, nanoscale amorphization.

2) Intermetallic compounds:

Dislocations are the primary carriers of plastic deformation in metals, and their interactions with each other and with other structural features such as grain boundaries (GBs) lead to strengthening. Typically, lack of dislocation plasticity will lead to a brittle failure of the sample. Ni-Zr, Ni₃Al, explosively welded Ti/Ni clad, NiTi, Ni_xZr_y, ZrCu, Zr₅₀Cu₄₀Al₁₀ and samarium-cobalt (SmCo₅) produced by different methods of severe plastic deformation have been studied. For the intermetallic compound samarium-cobalt (SmCo₅), in nanoindentation deformation at small grain sizes, the primary deformation mechanism is grain-boundary sliding, while for larger grain sizes, both grain-boundary sliding and the formation of amorphous shear bands occur. By far the most studied intermetallic is NiTi.

3) Covalent and ionic materials:

Covalent materials, by virtue of their open structures and negative Clapeyron behavior, are also amenable to amorphization and the following systems are reviewed: olivine, Si, cristobalite, α-quartz, α-berlinite, CaSiO₃, serpentine, B₄C, boron suboxide, diamond, Ge, SiC, and forsterite.

A similar phenomenon of deformation-induced amorphization has been observed in the extreme deformation in ionic materials like Ca(OH)₂ and calcium phosphates.

4) Biological materials:

Nature constructs lightweight, strong and tough biological materials under constrained environment with limited available resources. The impact surface of the fast-striking dactyl club of the mantis shrimp is an example of such a composite material. This shrimp has evolved the capability to localize damage and avoid catastrophic failure from high-speed impact during its feeding

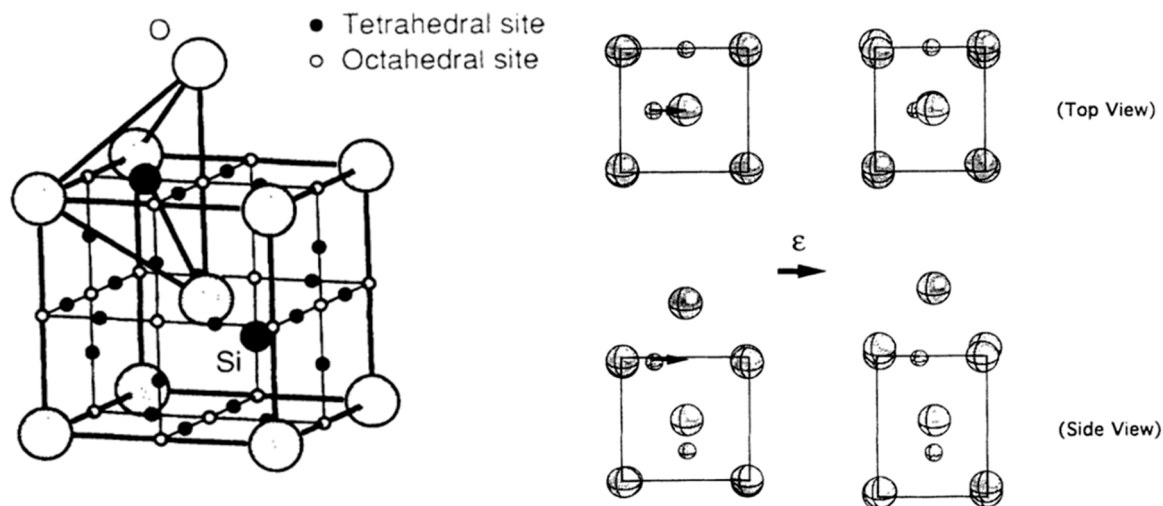


Fig. 62. On the left, the tetrahedral and octahedral sites in the silica structure. At 0 GPa, the stable form is SiO_4 , where silicon atoms are located at the tetrahedral sites. On the right, the movement of the atoms with increasing strain, resulting in the changing coordination [123].

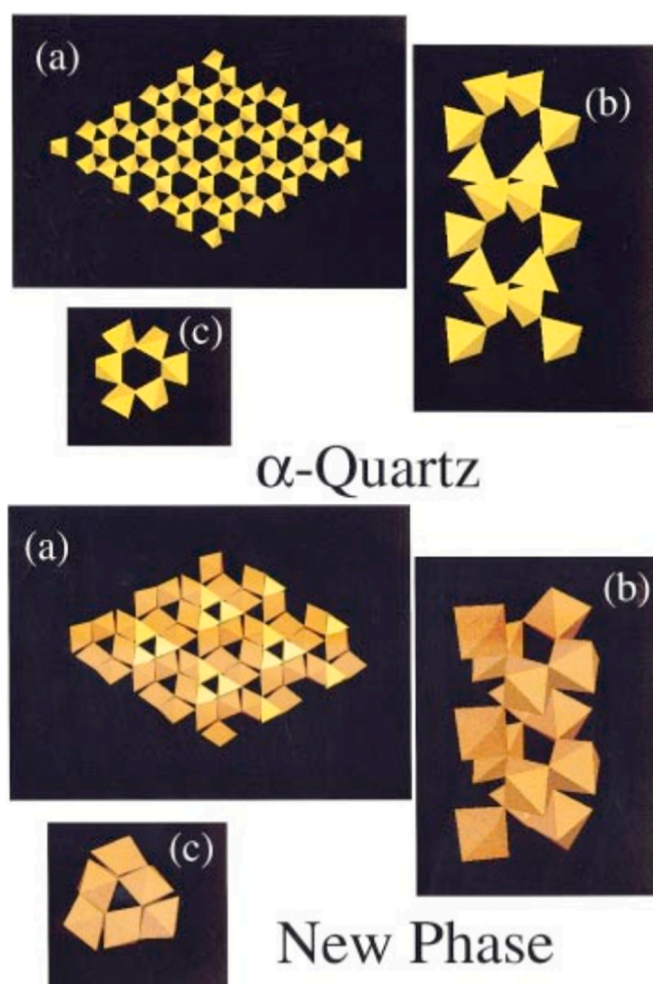


Fig. 63. Crystalline silica at 0 GPa pressure. (a) Top view along the c-axis. (b) Side view of the tetrahedral double-helix structure of silica (c) Projection along the C-axis. New Crystalline structure formed after increasing pressure to 33 GPa and annealing. The original structure of SiO_4 atoms has changed to edge sharing SiO_6 octahedra in a denser configuration. (a) Top view along the c-axis. (b) Side view of the distorted structure (c) Projection along the c-axis [125].

activities. By implementing amorphization into the design of the nanoparticle structures, the stiffness and strength are substantially increased compared with those of structures with non-integrated phases, leading to a higher energy absorption.

The plastic deformation of amorphous materials is also relevant to the focus of this review. It can represent the last stage, when amorphization has already been reached through mechanical means. There are essentially two theories that predict mechanisms for this deformation: free volume and shear transformation zone theories. They are both critically reviewed herein.

The process of amorphization can release the large deviatoric stresses accumulated at the intersections of crystal defects such as dislocations, stacking faults, twins or phase transformation zones. The release of the deviatoric stresses can suppress the initiation and propagation of nano-sized cracks that would otherwise lead to failure of the material. Thus, the amorphous phase is generally harder than its crystalline counterpart because dislocations cannot propagate in it, which makes these materials a competitive rival for extreme load-bearing applications such as in impact, penetration, protection, and extreme strain-rate conditions. Amorphization can be considered a deformation mechanism in addition to dislocation-mediated plasticity, mechanical twinning, and phase transformations; it provides an effective pathway to dissipate the imposed strain energy.

As much as it has been observed in a variety of materials by different means, amorphization by mechanical deformation is a field of research that is still in its early stages. We lay out a few future directions for this emerging and exciting branch of materials science:

- (1) Generalization of deformation-induced amorphization in a broader scope of materials, especially those of metallic nature.
- (2) Taking amorphization into account as an additional deformation mechanism, understanding the effect of amorphization on the plastic flow, and incorporating it in the constitutive models, especially in those for materials under extreme regimes.
- (3) Exploration of the physical-chemical-mechanical properties of amorphous materials produced by mechanical deformation and comparing them with those produced by conventional melting and quenching processes. Correlating these properties with the representative structures of the amorphous phase, especially short-range and medium-range order, structural motifs, and local symmetry [145].
- (4) Development of a rigorous and general theory of deformation-induced amorphization. The theory should capture the physical

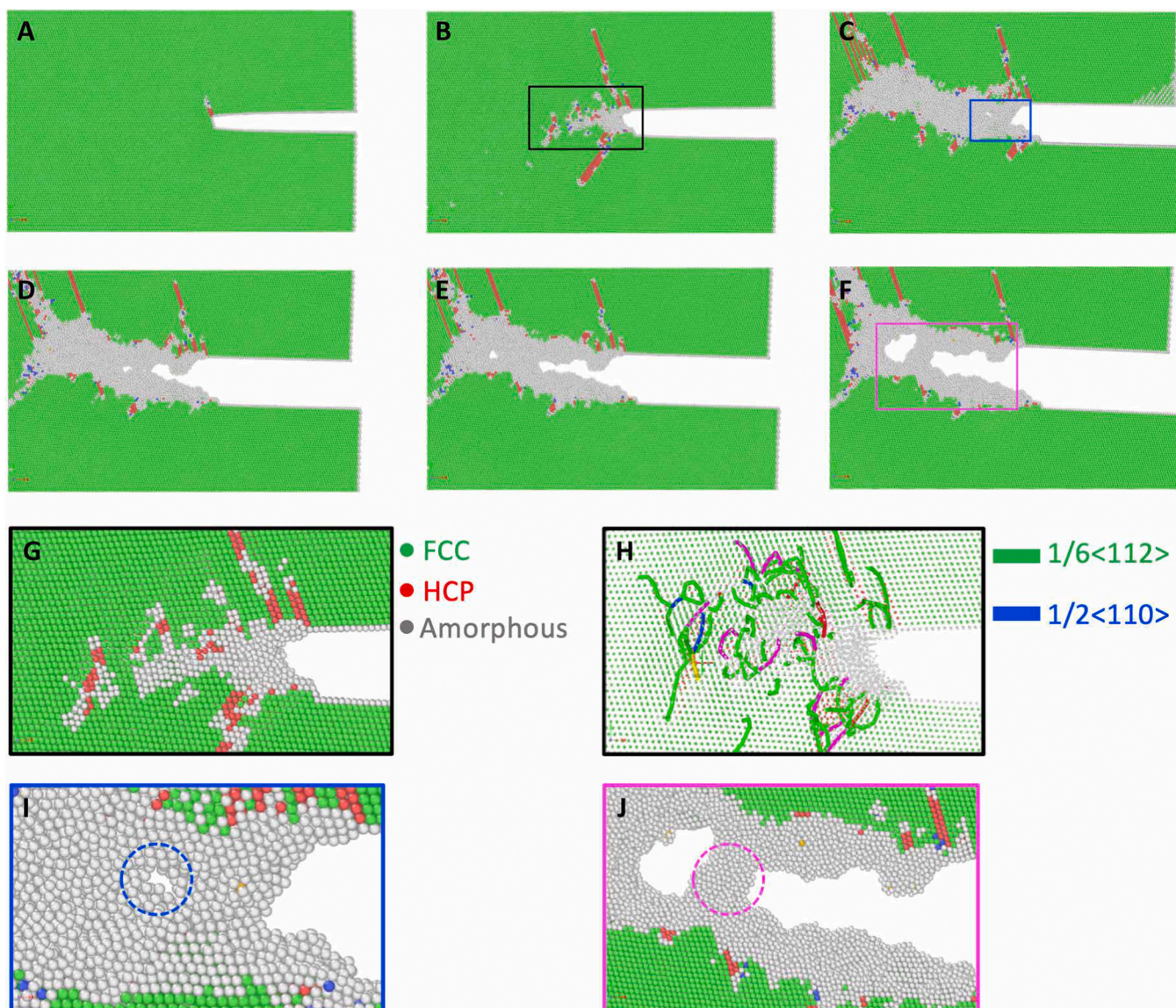


Fig. 64. Crack tip molecular dynamics simulation in a 10% Al 90% Cu alloy under tensile load. (a to f) Increasing tensile load results in the evolution of the amorphous phase around the crack tip region. Three phases of atoms are identified: FCC (green), HCP (red), and amorphous (gray). (g and h) Magnified images in the rectangle area in (b) with associated dislocation analysis. (i) Magnified image in the rectangle area in (c). A nanovoid has nucleated ahead of crack tip. (j) Magnified image of the rectangle area in (f). An amorphous nanobridge has formed in the wake of crack growth [127].

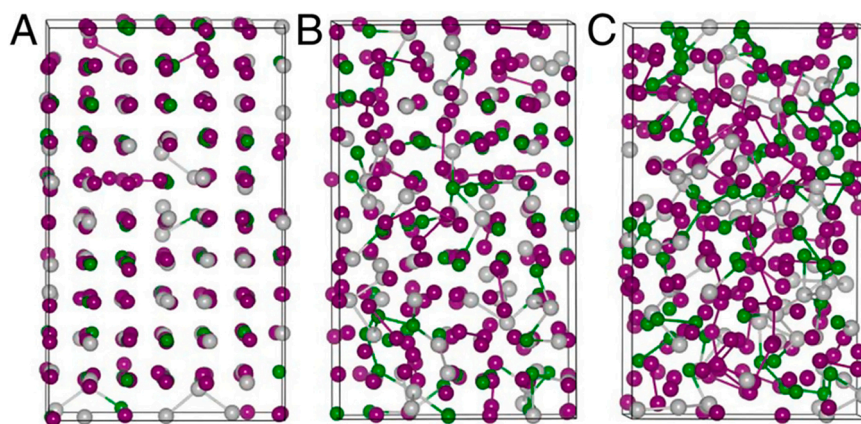


Fig. 65. Cubic GST at (a) 18 GPa, (b) 22 GPa, and (c) 33 GPa. Te atoms initially slip to neighboring vacancies at 18 GPa, resulting in local distortion and creation of homopolar Te-Te, Sb-Sb, and Sb-Ge bonds. At 22 GPa, Ge-Ge bonds begin to appear. All homopolar bonds increase in amount with increasing pressure [128].

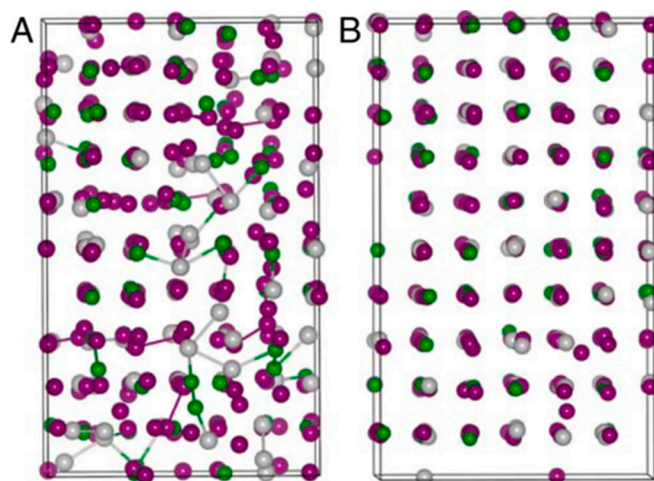


Fig. 66. c-amorphous GST after decompressing to lattice parameters of (a) 5.56 angstroms and (b) 6.02 angstroms. The number of homopolar bonds initially decreases before returning to the original cubic structure [128].

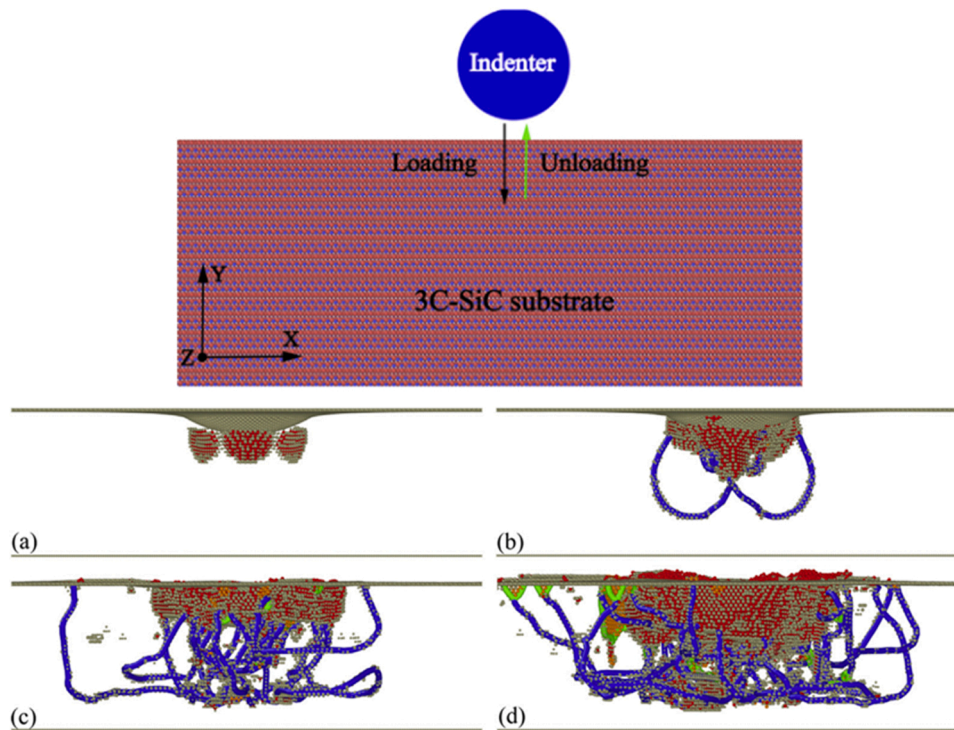


Fig. 67. The MD model for loading and unloading of a nanoindenter on monocrystalline 3 C-SiC MD Snapshots of defects under different loading stages of the nanoindentation (a)1.56 nm, (b) 1.6 nm, (c) 2.84 nm, (d) 4 nm. Red indicates amorphous phase. Orange and gray are hexagonal diamond and surface atoms, respectively. Green and Blue are $1/6 \langle 112 \rangle$ and $1/2 \langle 110 \rangle$ dislocations, respectively [129].

picture of the phenomenon and predict the threshold. Kinetics of amorphization should be paid more attention to. Whether amorphization is a strain-induced, or stress-assisted process needs to be clarified.

- (5) Uncovering the deformation mechanisms of the newly formed amorphous materials. How it accommodates the plastic deformation of a polycrystalline material is still unknown. Whether density-driven amorphous-to-amorphous phase transitions exist and how they proceed remains controversial.

With the advances in the in-situ characterization tools such as in-situ

scanning and transmission electron microscopy [146], scanning electron nanobeam diffraction (better known as 4D-STEM) [147], atomic resolution tomography [148,149], electron energy loss spectroscopy and time-resolved X-ray diffraction, both spatial-temporal and energy resolution of characterization techniques are extended to an unprecedented level, enabling us to probe structural-chemical information of disordered materials with higher fidelity. On the other hand, the rapid advance of machine learning (ML) has stimulated the development of structural representations (also called descriptors or features) of glasses, such as symmetry function [150,151], interstice distribution [152,153], and recently, representations directly learned from deep neural

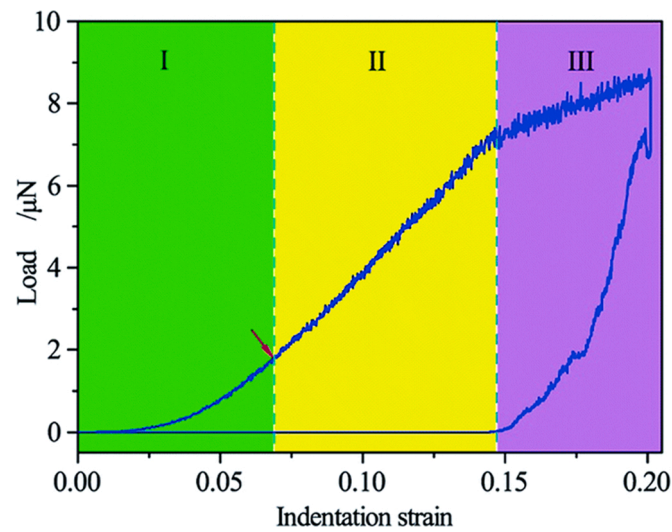


Fig. 68. Load vs. Indentation curve for nanoindentation in silicon. Zone 1 is the elastic region and Zone 2 is the plastic region. At the beginning of zone 3, a sharp discontinuity can be seen, where the deformation mechanism becomes dominated by the formation of an amorphous phase [133].

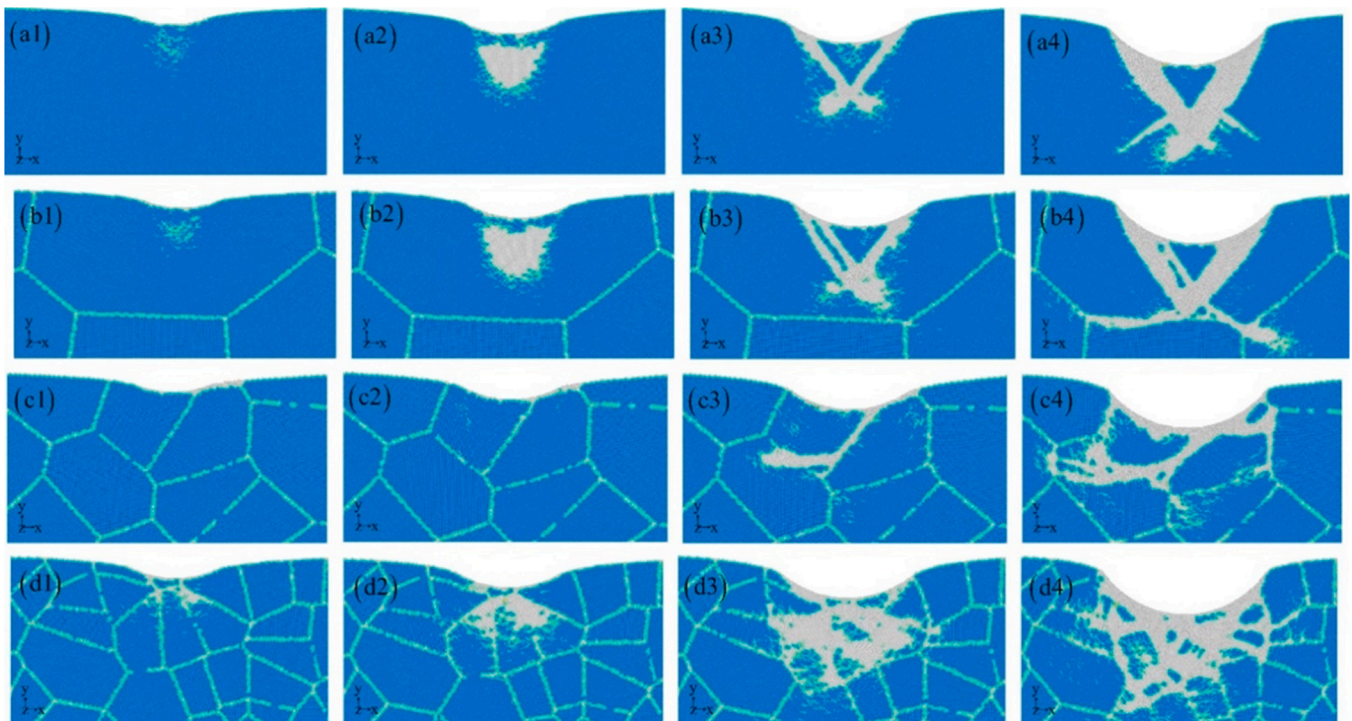


Fig. 69. Microstructure evolution of single-crystalline (top row, a) and polycrystalline silicon (bottom three rows, for different grain sizes, b, c, d). The depth of indentation: Case 1: 3.0 nm (a1), 4.5 nm (a2), 6.5 nm (a3), 9.0 nm (a4); Case 2: 3.0 nm (b1), 4.5 nm (b2), 6.5 nm (b3), 9.0 nm (b4); Case 3: 3.0 nm (c1), 4.5 nm (c2), 6.5 nm (c3), 9.0 nm (c4); Case 4: 3.0 nm (d1), 4.5 nm (d2), 6.5 nm (d3), 9.0 nm (d4) [134].

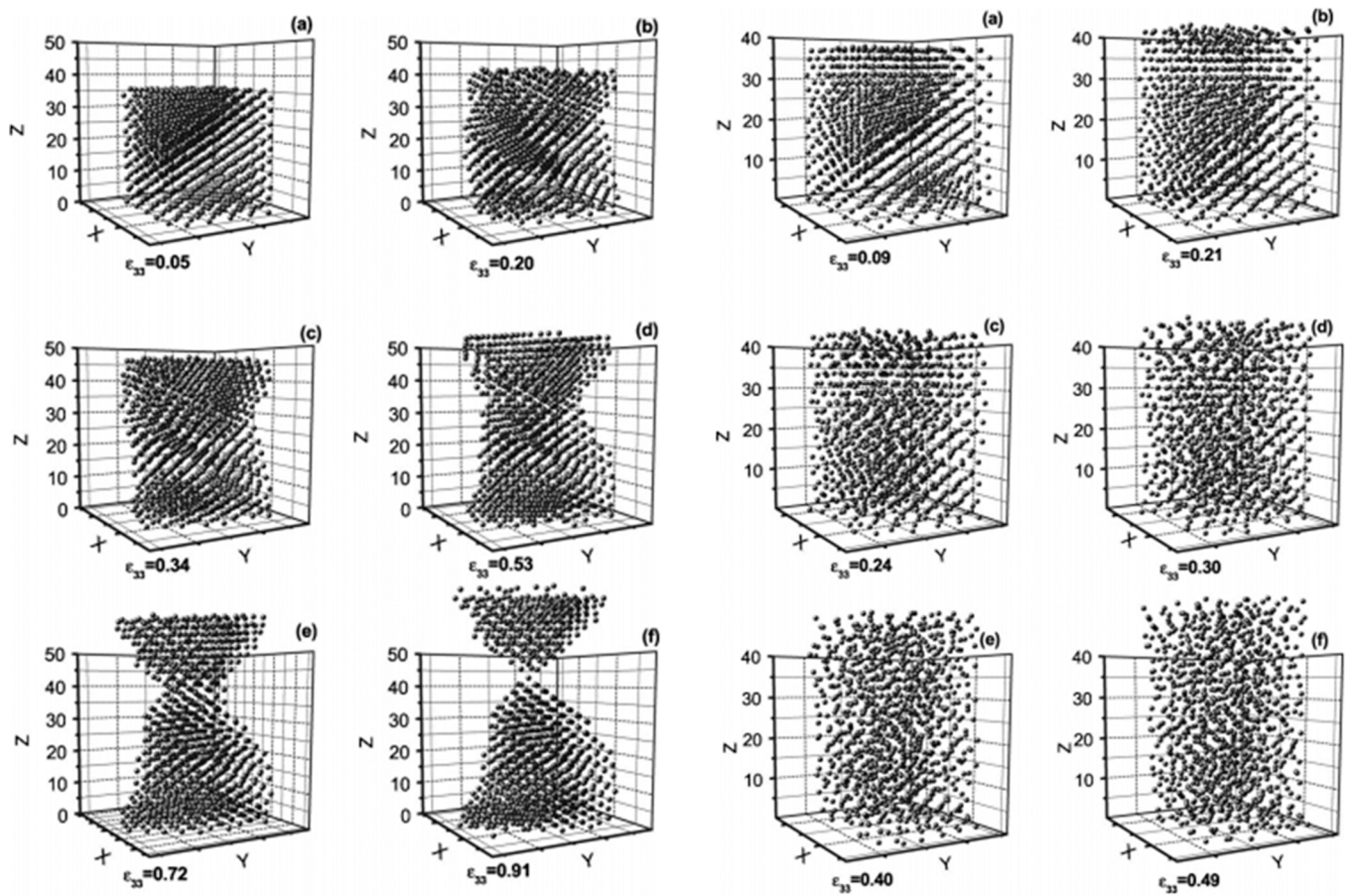


Fig. 70. Deformation differences in nickel nanowires at different strain rates. Left: Necking occurs at strain rates below 7%/ps. Right: Amorphization occurs at strain rates above 7%/ps [136].

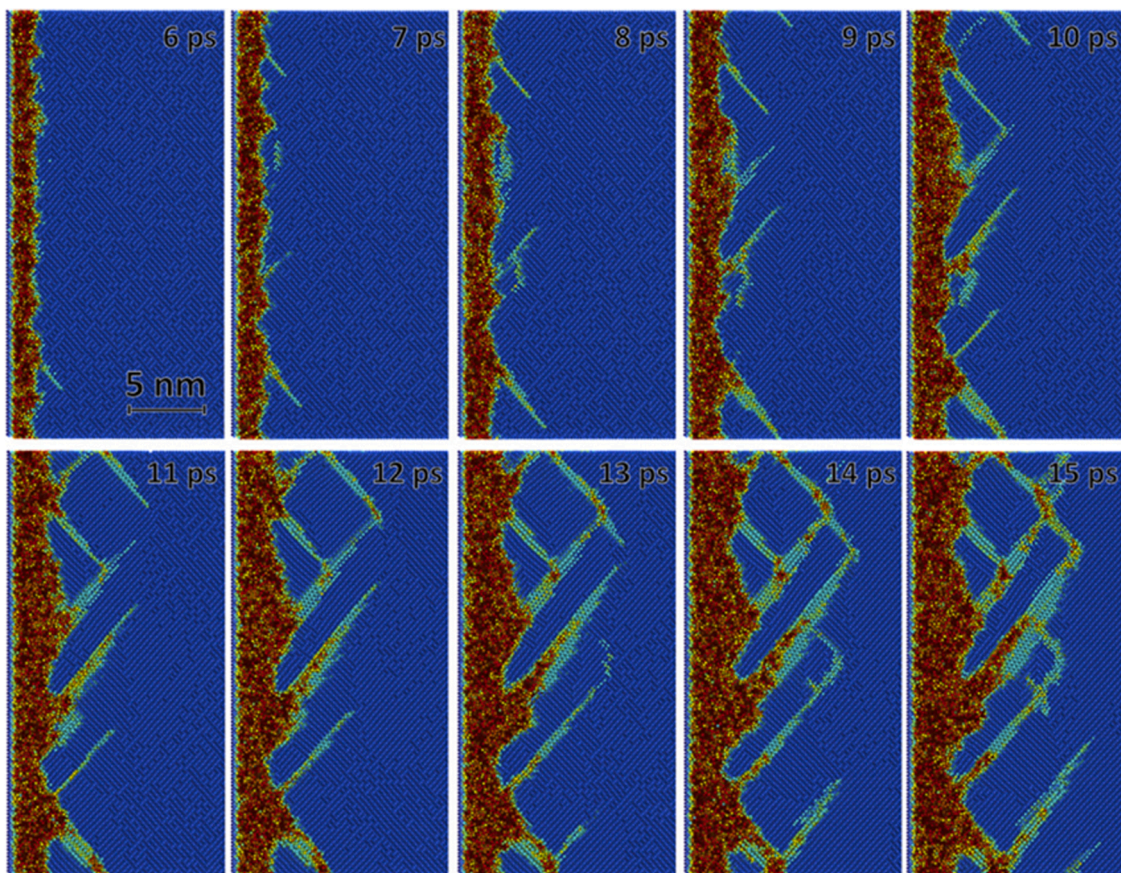


Fig. 71. Time evolution of shocked silicon. The initial surface is amorphized by shock compression. As the shock wave passes through, shear bands form. The intersections of the shear bands give rise to more amorphous regions (in light blue) [137].

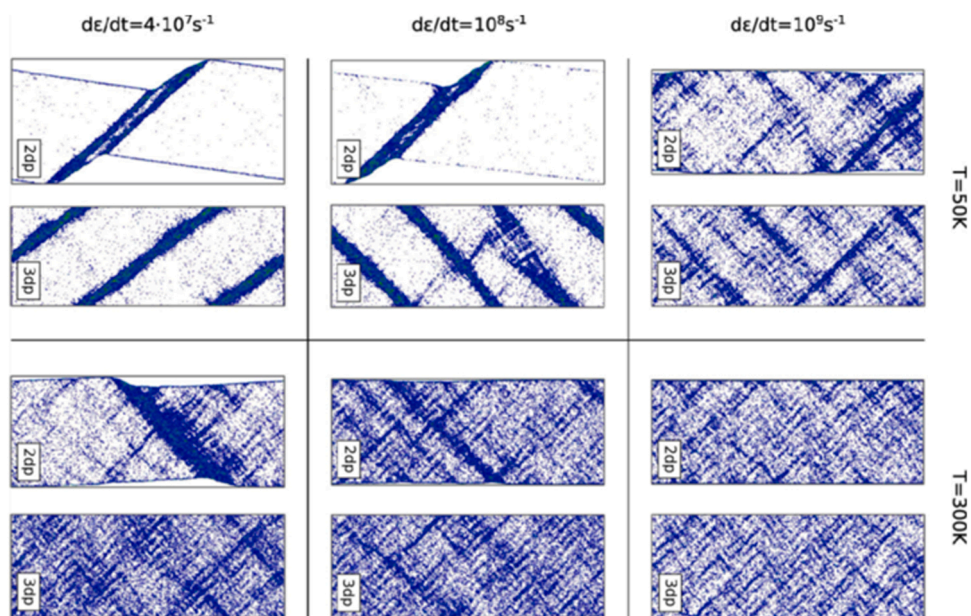


Fig. 72. Snapshots of samples deformed to 18% strain at different temperatures and strain rates. Atoms within shear transformation zones, indicated by a local shear strain higher than 0.2, are highlighted in blue [122].

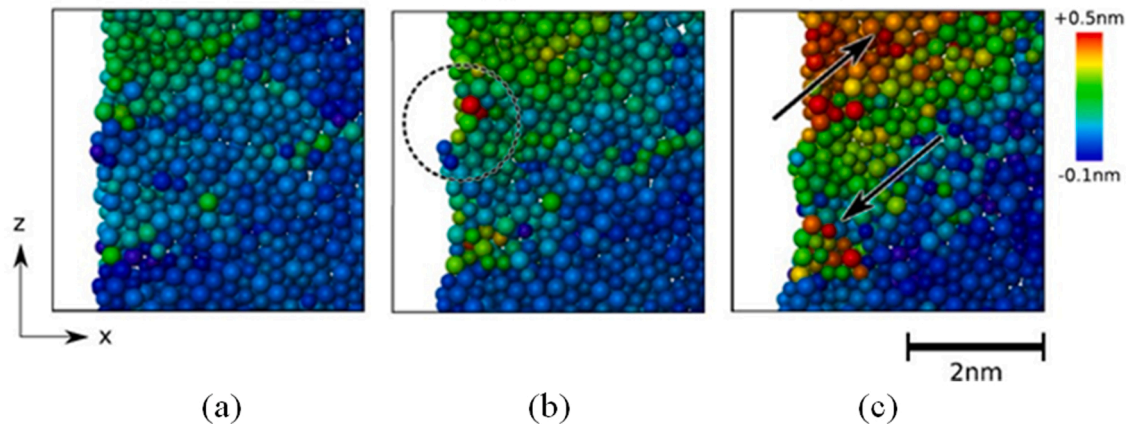


Fig. 73. In a binary $\text{Cu}_{64}\text{Zr}_{36}$ metallic glass, shear transformation zones create a surface defect, which results in shear band nucleation. At 8% strain, surface roughness is low and no surface defects act as stress concentrators. At 9% strain, the STZ is activated and leaves behind a kink. At 10.6% this kink has served as a stress concentrator and leads to shear localization [122].

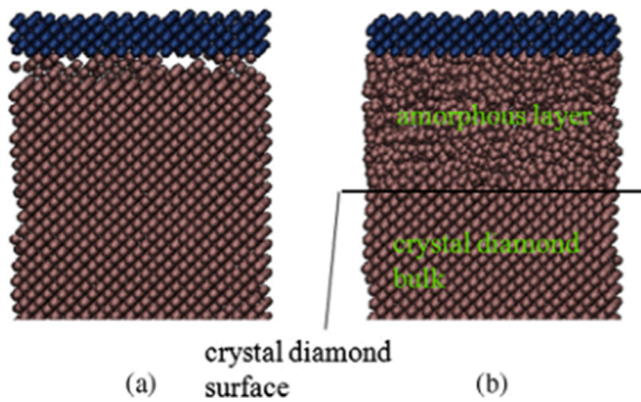


Fig. 74. Diamond crystal (a) before and (b) after sliding friction. The thickness of the amorphous layer increases with the degree of amorphization within the layer. It can be separated into two regions, a coherent layer and a transition layer, determined by the velocity of the carbon atoms [141].

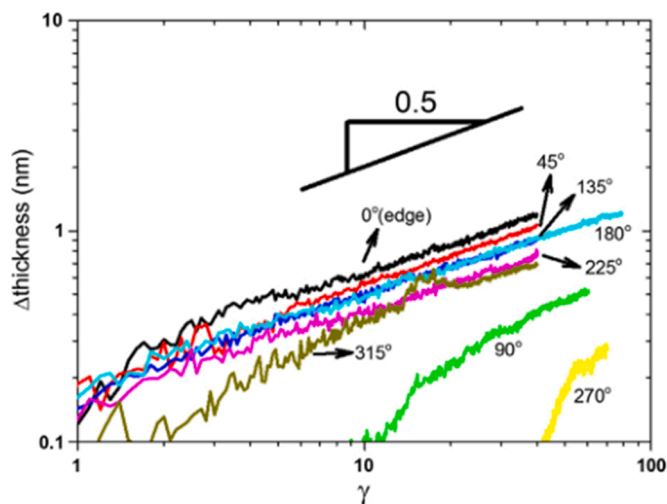


Fig. 75. Increasing amorphous layer thickness with shear strain γ in the Cu/Nb interface. Different angles produced different amorphous layers [142].

networks in an end-to-end manner [154,155]. These representations are more comprehensive than conventional structural signatures in describing the local order of amorphous phase and can be well applied to establish a link between the glassy structure and properties. Therefore, it can be concluded with confidence that we are on the verge of uncovering the mysterious nature of deformation-induced amorphization and much exciting science is waiting around the corner.

The relevance and timeliness of this theme is confirmed by the extensive 1996 review [156] on the effect of pressure on the amorphization of materials, with emphasis on minerals. This phenomenon is of significant import in geophysics. The work presented herein deals principally with the effects of deviatoric (shear) rather than hydrostatic stresses and does not overlap with theirs. High pressures are generated in the interior of the earth and exoplanets, as well as in meteorite impact and tectonic processes. A second review by Idrissi et al. [112], appeared in the last stages of the preparation of our work. This review article reinforces the importance of amorphization induced by deformation of materials.

Declaration of Competing Interest

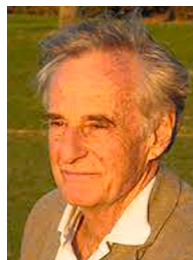
The authors declare that they have no known competing financial interests or personal relationships that could have appeared to influence the work reported in this paper.

References

- [1] M.A. Meyers, K.K. Chawla, *Mechanical Behavior of Materials*, Cambridge University Press, 2008.
- [2] W. Klement, R.H. Willens, P. Duwez, *Nature* 187 (1960).
- [3] A. Nicolas, E.E. Ferrero, K. Martens, J.L. Barrat, *Rev. Mod. Phys.* 90 (2018).
- [4] H.W. Sheng, W.K. Luo, F.M. Alamgir, J.M. Bai, E. Ma, *Nature* 439 (2006) 419–425.
- [5] S. v King, *Nature* 213 (1967) 1112–1113.
- [6] L.H. Sperling, *Pioneers Polym. Sci.* (1989) 41–46.
- [7] J.D. Bernal, *Nature* 183 (1959) 141–147.
- [8] Q. Zheng, Y. Zhang, M. Montazerian, O. Gulbitten, J.C. Mauro, E.D. Zanotto, Y. Yue, *Chem. Rev.* 119 (2019) 7848–7939.
- [9] S.K. Patel, B.K. Swain, A. Behera, S.S. Mohapatra, *Met. Glass* (2020).
- [10] E.A. Morrow, M.W. Terban, L.C. Thomas, D.L. Gray, M.J. Bowman, S.J.L. Billinge, S.J. Schmidt, *J. Food Eng.* 243 (2019) 125–141.
- [11] M. Misawa, E. Ryu, K. Yoshida, R.K. Kalia, A. Nakano, N. Nishiyama, F. Shimojo, P. Vashishta, F. Wakai, *Sci. Adv.* 3 (2017).
- [12] A.J. Leide, L.W. Hobbs, Z. Wang, D. Chen, L. Shao, J. Li, *J. Nucl. Mater.* 514 (2019) 299–310.
- [13] B.L. Darby, *Amorph. Solid Phase Epitaxial Growth Germanium* (2012).
- [14] Z.Q. Chen, F. Wang, P. Huang, T.J. Lu, K.W. Xu, *J. Nanomater.* 2013 (2013).

- [15] P.H.B. Brant Carvalho, A. Mace, C.L. Bull, N.P. Funnell, C.A. Tulk, O. Andersson, U. Häussermann, *J. Chem. Phys.* 150 (2019).
- [16] P. Richet, P. Gillet, *Eur. J. Miner.* 9 (1997) 907–933.
- [17] J. Tominaga, L. Bolotov, *Appl. Phys. Express* 12 (2019).
- [18] E. Zarkadoulou, M. Toulemonde, W.J. Weber, *Appl. Phys. Lett.* 107 (2015).
- [19] L. Romano, K.S. Jones, K. Sekar, W.A. Krull, *J. Vac. Sci. Technol. B: Microelectron. Nanometer Struct.* 27 (2009) 597.
- [20] S.K. Deb, M. Wilding, M. Somayazulu, P.F. Mcmillan, *Nature* 414 (2001) 528–530.
- [21] W. Qiang, K. Löbmann, C.P. McCoy, G.P. Andrews, M. Zhao, *Pharmaceutics* 12 (2020) 1–19.
- [22] T. Einfal, O. Planinšek, K. Hrovat, *Acta Pharm.* 63 (2013) 305–334.
- [23] L. Pelaz, L.A. Marqués, J. Barbolla, *J. Appl. Phys.* 96 (2004) 5947–5976.
- [24] A.U. Ortiz, A. Boutin, A.H. Fuchs, F.X. Coudert, *J. Phys. Chem. Lett.* 4 (2013) 1861–1865.
- [25] A.R. Niknam, M. Hashemzadeh, B. Shokri, M.R. Rouhani, *Phys. Plasmas* 16 (2009).
- [26] A. Meldrum, L.A. Boatner, R.C. Ewing, *Phys. Rev. Lett.* 88 (2002) 4.
- [27] A. Meldrum, L.A. Boatner, W.J. Weber, R.C. Ewing, *J. Nucl. Mater.* 300 (2002) 242–254.
- [28] R. Mejdoub, H. Hammi, M. Khitouni, J.J. Suñol, A. M'nif, *J. Mater. Civ. Eng.* 29 (2017), 04017019.
- [29] K. Hurlle, J. Neubauer, F. Goetz-Neunhoeffer, *BioNanoMaterials* 18 (2017).
- [30] G.N. Greaves, F. Meneau, A. Sapelkin, L.M. Colyer, I. ap Gwynn, S. Wade, G. Sankar, *Nat. Mater.* 2 (2003) 622–629.
- [31] M. Fujita, Y. Izawa, ... T.N.... on L. and, undefined 2009, The European Conference on Lasers and Electro-Optics (2009).
- [32] M. Doreth, M.A. Hussein, P.A. Priemel, H. Grohganz, R. Holm, H. Lopez de Diego, T. Rades, K. Löbmann, *Int. J. Pharm.* 519 (2017) 343–351.
- [33] F. Djurabekova, M. Backholm, M. Backman, O.H. Pakarinen, J. Keinonen, K. Nordlund, T.R. Shan, B.D. Devine, S.B. Sinnott, *Nucl. Instrum. Methods Phys. Res., Sect. B: Beam Interact. Mater. At.* (2010) 3095–3098.
- [34] A.M. Grishin, *Crystals* 10 (2020) 1–10.
- [35] S. Cao, T.D. Bennett, D.A. Keen, A.L. Goodwin, A.K. Cheetham, *Chem. Commun.* 48 (2012) 7805–7807.
- [36] A. Battaglia, S.U. Campisano, *J. Appl. Phys.* 74 (1993) 6058–6061.
- [37] A.K. Arora, V.S. Sastry, P.C. Sahu, T.A. Mary, *J. Phys. Condens. Matter* 16 (2004) 1025–1031.
- [38] P.K. Khulbe, X. Xun, M. Mansuripur, *Appl. Opt.* 39 (2000) 2359–2366.
- [39] Y. Akahama, Y. Mori, M. Kobayashi, H. Kawamura, K. Kimura, S. Takeuchi, *J. Phys. Soc. Jpn.* 58 (1989) 2231–2234.
- [40] A.T. Motta, F. Lefebvre, C. Lernaigan, Zirconium in the Nuclear Industry: Ninth International Symposium. ASTM International (1991).
- [41] L. Douillard, J. Durand, *J. De. Phys. III* 6 (1996).
- [42] T.-T. Jiang, J.-J. Wang, L. Lu, C.-S. Ma, D.-L. Zhang, F. Rao, C.-L. Jia, W. Zhang, *APL Mater.* 7 (2019).
- [43] R.C. Ewing, A. Meldrum, L. Wang, S. Wang, *Rev. Mineral. Geochem.* 39 (2000) 319–361.
- [44] K. Wang, R. Liu, Y. Qiao, J. Cui, B. Song, B. Liu, B. Zou, (2015).
- [45] J. Hirayama, H. Kobayashi, A. Fukuoka, *Bull. Chem. Soc. Jpn.* 93 (2020) 273–278.
- [46] K. Kranjc, A.S. Thind, A.Y. Borisevich, R. Mishra, K.M. Flores, P. Skemer, *J. Geophys. Res.: Solid Earth* 125 (2020).
- [47] P. Carrez, D. Demyk, P. Cordier, L. Gengembre, J. Grimblot, L. D'Hendecourt, A. P. Jones, H. Leroux, *Meteorit. Planet. Sci.* 37 (2002) 1599–1614.
- [48] P.C. Taylor, *World Sci. Ref. Amorph. Mater.: Struct., Prop., Model. Appl.* (2021).
- [49] C. Suryanarayana, *Prog. Mater. Sci.* 46 (2001) 1–184.
- [50] K. Matsuki, L.A. Inoue, H.M. Kimura, T. Masumoto, *Mater. Sci. Eng.* 97 (1988) 47–51.
- [51] Y.S. Cho, C.C. Koch, *Mater. Sci. Eng., A* 141 (1991) 139–148.
- [52] M.A. Meyers, Y.B. Xu, Q. Xue, M.T. Pérez-Prado, T.R. McNelley, *Acta Mater.* 51 (2003) 1307–1325.
- [53] S. Han, L. Zhao, Q. Jiang, J. Lian, *Sci. Rep.* 2 (2012).
- [54] R. Hinrichs, M.A. Zen Vasconcellos, W. Österle, C. Prietzel, *Mater. Res.* 21 (2018).
- [55] W.H. Wang, *JOM* 66 (2014) 2067–2077.
- [56] X. Yang, Y. Zhou, R. Zhu, S. Xi, C. He, H. Wu, Y. Gao, *Acta Metall. Sin. (Engl. Lett.)* 33 (2020) 1057–1063.
- [57] S. Zhao, Z. Li, C. Zhu, W. Yang, Z. Zhang, D.E.J. Armstrong, P.S. Grant, R. O. Ritchie, M.A. Meyers, *Sci. Adv.* 7 (2021) 3108–3137.
- [58] T.C. Pekin, J. Ding, C. Gammer, B. Ozdol, C. Ophus, M. Asta, R.O. Ritchie, A. M. Minor, *Nat. Commun.* 1 (10) (2019) 1–7.
- [59] Y. Wang, J. Li, A.V. Hamza, T.W. Barbee, *Proc. Natl. Acad. Sci.* 104 (2007) 11155–11160.
- [60] W. Guo, E.A. Jägle, P.-P. Choi, J. Yao, A. Kostka, J.M. Schneider, D. Raabe, *Phys. Rev. Lett.* 113 (2014), 035501.
- [61] J. Wang, Q. Zhou, S. Shao, A. Misra, *Mater. Res. Lett.* 5 (2017) 1–19.
- [62] A.W. Weeber, H. Bakker, *J. Less-Common Met.* 141 (1988) 93–102.
- [63] Y. Chen, M. Bibole, R. le Hazif, C. Martin, *Phys. Rev. B* 48 (1993).
- [64] J.S.C. Jang, C.C. Koch, *J. Mater. Res.* 5 (1990).
- [65] J. Koike, D.M. Parkin, M. Nastasi, *Philos. Mag. Lett.* 62 (1990) 257–264.
- [66] M. Nishida, A. Chiba, Y. Morizono, M. Matsumoto, T. Murakami, A. Inoue, *Mater. Trans., JIM* 36 (1995) 1338–1343.
- [67] J.Y. Huang, Y.T. Zhu, X.Z. Liao, R.Z. Valiev, *Philos. Mag. Lett.* 84 (2004) 183–190.
- [68] M. Peterlechner, T. Waitz, H.P. Karnthaler, *Scr. Mater.* 60 (2009) 1137–1140.
- [69] G. Thomas, H. Mori, H. Fujita, R. Sinclair, *Scr. Metall.* 16 (1982) 589–592.
- [70] K. Yamada, C.C. Koch, *J. Mater. Res.* 8 (1993) 1317–1326.
- [71] D.M. Grant, S.M. Green, J.V. Wood, *Acta Metall. Mater.* 43 (1995) 1045–1051.
- [72] E. v Tatyaniin, V.G. Kurdwmov, *Subj. Classif.: 61. 70 62. 20; 64. 70; S1. 2 Inst. High. Press. Phys.* (1990).
- [73] S. Jiang, L. Hu, Y. Zhang, Y. Liang, *J. Non-Cryst. Solids* 367 (2013) 23–29.
- [74] C. Ye, X. Zhou, A. Telang, H. Gao, Z. Ren, H. Qin, S. Suslov, A.S. Gill, S. R. Mannava, D. Qian, G.L. Doll, A. Martini, N. Sahai, V.K. Vasudevan, *J. Mech. Behav. Biomed. Mater.* 53 (2016) 455–462.
- [75] P. Hua, K. Chu, Q. Sun, *Scr. Mater.* 154 (2018) 123–126.
- [76] K. Tsuchiya, O. Ciuca, *Materials Science Forum*, in: Materials Science Forum, Trans Tech Publications Ltd, 2011, pp. 17–24.
- [77] H. Luo, H. Sheng, H. Zhang, F. Wang, J. Fan, J. Du, J. Ping Liu, I. Szuflarska, *Nat. Commun.* 10 (2019) 1–8.
- [78] R. Jeanloz, T.J. Ahrens, J.S. Lally, G.L. Nord, J.M. Christie, A.H. Heuer, *Science* 197 (1977) 457–459.
- [79] K. Minowa, K. Sumino, *Phys. Rev. Lett.* 69 (1992) 320–322.
- [80] K.J. Kingma, C. Meade, R.J. Hemley, H.K. Mao, D.R. Veblen, *Science* 259 (1993) 666–669.
- [81] A.J. Gratz, L.D. DeLoach, T.M. Clough, W.J. Nellis, *Science* 259 (1993) 663–666.
- [82] P. Cordier, J.C. Doukhan, J. Peyronneau, *Phys. Chem. Miner.* 20 (1993) 176–189.
- [83] G.C. Serghiou, W.S. Hammack, *J. Chem. Phys.* 98 (1993) 9830–9834.
- [84] T. Irifune, K. Kuroda, N. Funamori, T. Uchida, T. Yagi, T. Inoue, N. Miyajuma, *Science* 272 (1996) 1468–1470.
- [85] X. Markenscoff, *J. Mech. Phys. Solids* 152 (2021), 104379.
- [86] M. Chen, J.W. Mccauley, K.J. Hemker, *Science* 299 (2003) 1563–1566.
- [87] G. Subhash, D. Ghosh, J. Blaber, J.Q. Zheng, V. Halls, K. Masters, *Acta Mater.* 61 (2013) 3888–3896.
- [88] G. Subhash, A.P. Awasthi, C. Kunka, P. Jannotti, M. DeVries, *Scr. Mater.* 123 (2016) 158–162.
- [89] K.M. Reddy, D. Guo, S. Song, C. Cheng, J. Han, X. Wang, Q. An, M. Chen, *Sci. Adv.* 7 (2021) 6714–6731.
- [90] K. Madhav Reddy, A. Hirata, P. Liu, T. Fujita, T. Goto, M.W. Chen, *Scr. Mater.* 76 (2014) 9–12.
- [91] Z. Zeng, L. Yang, Q. Zeng, H. Lou, H. Sheng, J. Wen, D.J. Miller, Y. Meng, W. Yang, W.L. Mao, H.K. Mao, *Nat. Commun.* 8 (2017).
- [92] Y. Shang, Z. Liu, J. Dong, M. Yao, Z. Yang, Q. Li, C. Zhai, F. Shen, X. Hou, L. Wang, N. Zhang, W. Zhang, R. Fu, J. Ji, X. Zhang, H. Lin, Y. Fei, B. Sundqvist, W. Wang, B. Liu, *Nature* 599 (2021) 599–604.
- [93] H. Tang, X. Yuan, Y. Cheng, H. Fei, F. Liu, T. Liang, Z. Zeng, T. Ishii, M.S. Wang, T. Katsura, H. Sheng, H. Gou, *Nature* 599 (2021) 605–610.
- [94] S. Zhao, B. Kad, E. Hahn, L. Chen, Y. Opachi, K. More, B. Remington, C. Wehrenberg, J. Lasalvia, W. Yang, H. Quan, M. Meyers, EPJ Web of Conferences, in: EPJ Web of Conferences, EDP Sciences, 2018.
- [95] S. Zhao, B. Li, B.A. Remington, C.E. Wehrenberg, H.S. Park, E.N. Hahn, M. A. Meyers, *Mater. Today* 49 (2021) 59–67.
- [96] J.R. Patel, M. Cohen, *Acta Metall.* 1 (1953) 531–538.
- [97] V.I. Levitas, R. Ravelo, *Proc. Natl. Acad. Sci.* 109 (2012) 13204–13207.
- [98] V. Samae, P. Cordier, S. Demouchy, C. Bollinger, J. Gasc, S. Koizumi, A. Mussi, D. Schryvers, H. Idrissi, *Nature* 591 (2021) 82–86.
- [99] C. Meade, R. Jeanloz, *Geophys. Res. Lett.* 17 (1990) 1157–1160.
- [100] S.N. Vaidya, V. Sugandhi, *J. Mater. Sci.* 34 (1999) 3769–3778.
- [101] W. Huang, M. Shishehbor, N. Guarín-Zapata, N.D. Kirchner, J. Li, L. Cruz, T. Wang, S. Bhowmick, D. Stauffer, P. Manimunda, K.N. Bozhilov, R. Caldwell, P. Zavattieri, D. Kisailus, *Nat. Mater.* 19 (2020) 1236–1243.
- [102] C.C. Koch, *Scr. Mater.* 34 (1996) 21–27.
- [103] J.R. Patel, M. Cohen, *Acta Metall.* 1 (1953) 531–538.
- [104] J.D. Eshelby, *Solid State Phys. - Adv. Res. Appl.* 3 (1956) 79–144.
- [105] J.D. Eshelby, *Proc. R. Soc. Lond. Ser. A. Math. Phys. Sci.* 241 (1957) 376–396.
- [106] V.I. Levitas, H. Chen, L. Xiong, *Phys. Rev. B* 96 (2017).
- [107] A. Yermakov, Y. Yurchikov, V.A. Barinov, *Phys. Met. Metallogr.* 52 (1981) 50–58.
- [108] C.C. Koch, O.B. Cavin, C.G. McKamey, J.O. Scarbrough, *Appl. Phys. Lett.* 43 (1983) 1017–1019.
- [109] E.P. Donovan, F. Spaepen, D. Turnbull, J.M. Poate, D.C. Jacobson, *J. Appl. Phys.* 57 (1985) 1795–1804.
- [110] I. Szuflarska, R.K. Kalia, A. Nakano, P. Vashishta, *Phys. Rev. B - Condens. Matter Phys.* 71 (2005).
- [111] Z. Wu, W. Liu, L. Zhang, S. Lim, *Acta Mater.* 182 (2020) 60–67.
- [112] H. Idrissi, P. Carrez, P. Cordier, *Curr. Opin. Solid State Mater. Sci.* 26 (2022), 100976.
- [113] G.B. Olson, M. Cohen, *Metall. Mater. Trans. A* 6 (1975) 791.
- [114] F. Spaepen, *Acta Metall.* 25 (1977) 407–415.
- [115] A.S. Argon, *Acta Metall.* 27 (1979) 47–58.
- [116] S. Zhao, *Shock-Induc. Amorph. Covalently Bond. Solids* (2017).
- [117] E.S. Park, *Appl. Microsc.* 45 (2015) 63–73.
- [118] C.A. Schuh, T.C. Hufnagel, U. Ramamurty, *Acta Mater.* 55 (2007) 4067–4109.
- [119] X. Gu, K.J.T. Livi, T.C. Hufnagel, *Mater. Res. Soc. Symp. - Proc.* 754 (2003) 263–268.
- [120] V. Hieronymus-Schmidt, H. Rösner, G. Wilde, A. Zaccone, *Phys. Rev. B* 95 (2017).
- [121] I.A. Ovid'ko, *Scr. Mater.* 66 (2012) 402–405.
- [122] K. Albe, Y. Ritter, D. Şoşu, *Mech. Mater.* 67 (2013) 94–103.
- [123] N. Binggeli, N.R. Keskar, J.R. Chelikowsky, *Phys. Rev. B* 49 (1994) 3075–3081.
- [124] J.R. Chelikowsky, N. Binggeli, *MRS Online Proc. Libr. (OPL)* 291 (1992) 629–639.
- [125] R.M. Wentzcovitch, C. da Silva, J.R. Chelikowsky, N. Binggeli, *Phys. Rev. Lett.* 80 (1998) 2149–2152.
- [126] D.W. Dean, R.M. Wentzcovitch, N. Keskar, J.R. Chelikowsky, N. Binggeli, *Phys. Rev. B - Condens. Matter Phys.* 61 (2000) 3303–3309.

- [127] H. Wang, D. Chen, X. An, Y. Zhang, S. Sun, Y. Tian, Z. Zhang, A. Wang, J. Liu, M. Song, S.P. Ringer, T. Zhu, X. Liao, *Sci. Adv.* 7 (2021) 3105–3136.
- [128] Z. Sun, J. Zhou, Y. Pan, Z. Song, H.K. Mao, R. Ahuja, *Proc. Natl. Acad. Sci.* 108 (2011) 10410–10414.
- [129] L. Zhao, M. Alam, J. Zhang, R. Janisch, A. Hartmaier, *Ceram. Int.* 46 (2020) 12470–12479.
- [130] Z. Tian, X. Xu, F. Jiang, J. Lu, Q. Luo, J. Lin, *Ceram. Int.* 45 (2019) 21998–22006.
- [131] P. Walsh, R.K. Kalia, A. Nakano, P. Vashishta, S. Saini, *Appl. Phys. Lett.* 77 (2000) 4332–4334.
- [132] X. Luo, Z. Zhang, Y. Xiong, Y. Shu, J. He, K. Zheng, Y. Bao, H.M. Urbassek, *Ceram. Int.* 47 (2021) 15968–15978.
- [133] J. Han, S. Xu, J. Sun, L. Fang, H. Zhu, *RSC Adv.* 7 (2017) 1357–1362.
- [134] J. Fan, J. Li, Z. Huang, P.H. Wen, C.G. Bailey, *Comput. Mater. Sci.* 144 (2018) 113–119.
- [135] H. Ikeda, Y. Qi, T. Çagin, K. Samwer, W.L. Johnson, W.A. Goddard, *Phys. Rev. Lett.* 82 (1999) 2900–2903.
- [136] P.S. Branício, J.P. Rino, *Phys. Rev. B - Condens. Matter Mater. Phys.* 62 (2000) 16950–16955.
- [137] S. Zhao, E.N. Hahn, B. Kad, B.A. Remington, C.E. Wehrenberg, E.M. Bringa, M. A. Meyers, *Acta Mater.* 103 (2016) 519–533.
- [138] S. Zhao, B. Kad, E.N. Hahn, B.A. Remington, C.E. Wehrenberg, C.M. Huntington, H.S. Park, E.M. Bringa, K.L. More, M.A. Meyers, *Extrem. Mech. Lett.* 5 (2015) 74–80.
- [139] S. Zhao, R. Flanagan, E.N. Hahn, B. Kad, B.A. Remington, C.E. Wehrenberg, R. Cauble, K. More, M.A. Meyers, *Acta Mater.* 158 (2018) 206–213.
- [140] S. Zhao, B. Kad, C.E. Wehrenberg, B.A. Remington, E.N. Hahn, K.L. More, M. A. Meyers, *Proc. Natl. Acad. Sci. USA* 114 (2017) 9791–9796.
- [141] N. Yang, W. Zong, Z. Li, T. Sun, *Comput. Mater. Sci.* 95 (2014) 551–556.
- [142] J. Zhou, R.S. Averback, P. Bellon, *Acta Mater.* 73 (2014) 116–127.
- [143] W.L. Johnson, *Mater. Sci. Forum* 225–227 (1996) 35–50.
- [144] W.H. Wang, C. Dong, C.H. Shek, *Mater. Sci. Eng. R: Rep.* 44 (2004) 45–89.
- [145] J. Ding, S. Patinet, M.L. Falk, Y. Cheng, E. Ma, *Proc. Natl. Acad. Sci. USA* 111 (2014) 14052–14056.
- [146] C. Gammer, C. Rentenberger, D. Beitel Schmidt, A.M. Minor, J. Eckert, *Mater. Des.* 209 (2021), 109970.
- [147] B.H. Savitzky, S.E. Zeltmann, L.A. Hughes, H.G. Brown, S. Zhao, P.M. Pelz, T. C. Pekin, E.S. Barnard, J. Donohue, L. Rangel Dacosta, E. Kennedy, Y. Xie, M. T. Janish, M.M. Schneider, P. Herring, C. Gopal, A. Anapolsky, R. Dhall, K. C. Bustillo, P. Ercius, M.C. Scott, J. Ciston, A.M. Minor, C. Ophus, *Microsc. Microanal.* 27 (2021) 712–743.
- [148] X. Tian, D.S. Kim, S. Yang, C.J. Ciccarino, Y. Gong, Y. Yang, Y. Yang, B. Duschatko, Y. Yuan, P.M. Ajayan, J.C. Idrobo, P. Narang, J. Miao, *Nat. Mater.* 8 (19) (2020) 867–873.
- [149] Y. Yang, J. Zhou, F. Zhu, Y. Yuan, D.J. Chang, D.S. Kim, M. Pham, A. Rana, X. Tian, Y. Yao, S.J. Osher, A.K. Schmid, L. Hu, P. Ercius, J. Miao, *Nature* 7852 (592) (2021) 60–64.
- [150] E.D. Cubuk, S.S. Schoenholz, J.M. Rieser, B.D. Malone, J. Rottler, D.J. Durian, E. Kaxiras, A.J. Liu, *Phys. Rev. Lett.* 114 (2015), 108001.
- [151] S.S. Schoenholz, E.D. Cubuk, D.M. Sussman, E. Kaxiras, A.J. Liu, *Nat. Phys.* 5 (12) (2016) 469–471.
- [152] Q. Wang, A. Jain, *Nat. Commun.* 1 (10) (2019) 1–11.
- [153] Q. Wang, J. Ding, L. Zhang, E. Podryabinkin, A. Shapeev, E. Ma, *Npj Comput. Mater.* 1 (6) (2020) 1–12.
- [154] V. Bapst, T. Keck, A. Grabska-Barwińska, C. Donner, E.D. Cubuk, S.S. Schoenholz, A. Obika, A.W.R. Nelson, T. Back, D. Hassabis, P. Kohli, *Nat. Phys.* 4 (16) (2020) 448–454.
- [155] Q. Wang, L. Zhang, *Nat. Commun.* 12 (2021).
- [156] S.M. Sharma, S.K. Sikka, *Prog. Mater. Sci.* 40 (1996) 1–77.



M.A. Meyers



S. Zhao